Size effects in microstructured superconductors and quantum materials

Fermin, R.

Citation

Fermin, R. (2022, December 7). *Size effects in microstructured superconductors and quantum materials*. *Casimir PhD Series*. Retrieved from https://hdl.handle.net/1887/3492762

Version:	Publisher's Version
License:	Licence agreement concerning inclusion of doctoral thesis in the Institutional Repository of the University of Leiden
Downloaded from:	https://hdl.handle.net/1887/3492762

Note: To cite this publication please use the final published version (if applicable).

Size Effects in Microstructured Superconductors and Quantum Materials

Proefschrift

ter verkrijging van
de graad van doctor aan de Universiteit Leiden,
op gezag van rector magnificus prof.dr.ir. H. Bijl,
volgens besluit van het college voor promoties
te verdedigen op woensdag 7 december 2022
klokke 16:15 uur

door

Remko Fermin
Geboren te Rotterdam
in 1993

Promotor:

Prof. dr. J. Aarts

Promotiecommissie:

Prof. dr.ir. J.W.M. Hilgenkamp	Universiteit Twente
Dr. A. McCollam	Universiteit Nijmegen
Dr. M. P. Allan	
Prof. dr. ir. T. H. Oosterkamp	
Prof. dr. K.E. Schalm	

Casimir PhD series, 2022-27
ISBN 978-90-8593-538-4

An electronic version of this thesis can be found at:
`https://openaccess.leidenuniv.nl/`.

The research described in this thesis was conducted at the Leiden Institute of Physics, Leiden University. It was financially supported by a grant from the Netherlands Organisation for Scientific Research (NWO) through the Gravitation Program Nanofront and the Casimir Research School.

About the cover: *The cover symbolizes the flag of Leiden, where the keys are composed out of stylized sample geometries studied in this thesis.*

Cover design: Remko Fermin
Copyright © 2022 Remko Fermin

De beloning van de deugd is de deugd zelf

-Baruch Spinoza

CONTENTS

1 Introduction **1**
1.1 Outline of this thesis 3
1.1.1 Part one: Josephson physics in thin film planar junctions 3
1.1.2 Part two: Mesoscopic SF-hybrid Josephson junctions 4
1.1.3 Part three: Strongly correlated ruthenium oxide microstructures 5
References 6

Part one: Josephson physics in thin film planar junctions **11**

2 Superconductivity and Josephson physics **13**
2.1 A macroscopic quantum phenomenon 14
2.2 The Meissner effect and its consequences 15
2.3 Pairing symmetry 17
2.4 The proximity effect and Josephson junctions 20
2.5 Shapiro steps 23
2.6 Magnetic interference in a Josephson Junction 25
2.7 Extracting the supercurrent density with Fourier analysis 27
Appendices 28
A Experimental set-up and measurement procedure. 28
References 29

3 Reducing dimensions: the thin film planar Josephson junction **33**
3.1 Introduction 34
3.2 Review of the Clem model 34
3.3 Comparing different geometries 37
3.3.1 Simulation results 38
3.3.2 Comparison to experiments 42
3.4 Consequences for the Fourier analysis 44
3.4.1 Technical details of the Fourier analysis 45
3.5 Conclusion 47
References 48

Part two: Mesoscopic S−F-hybrid Josephson junctions **51**

4 Superconducting triplet rim currents in a spin-textured ferromagnetic disk **53**
4.1 Introduction 54
4.2 Establishing long-range triplet transport 55
4.3 Triplet currents confined to the rims of the disk. 57
4.4 Altering the magnetic texture by an in-plane field. 58
4.5 Modeling LRT generation at the rims of the disk 60
4.5.1 Mapping spin texture to spin-orbit coupling. 61
4.5.2 Mechanism for generating LRT rim currents 62
4.6 Discussion 63
4.7 Conclusion 64
Appendices 65
A Control experiments 65
References 67

5 Mesoscopic superconducting memory elements based on bistable magnetic textures **73**
5.1 Introduction 74
5.2 Ellipse-shaped S−F−S junctions 76
5.3 Controllable switching 77
5.4 Stray field driven mechanism 80
5.5 Pairing symmetry of the supercurrents 81
5.6 Conclusion and outlook. 82
Appendices 83
A Micromagnetic simulations 83
B Additional data 84
References 87

Part three: Strongly correlated ruthenium oxide microstructures **91**

6 Universal size-dependent nonlinear charge transport in single crystals of the Mott insulator Ca_2RuO_4 **93**
6.1 Introduction 94
6.2 Characterizing microscopic samples 96
6.3 Comparing samples of different cross section. 96

6.4 The role of temperature 100
    6.4.1 Micro-scale thermometry 101
    6.4.2 Comsol simulations 102
    6.4.3 Consequences of heating 103
6.5 Discussion 104
6.6 Conclusion 106
Appendices 107
    A Crystal growth and sample fabrication 107
    B Abrupt transition in a relatively thick microscopic sample 108
    C The Figure of Merit as a function of other length scales 109
    D Reconstructing the JE-characteristic on basis of Joule heating only 110
    E Minimal model for current density inhomogeneity over the cross-sectional area 112
References 114

7 Controlling chiral domain walls in mesoscopic Sr_2RuO_4 using geometry and in-plane magnetic fields 119
7.1 Introduction 120
7.2 Brief experimental history of the pairing symmetry in Sr_2RuO_4 121
    7.2.1 An unconventional superconductor 121
    7.2.2 post-2019 results: a shift from the p-wave paradigm 122
7.3 Trapping a single superconducting domain wall in mesoscopic Sr_2RuO_4 124
7.4 Detection of Shapiro steps 127
7.5 Considerations on geometry 128
7.6 $I_c(T)$ of a chiral domain wall junction 130
7.7 Field-induced bistable domain configurations 131
7.8 Altering the periodicity of current-phase relation with in-plane magnetic fields 135
7.9 Implications for the pairing symmetry 138
7.10 Conclusion and outlook. 139
Appendices 139
    A Sample dimensions of ring samples 139
    B Stability of chiral domain walls under in-plane fields 140
    C proposed experiment to establish a- and b-axis in situ. 142
References 143

Summary **149**

Samenvatting **153**

Curriculum Vitae **158**

List of publications **159**

Acknowledgements **161**

1

INTRODUCTION

At the time of writing, the amount of transistors in the processor of the latest smartphones is in the order of 10^{10}. This results from the information processing industry striving to push the boundaries of how small a transistor can be fabricated. Since the 1970s, the average size of a transistor actually halved every two years, an empirical observation that is known as Moore's law. Since we have entered the realm of the ultra-small, understanding the laws of physics that govern these length scales will prove vital for developing any future computing technologies. Specifically, ones based on novel physics — like superconducting spintronics or neuromorphic computing using correlated electron matter — require a thorough understanding of physical processes at the microscale.

In the case of superconducting spintronics, for example, the field that strives to combine computations using electron spin with the non-dissipative nature of superconductors, the physical processes are magnetism and, naturally, superconductivity. The length scales determining the physics in the latter are the coherence length and London penetration depth. Both are typically between 1 nm and 1 μm (at low temperatures). When reducing the size of superconducting devices to these scales, we need to rethink the relations that normally govern superconductivity on the macro scale. A similar argument can be made for ferromagnets: here, the competition between exchange energy (trying to align the spins) and demagnetization energy (trying to reduce stray fields) causes a ferromagnet to form magnetic domains spontaneously. Reducing the sample size to below the domain size can result in single domain ferromagnets. More importantly, by carefully tuning the geometry of the ferromagnet, a rich variety of magnetic textures, like ferromagnetic vortices and skyrmions, can be stabilized[1–4].

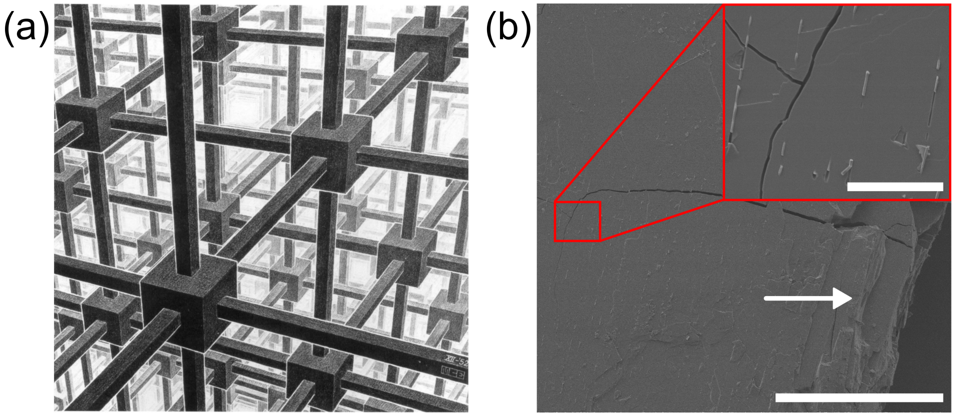

Figure 1.1: (a) *Kubische Ruimteverdeling* by M.C. Escher, how we picture crystalline solids. (b) scanning electron micrograph of an actual macroscopic crystal of Ca_2RuO_4. A large crack is located in the middle of the crystal. Terraced step edges are visible on the side, indicated by the white arrow. The inset shows a scanning electron micrograph of higher magnification. Here some impurities and a zoom of the crack in the crystal can be seen. The scale bar in the main image corresponds to 300 µm; the one in the inset is ten times smaller, namely 30 µm.

Besides probing the laws of physics on the microscale, reducing the size of the studied material improves the controllability of experiments. This is specifically important in the study of correlated electron matter as it involves crystalline form of matter: a periodically ordered lattice of atoms. We picture these materials in their pristine ordered form, namely a repetition of the same unit cell *ad infinitum*, similar to the lithograph *Kubische Ruimteverdeling* by M.C. Escher (see Figure 1.1a). In reality, even the most pure crystals contain micro-cracks, step edges, inclusions of other atoms, and impurities at the macroscopic size level. An example is shown in the scanning electron micrograph of Figure 1.1b. However, when we reduce the system size to mesoscopic levels by cutting out a clean part of the parent compound, we are able to 'zoom in' on a pristine part of the crystal, which significantly improves the controllability of the study.

Typically, microscopic devices are constructed *bottom-up*, meaning their constituents are smaller than the total. For example, by combining lithography and thin film deposition, different material layers are incorporated into a device. This process can be compared to strokes of paint on a canvas. The method faces several difficulties, including the challenging deposition of correlated oxides. In contrast, central to the experiments presented here is a *top-down* technique: by employing a combination of mechanical exfoliation and focused ion beam (FIB) processing, we reduce the size of macroscopic correlated oxide crystals into microstructures. This can be regarded as carving a statue from a larger block of marble. We gain complete control over the size and geometry of the samples while circumventing the need for thin film growth of oxide systems. FIB processing also unlocks the possibility of structuring planar Josephson junctions from macroscopic thin films, with various electrode geometries and feature sizes well below the micrometer scale. For conventional electron beam lithography methods, in contrast, any feature size below 1 μm becomes exponentially difficult.

1.1. OUTLINE OF THIS THESIS

This thesis will study the effects of size reduction and geometry on planar Josephson junctions and highly correlated electron matter using transport experiments. The work is divided into three parts, the first of which introduces the basic concepts of superconductivity and Josephson junctions, which are two superconducting electrodes separated by a non-superconducting weak link. Specifically, we present how these concepts are altered upon reducing the size into microscopic geometries by providing a theoretical framework that relates measurable quantities to the superconducting electrode geometry. Besides, we describe a method to fabricate planar Josephson junctions with a normal metal weak link and arbitrary electrode geometry employed to test this theory. In the second part, we replace the normal metal weak link with a ferromagnet to study the interplay between superconductivity and ferromagnetic spin textures. By carefully tuning the geometry of the sample, we show that spin texture can induce superconducting correlations in a single ferromagnet. Furthermore, we find that the bistability of such textures can be utilized to create a non-volatile superconducting memory element. In the final part of this thesis, we examine the isostructural correlated electron oxides Ca_2RuO_4 and Sr_2RuO_4. For the first, we use the crystal size as the principal tool to investigate its Mott-insulating transition: we find the current density required to drive the crystal out of its insulating phase to have a strong size dependence, which has considerable implications for its possible technological implementation. For Sr_2RuO_4, we use microscopic geometries to isolate a single superconducting domain wall, which acts as a Josephson junction. We show that we can control the periodicity of its current-phase relation by applying in-plane fields. Below I will provide more details on each part of this thesis.

1.1.1. PART ONE: JOSEPHSON PHYSICS IN THIN FILM PLANAR JUNCTIONS

The first part will develop a background on superconductivity and Josephson physics. In Chapter 2, I will discuss that superconductivity is a macroscopic manifestation of quantum mechanics. In a regular conducting solid, the electrons are weakly interacting and repel each other due to their negative charge. Besides, electrons are spin-$\frac{1}{2}$ particles and therefore follow Fermi-Dirac statistics. However, this radically changes upon entering the superconducting phase. Below the superconducting transition, a finite positive pair-wise interaction exists between the electrons, letting them form Bosonic composite particles. Based on the change from Fermionic to Bosonic nature of the charge carriers, I derive the basic properties of superconductors in Chapter 2. Besides, Chapter 2 discusses one of the most fundamental superconducting objects: Josephson junctions. These are non-superconducting connections sandwiched between two superconducting electrodes. I will highlight how the quantum nature of superconductors truly shines in these junctions by deriving how the maximum supercurrent (called critical current, I_c) is dependent on an externally applied magnetic field (B), among other basic properties.

In Chapter 3, I will discuss how the properties of a Josephson junction alter when the thickness of the electrodes is reduced below the London penetration depth, forming so-called thin film planar junctions. Specifically, for junctions featuring laterally constrained and arbitrarily shaped electrodes, $I_c(B)$ becomes governed by non-local electrodynamics[5–8]. This expresses itself in $I_c(B)$ becoming completely dependent on the geometry of the electrodes. By extending the theory to ellipsoid and rhomboid geometries, Chapter 3 builds on the work of John Clem, who derived $I_c(B)$ for junctions with a rectangular geometry[9]. Besides, we verify the theory by fabricating elliptically shaped Josephson junctions with various aspect ratios. Finally, we use these results to adjust the Fourier relation between $I_c(B)$ and the critical current distribution in the junction. This is the perfect tool to study the appearance of current channels in the magnetic Josephson junctions, which is the topic of the next part.

1.1.2. PART TWO: MESOSCOPIC SF-HYBRID JOSEPHSON JUNCTIONS

In the second part of this thesis, we study the interplay between magnetic textures and supercurrents. Superconductivity and magnetism are generally antagonistic: in most superconductors, the electrons pair up with opposite spins, whereas the exchange interaction tries to align them. However, over the last 20 years it has been shown that magnetic non-collinearity at the interface of a superconductor can induce long-range triplet superconductivity: pairs of equal spin that can penetrate a ferromagnet over far longer length scales[10–14]. In this part, we combine micromagnetic simulations with the large control over the geometry gained by our top-down fabrication approach to study triplet superconductivity induced directly by spin texture. Specifically, Chapter 4 shows that superconducting triplet correlations can be generated by the vortex magnetization of a single disk-shaped ferromagnet without relying on the conventional combination between spin mixing and spin rotation. Using the analysis developed in the third Chapter, we find the supercurrent to flow in highly localized channels on the rims of the device (aptly named *rim currents*), which are a direct result of an effective spin-orbit coupling caused by the vortex magnetization.

In the fifth Chapter, we examine a more applied example of superconductor-ferromagnet hybrids. Here we show that a transition from circular to elliptical devices can induce bistable magnetic textures at zero applied magnetic field: either the ellipse is magnetized along its long axis, or two vortices are stable near its focal points. Furthermore, the difference in spin-texture is accompanied by a change in critical current, allowing for the creation of a superconducting memory element, which combines the non-volatility of the ferromagnet with the easy dissipationless read-out of the superconductor. By carefully analyzing the simulations, we are able to explain the change in critical current in terms of the stray fields originating from the different magnetic configurations.

1.1.3. PART THREE: STRONGLY CORRELATED RUTHENIUM OXIDE MICROSTRUCTURES

In Part 3, we will shift gears and leave the topic of thin film Josephson junctions. Instead, we will examine a family of strongly correlated electron systems, namely the *Ruthenates*, which exhibits a rich diversity of phenomena that include Mott insulators[15, 16], unconventional superconductivity[17, 18], and magnetism[19, 20]. The topic of Chapter 6 is the paramagnetic Mott insulator Ca_2RuO_4. This perovskite oxide seems a good candidate for Mott-based electronic devices since it features a metal-to-insulator transition triggered by small current densities[21, 22]. However, whether electronic or thermal effects cause this transition is still under debate since the transition can also be induced by heating the crystal to 357K[23]. In Chapter 6, we use the crystal size itself as the principal tool to investigate the insulator to metal transition. We find a four orders of magnitude increase of the current density required to drive Ca_2RuO_4 out of the insulating phase when reducing the size of the crystals to the micrometer range, shattering the promise of applications at the sub-micrometer level. Besides, we investigate the influence of temperature using microscopic contact thermometry and thermal simulations. We conclude that the size dependence cannot be attributed to Joule heating.

In Chapter 7, we return to the realm of superconductivity by treating the isostructural counterpart of Ca_2RuO_4, where the Ca atoms are substituted by strontium. Ever since the discovery of superconductivity in Sr_2RuO_4 in 1994, its pairing symmetry has posed a challenging conundrum[24]. Already in 1995, it was proposed that superconductivity in Sr_2RuO_4 might be a solid-state analog of the A phase of superfluid ^{3}He: a native triplet superconductor that is degenerate in two chiral ground states[25, 26]. Although this idea has been contested since 2019[27, 28], and the current proposals widely vary, the community agrees that the pairing symmetry is of two-component nature[29, 30]. Such a two-component order parameter is likely expected to host multi-domain superconductivity. In a previous work, we utilized microstructures to trap a single superconducting domain wall[31]. This manifested itself as the formation of spontaneous Josephson junctions in the nominally clean crystal. In Chapter 7, we extend this work by measuring the Shapiro response of these junctions. Not only does this serve as a definite proof of the existence of these spontaneous junctions, it additionally allows for characterizing the periodicity of their current-phase relation. We find that, under the application of in-plane (i.e., ab-plane) magnetic fields, the periodicity of the current-phase relation can halve, as evidenced by the appearance of half-integer Shapiro steps.

Furthermore, we show that in-plane fields can decrease the pinning of the domains, resulting in a bistability of the critical current. This allows for switching between a high critical current state and a low critical current state by applying a large enough positive or negative bias current. We finish by reinterpreting these results based on the latest literature regarding the pairing symmetry in Sr_2RuO_4.

REFERENCES

[1] Prejbeanu, I. L. *et al.* In-plane reversal mechanisms in circular Co dots. *J. Appl. Phys.* **91**, 7343–7345 (2002).

[2] Natali, M. *et al.* Correlated magnetic vortex chains in mesoscopic cobalt dot arrays. *Phys. Rev. Lett.* **88**, 157203 (2002).

[3] Chui, C. P., Ma, F. & Zhou, Y. Geometrical and physical conditions for skyrmion stability in a nanowire. *AIP Adv.* **5**, 047141 (2015).

[4] Winkler, T. B. *et al.* Skyrmion states in disk geometry. *Phys. Rev. Applied* **16**, 044014 (2021).

[5] Pearl, J. Current distribution in superconducting films carrying quantized fluxoids. *Appl. Phys. Lett.* **5**, 65–66 (1964).

[6] Ivanchenko, Y. & Soboleva, T. Nonlocal interaction in Josephson junctions. *Phys. Lett. A* **147**, 65–69 (1990).

[7] Abdumalikov, A. A., Jr., Alfimov, G. L. & Malishevskii, A. S. Nonlocal electrodynamics of Josephson vortices in superconducting circuits. *Supercond. Sci. Technol.* **22**, 023001 (2009).

[8] Boris, A. A. *et al.* Evidence for nonlocal electrodynamics in planar Josephson junctions. *Phys. Rev. Lett.* **111**, 117002 (2013).

[9] Clem, J. R. Josephson junctions in thin and narrow rectangular superconducting strips. *Phys. Rev. B* **81**, 144515 (2010).

[10] Bergeret, F. S., Volkov, A. F. & Efetov, K. B. Long-range proximity effects in superconductor-ferromagnet structures. *Phys. Rev. Lett.* **86**, 4096 (2001).

[11] Bergeret, F. S., Volkov, A. F. & Efetov, K. B. Odd triplet superconductivity and related phenomena in superconductor-ferromagnet structures. *Rev. Mod. Phys.* **77**, 1321 (2005).

[12] Houzet, M. & Buzdin, A. I. Long range triplet Josephson effect through a ferromagnetic trilayer. *Phys. Rev. B* **76**, 060504 (2007).

[13] Khaire, T. S., Khasawneh, M. A., Pratt, W. P. & Birge, N. O. Observation of spin-triplet superconductivity in Co-based Josephson junctions. *Phys. Rev. Lett.* **104**, 137002 (2010).

[14] Robinson, J. W. A., Witt, J. D. S. & Blamire, M. G. Controlled injection of spin-triplet supercurrents into a strong ferromagnet. *Science* **329**, 59 (2010).

[15] Nakatsuji, S., Ikeda, S.-i. & Maeno, Y. Ca_2RuO_4: new Mott insulators of layered ruthenate. *J. Phys. Soc. Jpn.* **66**, 1868–1871 (1997).

[16] Zhu, M. *et al.* Colossal magnetoresistance in a Mott insulator via magnetic field-driven insulator-metal transition. *Phys. Rev. Lett.* **116**, 216401 (2016).

[17] Maeno, Y., Kittaka, S., Nomura, T., Yonezawa, S. & Ishida, K. Evaluation of spin-triplet superconductivity in Sr_2RuO_4. *J. Phys. Soc. Jpn.* **81**, 011009 (2012).

[18] Leggett, A. J. & Liu, Y. Symmetry properties of superconducting order parameter in Sr_2RuO_4: A brief review. *J. Supercond. Nov. Magn.* **34**, 1647—-1673 (2020).

[19] Cao, G., McCall, S., Crow, J. E. & Guertin, R. P. Observation of a metallic antiferromagnetic phase and metal to nonmetal transition in $Ca_3Ru_2O_7$. *Phys. Rev. Lett.* **78**, 1751–1754 (1997).

[20] Grigera, S. A. *et al.* Magnetic field-tuned quantum criticality in the metallic ruthenate $Sr_3Ru_2O_7$. *Science* **294**, 329–332 (2001).

[21] Nakamura, F. *et al.* Electric-field-induced metal maintained by current of the Mott insulator Ca_2RuO_4. *Sci. Rep.* **3**, 2536 (2013).

[22] Okazaki, R. *et al.* Current-induced gap suppression in the mott insulator Ca_2RuO_4. *J. Phys. Soc. Jpn.* **82**, 103702 (2013).

[23] Alexander, C. S. *et al.* Destruction of the Mott insulating ground state of Ca_2RuO_4 by a structural transition. *Phys. Rev. B* **60**, R8422(R) (1999).

[24] Maeno, Y. *et al.* Superconductivity in a layered perovskite without copper. *Nature* **372**, 532–534 (1994).

[25] Rice, T. M. & Sigrist, M. Sr_2RuO_4: an electronic analogue of ^{3}He? *J. Phys.: Condens. Matter* **7**, L648 (1995).

[26] Rice, M. An analogue of superfluid ^{3}He. *Nature* **396**, 627–628 (1998).

[27] Pustogow, A. *et al.* Constraints on the superconducting order parameter in Sr_2RuO_4 from oxygen-17 nuclear magnetic resonance. *Nature* **574**, 72–75 (2019).

[28] Petsch, A. N. *et al.* Reduction of the spin susceptibility in the superconducting state of Sr_2RuO_4 observed by polarized neutron scattering. *Phys. Rev. Lett.* **125**, 217004 (2020).

[29] Ghosh, S. *et al.* Thermodynamic evidence for a two-component superconducting order parameter in Sr_2RuO_4. *Nat. Phys.* **17**, 199–204 (2021).

[30] Benhabib, S. *et al.* Ultrasound evidence for a two-component superconducting order parameter in Sr_2RuO_4. *Nat. Phys.* **17**, 194–198 (2021).

[31] Yasui, Y. *et al.* Spontaneous emergence of Josephson junctions in homogeneous rings of single-crystal Sr_2RuO_4. *npj Quantum Mater.* **5**, 21 (2020).

JOSEPHSON PHYSICS IN THIN FILM PLANAR JUNCTIONS

1

2

SUPERCONDUCTIVITY AND JOSEPHSON PHYSICS

Since all chapters in this thesis, except one, concern superconductivity and Josephson junctions, these concepts need some introduction. In this chapter, I will describe that a superconductor is characterized by a transition from fermionic to bosonic behavior of the charge carriers, which leads to a macroscopic quantum state that drives currents by the quantum mechanical phase, expels magnetic fields from the bulk, and exhibits zero electrical resistance. I will discuss the allowed symmetries of the paired electrons and conclude by introducing Josephson junctions and their response to a magnetic field. A part of this chapter is based on the excellent course material on applied superconductivity by Rudolf Gross and Achim Marx[1].

2.1. A MACROSCOPIC QUANTUM PHENOMENON

In a normal metal, charge is carried by electrons. These elementary particles are fermions and thus cannot occupy the same quantum state. Rather, they fill up k-space; therefore, finding a wavefunction that describes such a fermionic system is far from trivial. Including electron-electron interactions, this typically involves solving for 10^{23} degrees of freedom. The quantum mechanical description of a solid radically changes once it enters the superconducting phase. In a superconductor, the electrons experience an attractive force, below a *critical temperature* (T_c), which introduces pairwise phase-coherent interactions between them. These pairs are called *Cooper pairs* and can be regarded as composite particles that are bosonic of nature, which allows them to condense into a single ground state, forming a Bose-Einstein condensate. Since the distance over which electrons pair up is typically much larger than the average distance between electrons, this condensate can be regarded as a fluid, where we think of a density of Cooper pairs instead of individual particles. In this case, the condensate can be captured by a rather simple wavefunction Ψ that describes the collection of all Cooper pairs on the macroscopic scale:

$$\Psi(\boldsymbol{r},t) = \sqrt{n_\mathrm{s}(\boldsymbol{r},t)}e^{i\gamma(\boldsymbol{r},t)} \tag{2.1}$$

Here n_s is the density of Cooper pairs, which is equal to the expectation value of Ψ ($|\Psi|^2 = n_\mathrm{s}$), i is the imaginary unit, and γ is the phase of the wavefunction. By combining the Schrödinger equation and Lorentz's law, it can be shown that a current density of charged particles $\boldsymbol{J}$, driven by an electromagnetic field, equals[1]:

$$\boldsymbol{J} = q\,\mathrm{Re}\left(\Psi^* \frac{\hat{P}}{m}\Psi\right) = q\,\mathrm{Re}\left(\Psi^*\left(\frac{\hbar}{mi}\boldsymbol{\nabla} - \frac{q}{m}\boldsymbol{A}\right)\Psi\right) \tag{2.2}$$

Here $\hat{P}$ is the momentum operator, q is the charge of the particle, m its mass, $\hbar$ the reduced Planck constant, $\boldsymbol{A}$ is the vector potential and Re indicates the real part the argument. Filling in the wavefunction of Eq. 2.1 yields (omitting the space and time dependencies):

$$\boldsymbol{J} = -\frac{n_\mathrm{s}q^2}{m}\left(\boldsymbol{A} - \frac{\hbar}{q}\boldsymbol{\nabla}\gamma\right) \tag{2.3}$$

Realizing that for Cooper pairs $q = -2e$ (twice the electron charge e), and defining $\Phi_0 = \frac{h}{2e}$, the *magnetic flux quantum*, we can write

---

[1] This is the quantum mechanical analogue of $\boldsymbol{J} = q\boldsymbol{v}n_\mathrm{s}$.

$$\boldsymbol{J} = -\frac{\Phi_0}{2\pi\mu_0\lambda_\mathrm{L}^2}\left(\frac{2\pi}{\Phi_0}\boldsymbol{A} + \nabla\gamma\right) \tag{2.4}$$

Here λ_L is a characteristic length scale of a superconductor, called the *London penetration depth*. Its meaning will become clear under the application of magnetic field, discussed below. It is defined as:

$$\lambda_\mathrm{L} = \sqrt{\frac{m}{4\mu_0 n_\mathrm{s} e^2}} \tag{2.5}$$

Eq. 2.4 is called the *second Ginzburg-Landau eqation* and is one of the central results of Ginzburg-Landau theory describing the phenomenology of superconductivity. Interestingly, electromagnetic fields couple to supercurrents by a linear combination of the vector potential and the phase of the wave function. Since J is a gauge-invariant property, and both $\boldsymbol{A}$ and γ are not, we require the quantity between brackets in Eq. 2.4 to be gauge-invariant. Therefore Eq. 2.4 is often written as:

$$\boldsymbol{J} = \frac{\Phi_0}{2\pi\mu_0\lambda_\mathrm{L}^2}\theta \tag{2.6}$$

Where θ is the called the *gauge-invariant phase gradient*. Clearly, the macroscopic supercurrents are driven by a microscopic quantum mechanical quantity. Therefore, superconductivity is a direct manifestation of quantum effects on the macro scale.

2.2. THE MEISSNER EFFECT AND ITS CONSEQUENCES

In this section, I will describe two more macroscopic properties that result from the quantum nature of the superconducting phase: the zero-resistance state and the Meissner effect. In order to do so, first note that we can combine two of the Maxwell equations ($\nabla \cdot \boldsymbol{B} = 0$ and $\nabla \times \boldsymbol{B} = \mu_0 \boldsymbol{J}$) with some vector calculus to find:

$$\nabla^2 \boldsymbol{B} = \nabla(\nabla \cdot \boldsymbol{B}) - \nabla \times (\nabla \times \boldsymbol{B}) = -\nabla \times (\mu_0 \boldsymbol{J}) \tag{2.7}$$

By virtue of Eq. 2.4, we can obtain the curl of the quantity $\mu_0 \boldsymbol{J}$ in a superconductor, noting that the curl of a gradient is zero:

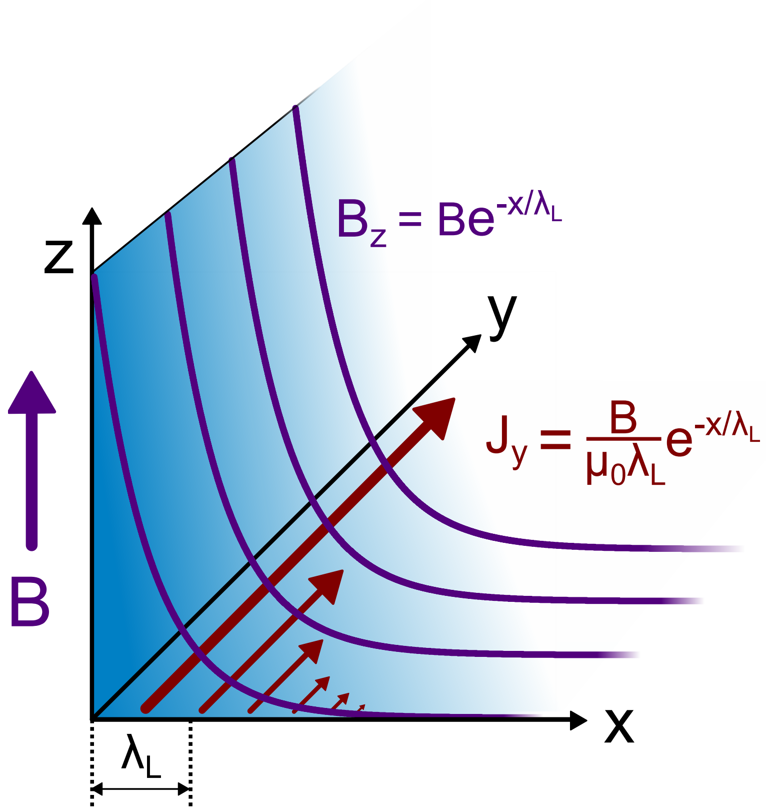
$B_z = Be^{-x/\lambda_L}$
z
y
$J_y = \frac{B}{\mu_0 \lambda_L} e^{-x/\lambda_L}$
B
x
λ_L

Figure 2.1: Schematic representation of the Meissner effect for a superconductor covering $x > 0$, under an applied field B in the z-direction. Due to the Meissner effect, screening currents run along the boundary of the superconductor, i.e., the y,z-plane. These decay exponentially, giving rise to an exponential decay of the magnetic field in the bulk of the superconductor.

$$\nabla \times (\mu_0 \boldsymbol{J}) = -\frac{\nabla \times \boldsymbol{A}}{\lambda_L^2} = -\frac{\boldsymbol{B}}{\lambda_L^2} \tag{2.8}$$

This Equation is known as the *second London equation*. Combined with the identity of Eq. 2.7, it describes the *Meissner effect*:

$$\nabla^2 \boldsymbol{B} = \frac{\boldsymbol{B}}{\lambda_L^2} \tag{2.9}$$

Clearly, a magnetic field in a superconductor decays exponentially over a length scale λ_L, which can be seen if we solve the differential Equation 2.9 for a superconductor covering the space $x > 0$, subject to a field B in the z-direction (see Figure 2.1):

$$B_z(x,y,z) = Be^{-\frac{x}{\lambda_\mathrm{L}}} \tag{2.10}$$

The origin of the exponential decay is a supercurrent that runs along the edge of the superconductor and screens the magnetic field. It is aptly called *screening* or *Meissner current* and is given by $\boldsymbol{\nabla} \times \boldsymbol{B} = \mu_0 \boldsymbol{J}$:

$$J_y(x,y,z) = \frac{B}{\mu_0 \lambda_\mathrm{L}} e^{-\frac{x}{\lambda_\mathrm{L}}} \tag{2.11}$$

These screening currents play an important role in the discussion on Josephson junctions. Since Eq. 2.8 is known as the second London equation, this naturally leads to the question of what the *first London equation* is. The first London equation is derived using a combination between Lorentz's law and the second London equation; it reads in its linearized form[2]:

$$\frac{\mathrm{d}\boldsymbol{J}}{\mathrm{d}t} = \frac{\boldsymbol{E}}{\mu_0 \lambda_\mathrm{L}^2} \tag{2.12}$$

From this Equation, we see that a superconductor can host a stationary supercurrent without the application of an electric field, meaning a zero-resistance state. Interestingly, the first London equation is derived using the second one. This implies that the Meissner effect is a more fundamental property of the condensate than its lack of electrical resistance. The reason why the latter coined the name of the phase can be traced to Heike Kamerlingh Onnes' discovery proceeding that of Walter Meissner. To conclude, the pairing of electrons in Cooper pairs and their entailing change from fermionic to bozonic character directly leads to the expulsion of magnetic fields from the bulk of the solid and the appearance of a zero-resistance state.

2.3. PAIRING SYMMETRY

In section 2.1, I did not discuss the origin of the pairing interaction between the electrons. The microscopic mechanism behind this pairing differs between classes of superconductors and is still the subject of ongoing research, although it is not relevant for the phenomenological description of superconductivity that I present here. However, the symmetry of the wavefunction describing a single Cooper pair will be pivotal for explaining its properties in later chapters. Therefore, I will briefly review this so-called *pairing symmetry*.

---

[2] Here I have omitted a second term which captures the kinetic energy of the electrons composing the Cooper pairs $\frac{\mu_0 \lambda_\mathrm{L}^2 e}{m} \boldsymbol{\nabla} \boldsymbol{J}^2$. This is valid if we assume that the magnetic contribution to Lorentz's law is much smaller than the electric one.

Although the Cooper pair is a bosonic composite particle, its fundamental constituents are fermionic and, therefore, still obey the Pauli exclusion principle. This implies that the wave function describing the pair must be anti-symmetric under the permutation of the two electrons that make up the Cooper pair, which can best be seen by regarding the anomalous Green's function describing the Cooper pair[2]. It is given by the time-ordered expectation value of two electron annihilation operators[3]:

$$f_{\alpha\beta,ab}(\boldsymbol{r}_1,\boldsymbol{r}_2,t_1,t_2) = \langle \mathcal{T}\, \hat{a}_{\alpha,a}(\boldsymbol{r}_1,t_1)\hat{a}_{\beta,b}(\boldsymbol{r}_2,t_2)\rangle \tag{2.13}$$

The Greek indices here indicate the spin state, the alphabetic indices represent the electron band, $\boldsymbol{r}$ is the position coordinate, and t is the time coordinate of each electron (labeled 1 and 2). Therefore, $\hat{a}_{\alpha,a}(\boldsymbol{r},t)$ removes an electron with spin α from electron band with label a, which is located at position $\boldsymbol{r}$ at time t. Creating a Cooper pair requires two electrons, thus f must be of the form $\hat{a}\hat{a}$. The Pauli exclusion principle states that the electrons cannot be in the same quantum state at equal times ($t_1 = t_2 = t$). Therefore, the Pauli exclusion principle is expressed as:

$$f_{\alpha\beta,ab}(\boldsymbol{r}_1,\boldsymbol{r}_2,t,t) = -f_{\beta\alpha,ba}(\boldsymbol{r}_2,\boldsymbol{r}_1,t,t) \tag{2.14}$$

Anti-symmetry can be expressed by permutation of any of the individual components (spin, spatial coordinate, time, and the electron band of the individual electrons. The latter results in interband or intraband pairing). However, only the total wave function of the pair is required to be anti-symmetric, which lets us classify the pairs on the basis of their underlying symmetries. Figure 2.2 depicts a classification scheme for the allowed pairing states.[3] Below, I will discuss the spin, relative position, and time symmetries in more detail.

The Fourier dual of the relative position between the electrons is their angular momentum. As in the case of electrons orbiting a nucleus, the angular momentum of the Cooper pair is described by a quantum number L. Each of its integer values is assigned a letter, i.e., *s*, *p*, *d*, *f* etc. and is subsequently called L-wave (e.g., *s*-wave). This notation is borrowed from molecular physics and was chosen due to the similarity between the shape of the superconducting gap structure and atomic orbitals. *s*-wave and *d*-wave pairs are symmetric and *p*-wave and *f*-wave are anti-symmetric.

---

[3] Creation and annihilation operators are part of the second quantization formulation of quantum mechanics, used in describing BCS theory.

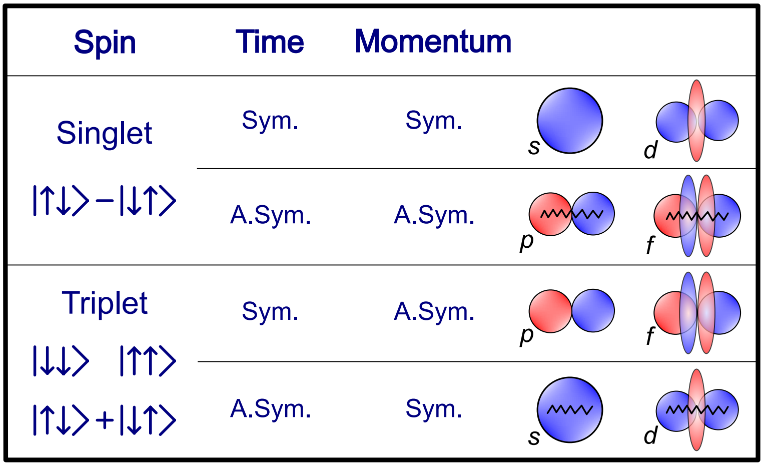

Figure 2.2: Overview of allowed pairing symmetries based on the Pauli exclusion principle. The wavefunction of the Cooper pair is required to be anti-symmetric under the permutation operation, which can result from either the spin, time, or momentum component of the wavefunction. All pairing symmetries can be classified as either spin singlet (S=0) or spin triplet (S=1). The schematics show the resulting allowed pairing symmetries in the last two columns. Here the letter denotes the angular momentum quantum number (Fourier dual of relative position), and the oscillating lines indicate an anti-symmetric time component of the wavefunction. Note that anti-symmetry can also result from interband pairing, which is not shown here. Image adapted from [3].

The spin part of the wavefunction is described by a quantum number S, allowing for two different possibilities: either $S = 0$, which is *singlet pairing*, or $S = 1$, which is called *triplet pairing*. In a singlet pair, the electrons have opposite spin and therefore this is an anti-symmetric state, in Dirac notation: $\frac{1}{\sqrt{2}}(|\uparrow\downarrow\rangle - |\downarrow\uparrow\rangle)$. The triplet state is its symmetric counterpart, where the electrons are paired with equal spin, i.e., $S = 1$, which is divided in three options. Either the electrons have a finite spin projection along the quantization axis($|\uparrow\uparrow\rangle$ and $|\downarrow\downarrow\rangle$) or they have zero spin projection: $\frac{1}{\sqrt{2}}(|\uparrow\downarrow\rangle + |\downarrow\uparrow\rangle)$. *Conventional* superconductors are of singlet *s*-wave nature. The antipathy to magnetic fields, described in section 2.2, is clearly reflected in the opposite spin of the singlet pairs, since magnetic fields tend to align the spins in a solid. Generally, materials with a different pairing symmetry as classified as *unconventional*.

The concept of time asymmetry is less easily grasped at first sight. It is best understood mathematically. Therefore, we return to the anomalous Green's function. The class of superconductors characterized by an asymmetry in time, also called *odd-frequency* pairing, are classified by acquiring a minus sign under exchange of time variables:

$$f_{\alpha\beta,ab}(\boldsymbol{r}_1,\boldsymbol{r}_2,t_1,t_2) = -f_{\alpha\beta,ab}(\boldsymbol{r}_1,\boldsymbol{r}_2,t_2,t_1) \tag{2.15}$$

This means that naturally $f = 0$, when $t_1 = t_2$. Therefore, strictly spoken odd-frequency superconductivity is not a consequence of the Pauli exclusion principle. Instead, it arises due to a constraint on the relative time coordinates of the anomalous Green's function. Yet it does allow for an electron pairing that is symmetric in momentum, spin and electron band that still meets the Pauli exclusion principle.

Pairing symmetry is an important topic in researching superconductivity, which is reflected in this thesis. For example, the pairing symmetry of the unconventional superconductor Sr_2RuO_4, which is the topic in Chapter 7, was thought to be equal-spin triplet p-wave for over 20 years. Only in 2020 this hypothesis was found to be unlikely, and currently, the pairing symmetry of Sr_2RuO_4 is a hotly debated topic: the proposals range from 'shadow-triplet' interband s+id-wave pairing to accidental degeneracies between d- and g-wave pairing[4, 5]. Another manifestation of triplet pairing will be encountered in Chapters 3 and 4, which discuss the proximity effect in a strong ferromagnet. Such superconducting correlations require spin-triplet pairing with finite spin ($|\uparrow\uparrow\rangle$ or $|\downarrow\downarrow\rangle$), exhibiting an odd time component to fulfill the anti-symmetry requirement. Before discussing the proximity effect in ferromagnets, I will introduce the superconducting proximity effect in normal metals in the next section.

2.4. THE PROXIMITY EFFECT AND JOSEPHSON JUNCTIONS

In section 2.1 omitted the space dependence of the superconducting condensate density, but naturally we can ask what governs this space dependence. For this we turn to the *first Ginzburg-Landau equation*, which reads in the absence of magnetic fields:

$$\alpha\psi + \beta|\psi|^2\psi + \frac{\hbar^2}{2m}\nabla^2\psi = 0 \tag{2.16}$$

This equation is derived from minimizing the free energy associated with an order parameter (ψ) near a phase transition. The solution of Eq. 2.16 is expressed in exponential functions that contain a characteristic length scale ξ, called the *coherence length*, which is given in Ginzburg-Laundau theory as[4]:

$$\xi = \sqrt{\frac{\hbar}{2m|\alpha|}} \tag{2.17}$$

This length scale can be interpreted as the distance over which the density of the superconducting condensate can change its magnitude. Since the coherence length is finite, the magnitude of the condensate cannot fall to zero over an infinitesimally small

---

[4] In BCS theory, which I do not discuss in this thesis, the coherence length is defined as well. It signifies the typical length scale corresponding to the pairing interactions and is, therefore, sometimes explained as the average size of the Cooper pair.

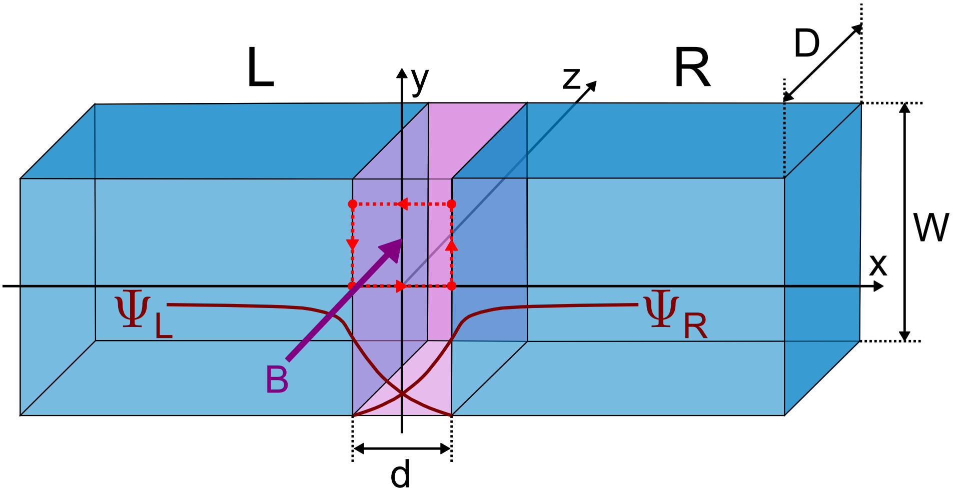

Figure 2.3: Schematic drawing of a Josephson junction: two superconducting leads (blue) separated by thin barrier layer of size d (pink). In dark red the amplitude of the superconducting wavefunctions is shown. As there is overlap between them, there can be a supercurrent flowing through the junction. A uniform magnetic field ($\boldsymbol{B} = B\hat{z}$) is applied to the junction, which results in an interference pattern observed in the critical current $I_\mathrm{c}(B)$ (see section 2.6). This is calculated by computing a contour integral of the gauge covariant-phase gradient over the red dotted contour.

distance, like the interface between a superconductor and a non-superconducting material. Therefore, superconducting effects 'leak' into the material adjacent to the superconductor. This is known as the *superconducting proximity effect*.

The fact that a normal metal can show superconducting effects through the proximity effect raises the question whether a supercurrent can pass from one superconducting electrode to another if separated by a proximized material. The answer is yes, but only if the proximized material is thin enough to let the superconducting wave functions overlap. A sketch of such a geometry is given in Figure 2.3: two superconducting electrodes separated by a so-called *weak link* or *barrier*. This fundamental superconducting element is called a *Josephson junction* and forms the centerpiece of research on superconductors and their technological applications. Generally, the nature of the weak link determines the transport through the junction and can be insulating (I), normal metal (N), or ferromagnetic (F). A normal metal junction is denoted as an S–N–S junction. Chapter 4 will discuss S–F–S junctions; below, I will describe what drives the current through a Josephson junction.

If we assume that the coupling between the two electrodes is weak, the Cooper pair density of the electrodes remains largely unaffected. Instead, supercurrents in the weak link are driven by the gauge-invariant phase gradient, as is the case in the bulk of the superconductor. Specifically, when comparing the phase difference between two sides of the junction, we define the *gauge-invariant phase difference*, which is given by (omitting any z-dependence):

$$\varphi(y) = \int_{-d/2}^{d/2} \theta \, \mathrm{d}l = \gamma(-\frac{d}{2}, y) - \gamma(\frac{d}{2}, y) - \frac{2\pi}{\Phi_0} \int_{-d/2}^{d/2} A_x(x, y) \, \mathrm{d}x \tag{2.18}$$

Since we now know that the current through the junction is given by $\boldsymbol{J} = \boldsymbol{J}(\varphi)$, we can follow the arguments of Landau and Lifschitz to find a relation between the current and the gauge-invariant phase difference, aptly called the *current-phase relation*[6]. From Eq. 2.1 we see that the wavefunction is 2π-periodic in the electrodes. This is consequently transferred to the junction such that $\boldsymbol{J}(\varphi) = \boldsymbol{J}(\varphi + 2\pi)$. Furthermore, in the absence of any phase difference, no currents can be running, which means: $\boldsymbol{J}(2\pi n) = 0$, where n is an integer. Combined, this limits the current-phase relation to the following set of functions:

$$\boldsymbol{J} = \boldsymbol{J}_\mathrm{c} \sin\varphi + \sum_{m=2}^{\infty} \boldsymbol{J}_{\mathrm{c},m} \sin\big(m\varphi\big) \tag{2.19}$$

This current-phase relation is also known as the general formulation of the *first Josephson relation*, after Brian Josephson, who derived it when studying pair-wise tunneling in S−I−S junctions[7]. More commonly, in the case of weak coupling between the two electrodes, we can neglect the higher harmonics, and Eq. 2.19 is reduced to:

$$\boldsymbol{J} = \boldsymbol{J}_\mathrm{c} \sin\varphi \tag{2.20}$$

Here $\boldsymbol{J}_\mathrm{c}$ is the maximum current density the junction can sustain, called the *critical current density*. Above this current, a finite voltage is measured over the junction. This manifests itself as a *critical current* (I_c) during the measurement of the IV-characteristic of a junction, which is the most fundamental measurement of a Josephson junction, repeated many times throughout this thesis. In such measurement, a DC current is applied through the junction, and the voltage across the junction is recorded (see Figure 2.4). More technical details on obtaining IV-characteristics and the set-up used to gather the data presented in this thesis are provided in Appendix A. The remarkably simple result of Eq. 2.20 is yet another manifestation of macroscopic currents driven by the microscopic quantum mechanical phase, leading to junction properties that reveal the wave-like nature of the condensate. Two of those, I will review below.

2.5. SHAPIRO STEPS

In the previous section we found a relation between the current through a junction and the gauge-invariant phase difference over the junction. How is this related to an electric field applied to the junction? Electric (E)-fields can be written as a linear combination between a scalar potential (ϕ) and a vector potential ($\boldsymbol{A}$):

$$\boldsymbol{E} = -\frac{\mathrm{d}\boldsymbol{A}}{\mathrm{d}t} - \nabla\phi \tag{2.21}$$

Also, from the time-dependent Schrödinger equation, one can show that the time evolution of the gauge covariant phase follows:

$$-\hbar\frac{\mathrm{d}\gamma}{\mathrm{d}t} = \frac{\mu_0\lambda_{\mathrm{L}}^2}{2n_{\mathrm{s}}}\boldsymbol{J}^2 + 2e\phi \tag{2.22}$$

This can be combined with Eq. 2.18, to obtain the time evolution of the gauge invariant phase difference:

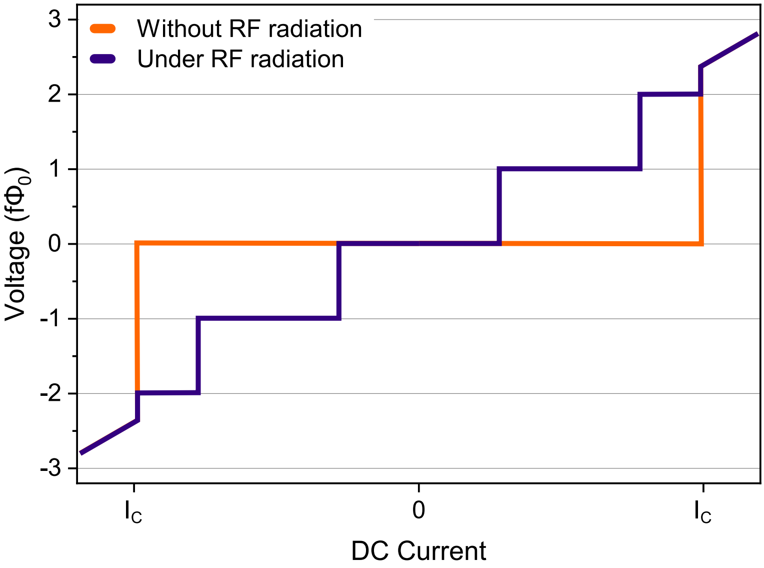

Figure 2.4: A schematic example of an IV-characteristic of a junction. If no microwave radiation is applied to the junction (orange curve), zero voltage is measured over the junction, as long as the current does not exceed the critical current I_C. Irradiation with RF-radiation results in quantized voltage steps that are spaced by $\Delta V = f\Phi_0$, which are called Shapiro steps. The measurement of a IV-characteristic is the most fundamental measurement in this thesis and is widely used to extract the critical current of Josephson junctions.

$$\frac{\mathrm{d}\varphi}{\mathrm{d}t} = -\frac{1}{\hbar}\left(\frac{\mu_0\lambda_\mathrm{L}^2}{2n_\mathrm{s}}\left(\boldsymbol{J}^2(\frac{d}{2}) - \boldsymbol{J}^2(-\frac{d}{2})\right) + 2e\phi\right) - \frac{2\pi}{\Phi_0}\int_{-d/2}^{d/2}\frac{\mathrm{d}A_x(x,y)}{\mathrm{d}t}\,\mathrm{d}x \tag{2.23}$$

Since the current is conserved in the junction ($\boldsymbol{J}^2(\frac{d}{2}) = \boldsymbol{J}^2(-\frac{d}{2})$), we can write:

$$\frac{\mathrm{d}\varphi}{\mathrm{d}t} = \frac{2\pi}{\Phi_0}\int_{-d/2}^{d/2} -\frac{\mathrm{d}\phi}{\mathrm{d}x} - \frac{\mathrm{d}A_x(x,y)}{\mathrm{d}t}\,\mathrm{d}x \tag{2.24}$$

Here we recognize the expression from Eq. 2.21 and we arrive at the *second Josephson equation*:

$$\frac{\mathrm{d}\varphi}{\mathrm{d}t} = \frac{2\pi}{\Phi_0}\int_{-d/2}^{d/2} E_x\,\mathrm{d}x = \frac{2\pi}{\Phi_0}V \tag{2.25}$$

The consequence of this equation is that a finite voltage V over the junction, entails a linear increase of the gauge invariant phase difference in time ($\varphi = \frac{2\pi}{\Phi_0}Vt$). Combining this with the current-phase relation, yields:

$$\boldsymbol{J} = \boldsymbol{J}_\mathrm{c}\sin\frac{2\pi}{\Phi_0}Vt \tag{2.26}$$

In other words, the application of a constant DC voltage yields an AC current through the junction with a frequency of $f = \frac{V}{\Phi_0}$, which translates to roughly 500 MHz per applied μV. The inverse of this effect can be encountered throughout this thesis. If a junction is irradiated with RF-radiation while driving a DC supercurrent through the junction, phase locking between the radiation and the supercurrents occurs. This results in a DC voltage over the junction, which appears as quantized steps in the IV-characteristic, spaced by $\Delta V = f\Phi_0$. These steps are called *Shapiro steps*; a schematic example of which is shown in Figure 2.4.

The measurement of Shapiro steps serves as definitive evidence for the Josephson effect without the use of static magnetic fields that might, for example, alter the magnetic texture of the S–F–S Josephson junctions presented in Chapter 4 and 5. Furthermore, they are conclusive proof of the emergence of spontaneous Josephson junctions in mesoscopic Sr_2RuO_4 structures, discussed in Chapter 7. Besides, the detection of Shapiro steps enables us to examine the periodicity of the current-phase relation. If the current-phase relation is not 2π periodic, for example, fractional Shapiro steps can be observed when it is dominated by a higher harmonic.

2.6. MAGNETIC INTERFERENCE IN A JOSEPHSON JUNCTION

One of the most fundamental measurements of a Josephson junction is the dependence of critical current on a magnetic field applied perpendicular to the junction (e.g., the y-direction or z-direction in Figure 2.3). Experimentally this is also known as superconducting quantum interferometry measurements, i.e., obtaining the $I_c(B)$-pattern of a junction. To calculate the expected $I_c(B)$, define a narrow rectangular loop of width d, with the bottom located at the origin and a height y (See the dotted contour in Figure 2.3). We integrate $\boldsymbol{\nabla}\gamma$ (using Eqs. 2.3 and 2.18) along this path to obtain[5]:

$$0=\int_{\mathrm{C}} \boldsymbol{\nabla}\gamma\,\mathrm{d}\boldsymbol{l}=-\varphi(y)+\varphi(0)+\frac{2\pi}{\Phi_0}\int_{\mathrm{C}}\boldsymbol{A}\,\mathrm{d}\boldsymbol{l}+\frac{2\pi\mu_0\lambda_{\mathrm{L}}^2}{\Phi_0}\left(\int_0^y J_{y,R}(\frac{d}{2},y')\,\mathrm{d}y'+\int_y^0 J_{y,L}(-\frac{d}{2},y')\,\mathrm{d}y'\right) \tag{2.27}$$

Using Stokes theorem, we can transform the integral over the vector potential into one over the magnetic field that penetrates the integration contour, resulting in the magnetic field flux ($\Phi = ydB$). Furthermore, in the case of a symmetric geometry: $J_{y,R}(\frac{d}{2},y') = -J_{y,L}(-\frac{d}{2},y')$. Therefore we find for $\varphi(y)$:

$$\varphi(y)=\varphi(0)+\frac{2\pi}{\Phi_0}\left(ydB+2\mu_0\lambda_{\mathrm{L}}^2\int_0^y J_{y,R}(\frac{d}{2},y')\,\mathrm{d}y'\right)=\varphi(0)+\varphi_B \tag{2.28}$$

We recognize two parts in $\varphi(y)$: the first, $\varphi(0)$ is the phase difference at the origin. This can be thought of as the phase difference resulting due to a current or voltage bias between the two electrodes. The second, φ_B, results from the magnetic induction to the junction (see the inset of Figure 2.5). The current that runs along the junction might not be trivial to compute. However, in the case of a junction between two macroscopic superconducting leads, we have already found this quantity in the form of the Meissner effect (Eq. 2.11). At the boundary we have $J_{y,R}(\frac{d}{2},y') = \frac{B\mu_0}{\lambda_{\mathrm{L}}}$; filling in yields:

$$\varphi(y)=\varphi(0)+\frac{2\pi(2\lambda_{\mathrm{L}}+d)B}{\Phi_0}y=\varphi(0)+\frac{2\pi L_{\mathrm{eff}}B}{\Phi_0}y \tag{2.29}$$

Where in the right-hand side we defined the *effective junction length* $L_{\mathrm{eff}} = 2\lambda_{\mathrm{L}} + d$. We see that φ_B scales with fields penetrating the barrier and with fields penetrating the electrodes over a length scale λ_{L} on either side of the junction. Therefore L_{eff} can be considered as the length of the Josephson junction. Using the current-phase relation

---

[5] Actually $\int_{\mathrm{C}}\boldsymbol{\nabla}\gamma\,\mathrm{d}\boldsymbol{l} = 2\pi n$, but we can set $n = 0$ if the current-phase relation is dominated by the first harmonic. In that case: $\sin(\varphi+2\pi n) = \sin(\varphi)$.

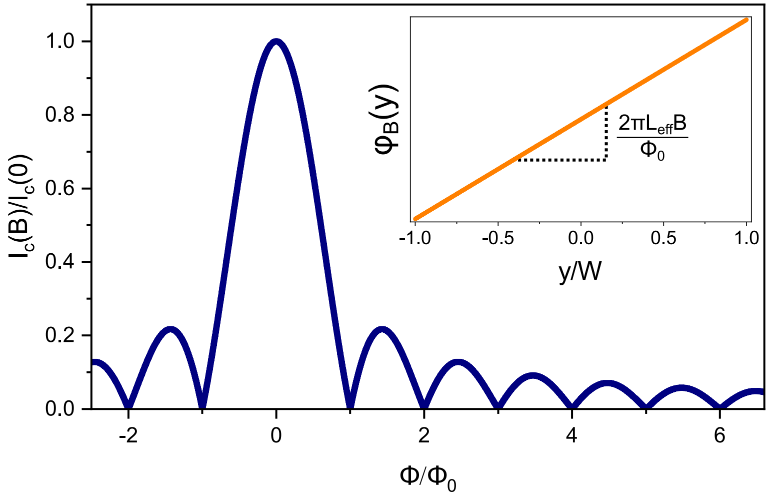

Figure 2.5: The interference pattern of the critical current in a Josephson junction due to the application of a field $I_c(B)$. This result corresponds to a typical Fraunhofer interference pattern commonly observed in optical diffraction patterns. The inset shows the gauge-invariant phase difference resulting from the magnetic induction to the junction, as a function of the length parameter running along the junction.

(Eq. 2.20), we can find the current that passes through the junction as a function of field:

$$I(B) = \int \boldsymbol{J}\,\mathrm{d}\boldsymbol{S} = \int_{-W/2}^{W/2} D J_c \sin\left(\varphi(0) + \frac{2\pi L_{\text{eff}} B}{\Phi_0} y\right) \mathrm{d}y \tag{2.30}$$

For now we assume that the critical current density at zero field is distributed uniformly over the junction, yielding $J_c = \frac{I_c(0)}{DW}$. Also, note that $\varphi(0)$ is independent of y and therefore merely is a phase factor. Therefore, the critical current is reached if we current-bias the junction by setting $\varphi(0) = \pi/2$, from which follows:

$$\frac{I_c(B)}{I_c(0)} = \left|\frac{1}{W}\int_{-W/2}^{W/2} \cos\left(\frac{2\pi L_{\text{eff}} B}{\Phi_0} y\right) \mathrm{d}y\right| = \left|\frac{\sin\left(\frac{\pi L_{\text{eff}} W B}{\Phi_0}\right)}{\frac{\pi L_{\text{eff}} W B}{\Phi_0}}\right| = \left|\frac{\sin\left(\frac{\pi \Phi}{\Phi_0}\right)}{\frac{\pi \Phi}{\Phi_0}}\right| \tag{2.31}$$

Here Φ is the total flux penetrating the junction. This result is the classic Fraunhofer pattern, obtained in an optical diffraction experiment of light waves in a single slit. I plot this result in Figure 2.5. Here we see a clear example of the wave-like nature of the condensate determining the macroscopic properties of the junction. As discussed below, measuring the magnetic interference pattern of the critical current is the ideal tool for understanding supercurrent transport in a Josephson junction.

2.7. EXTRACTING THE SUPERCURRENT DENSITY WITH FOURIER ANALYSIS

In the discussion so far, I assumed a uniform distribution of critical current throughout the weak link. In their 1971 paper, Dynes and Fulton [8] relax this criterion and discuss a relation between the shape of the SQI pattern and the supercurrent distribution in a junction. They realized that the current distribution in the junction can be extracted by complex inverse Fourier transform of $I_\mathrm{c}(B)$. For simplicity, consider a J_c that only has a y-dependence, such that:

$$I(B) = \int \boldsymbol{J}\, \mathrm{d}\boldsymbol{S} = \left| \int_{-W/2}^{W/2} D J_\mathrm{c}(y) \sin\left(\varphi(0) + \varphi_B\right) \mathrm{d}y \right| = \mathrm{Im}\left(e^{i\varphi(0)} \int_{-\infty}^{\infty} J_\mathrm{c}(y) e^{i\varphi_B}\, \mathrm{d}y \right) \tag{2.32}$$

On the right-hand side, the integration bounds have been extended to infinity since there are no supercurrents outside the sample boundaries, and therefore the integral is zero. Besides, I dropped the D, so J_c can be considered as the critical current density per unit length. The critical current is given by the absolute value of the complex expression. Note that this equal to setting $\varphi(0) = \pi/2$ in Eq. 2.31.

$$I_\mathrm{c}(B) = \left| \int_{-\infty}^{\infty} J_\mathrm{c}(y) e^{i\varphi_B(B,y)}\, \mathrm{d}y \right| = |\mathfrak{I}_\mathrm{c}| \tag{2.33}$$

From this equation a general expression for a Fourier transform can be recognized; conceptually depicted in Figure 2.6. For a junction with macroscopic leads discussed above, we have $\varphi_B(B,y) = \frac{2\pi L_\mathrm{eff} B}{\Phi_0} y$ and therefore:

$$I_\mathrm{c}(\beta) = \left| \int_{-\infty}^{\infty} J_\mathrm{c}(y) e^{2\pi i \beta y}\, \mathrm{d}y \right| \tag{2.34}$$

Here we have defined the reduced field $\beta = \frac{L_\mathrm{eff} B}{\Phi_0}$, such that the position along the junctions y and β form conjugate variables. The Fourier relation of Eq. 2.34, interestingly, gives rise to the possibility of extracting $J_\mathrm{c}(y)$ by inverse Fourier transform of $I_\mathrm{c}(B)$. This allows for studying the edge supercurrents in, for example, topological and semiconductor-based S–N–S junctions[9–12]. It also plays an important role in determining the rim currents in Chapter 4. In the next chapter, I will describe the technical details of the Fourier transform and its use to analyze experimental data. In light of the subject of this thesis, we are specifically interested in mesoscopically sized samples. Therefore we need to adjust the theory from this chapter first accordingly, which is the topic of the next chapter.

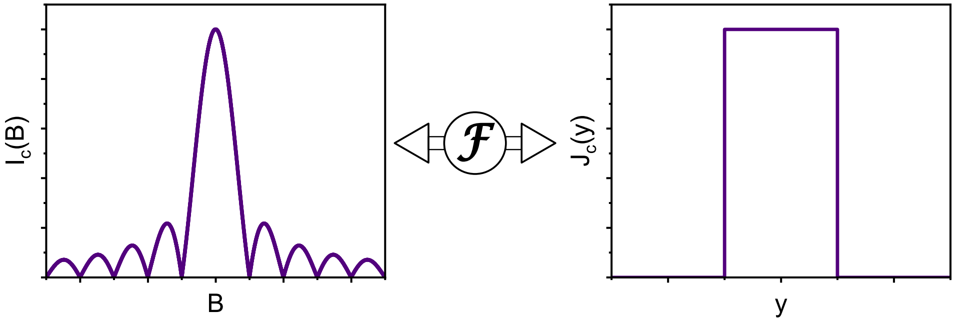

Figure 2.6: Conceptual representation of the Fourier relation between the magnetic interference pattern of the junction and the distribution of critical current density throughout said junction. For example, a uniform $J_\mathrm{c}(y)$ leads to a Fraunhofer interference pattern. Practically, $I_\mathrm{c}(B)$ is used to examine $J_\mathrm{c}(y)$, which is a powerful tool to find possible current channels in a junction, when the interference pattern deviates from the Fraunhofer case.

APPENDICES

A. EXPERIMENTAL SET-UP AND MEASUREMENT PROCEDURE

The data presented in this thesis is acquired in an Oxford Instruments IntegraAC cryostat equipped with a vector magnet, aptly called the Vectormagnet. Since it features a vector magnet, it can apply a one Tesla magnetic field in any direction, and on top of that, it can reach a 6 T and 2 T magnetic field along two specified directions. The Vectormagnet is a ‘wet cryostat,’ having a dewar with liquid ^{4}He. It cools samples by letting in liquid ^{4}He in the cooling chamber. The spent helium is recycled and liquefied by the integrated pulse tube attached to the dewar. We have two different inserts (sample rods) for measurements: the high-T insert and the Heliox insert. The first is a home-built insert capable of reaching a 1.5 K base temperature, which is the base-T of the Vectormagnet sample chamber. The Heliox insert contains an inner vacuum chamber with an integrated ^{3}He system that is capable of reaching sub-300 mK temperatures. Finally, in both inserts, we can irradiate samples with RF radiation using an open-ended coax cable antenna placed in close proximity to the samples.

Considerable effort was put into the grounding of the Vectormagnet and its inserts. The entire system has a single ground connection to prevent ground loops; the rest of the physical or electrical grounds are decoupled by plastic o-rings and low-pass filters, respectively. The computer that controls the Vectormagnet is decoupled electrically from the measurement equipment by a purely optical data transmission system. To further reduce the electrical noise, only the measurement wire cores are used for measurements. The wire shields are always connected to the ground of the Vectormagnet.

Independent of the measurement insert, we have both DC and AC measurement equipment available. First, we can apply DC currents using a Keithley 6221 current source and obtain DC voltages using a Keithley 2182A volt meter. We can also obtain AC voltages using a Synktek MCL1-540 multichannel lock-in. The latter allows the simultaneous measurements of up to 6 AC voltages. Therefore, we can measure many samples at the same time. Besides, we can use the MCL1-540 in combination with a shunt resistor to generate a DC bias current that is superimposed on the AC current. Therefore, the Synktek lock-in can also be used to obtain IV-characteristics of the samples. In conclusion, using the equipment described above, we can measure voltages as a function of several parameters:

$$V(I_{\mathrm{DC}}, I_{\mathrm{AC}}, T, \boldsymbol{B}, f_{\mathrm{RF}}, P_{\mathrm{RF}}) \tag{2.35}$$

Here I_{DC} and I_{AC} are the applied DC and AC current, T is the sample temperature, $\boldsymbol{B}$ the applied magnetic field, f_{RF} is the frequency of the applied RF radiation, and P_{RF} the power of the applied RF radiation. In practice, we scan the parameter space with the Vectormagnet and use the measured voltages to extract the properties of our samples. For example, the resistance is defined using a DC measurement as:

$$R(I_{\mathrm{DC}}) = \frac{V_{\mathrm{DC}}(I_{\mathrm{DC}}) - V_{\mathrm{DC}}(-I_{\mathrm{DC}})}{2I_{\mathrm{DC}}} \tag{2.36}$$

Likewise, we establish the resistance using the lock-in as:

$$R(I_{\mathrm{AC}}) = \frac{V_{\mathrm{AC}}(I_{\mathrm{AC}})}{I_{\mathrm{AC}}} \tag{2.37}$$

Another example is the critical current (I_{c}) of a Josephson junction. It is defined as the current corresponding to a voltage measured over the junction that exceeds a certain threshold value (typically chosen just larger than the noise floor).

REFERENCES

[1] Gross, R. & Marx, A. Applied superconductivity: Josephson effect and superconducting electronics (2005). https://www.wmi.badw.de/teaching/lecture-notes (accessed: 28-2-22).

[2] Linder, J. & Balatsky, A. V. Odd-frequency superconductivity. *Rev. Mod. Phys.* **91**, 045005 (2019).

[3] Eschrig, M. & Löfwander, T. Triplet supercurrents in clean and disordered half-metallic ferromagnets. *Nat. Phys.* **4**, 138–143 (2008).

[4] Kivelson, S. A., Yuan, A. C., Ramshaw, B. J. & Thomale, R. A proposal for reconciling diverse experiments on the superconducting state in Sr_2RuO_4. *npj Quantum Mater.* (2020).

[5] Clepkens, J., Lindquist, A. W. & Kee, H.-Y. Shadowed triplet pairings in hund's metals with spin-orbit coupling. *Phys. Rev. Res.* **3**, 013001 (2021).

[6] Landau, L. D. & Lifschitz, E. M. *Course of theoretical physics Vol. 9: Statistical physics 2* (Pergamon Press, Oxford, UK, 1980).

[7] Josephson, B. Possible new effects in superconductive tunnelling. *Phys. Lett.* **1**, 251–253 (1962).

[8] Dynes, R. C. & Fulton, T. A. Supercurrent density distribution in Josephson junctions. *Phys. Rev. B* **3**, 3015–3023 (1971).

[9] Hart, S. *et al.* Induced superconductivity in the quantum spin Hall edge. *Nat. Phys.* **10**, 638–643 (2014).

[10] Huang, C. *et al.* Proximity-induced surface superconductivity in Dirac semimetal Cd_3As_2. *Nat. Commun.* **10**, 2217 (2019).

[11] Suominen, H. J. *et al.* Anomalous Fraunhofer interference in epitaxial superconductor-semiconductor Josephson junctions. *Phys. Rev. B* **95**, 035307 (2017).

[12] de Vries, F. K. *et al.* h/e superconducting quantum interference through trivial edge states in InAs. *Phys. Rev. Lett.* **120**, 047702 (2018).

3

REDUCING DIMENSIONS: THE THIN FILM PLANAR JOSEPHSON JUNCTION

R. Fermin, B. de Wit & J. Aarts

The magnetic field dependent critical current $I_c(B)$ of a Josephson junction is determined by the screening currents in its electrodes. In macroscopic junctions, a local vector potential drives the currents, however, in thin film planar junctions, with electrodes of finite size and various shapes, they are governed by non-local electrodynamics. This complicates the extraction of parameters such as the geometry of the effective junction area, the effective junction length and, the critical current density distribution from the $I_c(B)$ interference patterns. In Phys. Rev. B, ***81****, 144515 (2010), John Clem derived $I_c(B)$ for Josephson junctions separating a rectangular superconducting strip of length L and width W. In this chapter, we will extend his technique to find $I_c(B)$ for junctions with ellipsoid and rhomboid geometries. We find the periodicity of the interference pattern ΔB to have common limits for $L \gg W$ and $L \ll W$, independent of the geometry. By fabricating elliptically shaped $S-N-S$ junctions with various aspect ratios, we experimentally verify the L/W dependence of ΔB. We show that these results greatly affect the Fourier relation between $I_c(B)$ and the distribution of critical current in the junction, which makes incorporating these alterations essential for the correct analysis of current channels in topological and magnetic planar Josephson junctions.*

A paper based on this chapter is under review for publication in *Phys. Rev. B* and is published as preprint at arXiv.org under the identifier 2210.05388.

3.1. INTRODUCTION

The previous chapter deals with junctions that are orders of magnitude larger than the physical length scales governing their physics. The discussion of Josephson junctions and their associated interference patterns becomes radically different when the size of the superconducting electrodes is constricted in one or more dimensions. Specifically, when the junction is formed between two superconducting thin films, with a thickness below λ_L, the shielding current running along the junction, responsible for the shape and periodicity of the magnetic interference in the critical current $I_c(B)$, is no longer determined by the Meissner effect in its macroscopic form (i.e., by the local vector potential). Rather non-local electrodynamic effects start to play a role[1–4]. This can be understood by considering that the magnitude of the shielding currents remains the same when the thickness of the superconducting electrode is decreased (there are no sample dimensions in Eq. 2.11). Therefore, the current density in the electrodes increases, and it becomes energetically favorable to extend the shielding currents deeper into the electrodes, yielding a larger penetration depth or effective junction length. In numerous theoretical and experimental studies, it was found that in thin film planar junctions, $I_c(B)$ becomes completely independent of λ_L and is solely determined by the geometry of the sample[4–8]. Moreover, John Clem provided a method to calculate $I_c(B)$ for planar junctions that are also restricted in their lateral size, i.e., a Josephson junction separating a rectangular superconducting strip of width W and length L in two halves[7].

In light of the disk- and ellipse-shaped thin film planar S−F−S junctions presented in Part two, we will review his technique in this chapter and extend his work by covering two more geometries: the ellipse and the rhomboid, both of width W and length L. First, we calculate $I_c(B)$ for these geometries and extract the periodicity of the interference pattern ΔB for different ratios of L/W. Next, we experimentally verify the geometry dependence of ΔB by fabricating elliptically shaped S−N−S junctions with different ratios of L/W. Finally, we analyze how the Fourier relation between $I_c(B)$ and the critical current density distribution is altered for these planar junctions. We find that adapting the Fourier transform is crucial in predicting the location of possible current channels in thin film planar junctions.

3.2. REVIEW OF THE CLEM MODEL

As we examine the thin film limit, the screening current density is uniform in the film, which effectively reduces the problem to a semi-2D one. Therefore, we consider a normal metal Josephson junction (dimensions W and d) that divides a symmetric superconducting thin film into two halves. We specifically consider the junction to be in the short junction limit, as the original model by Clem treats an infinitesimally thin insulating tunnel junction. Furthermore, it is assumed that the electrode the electrode

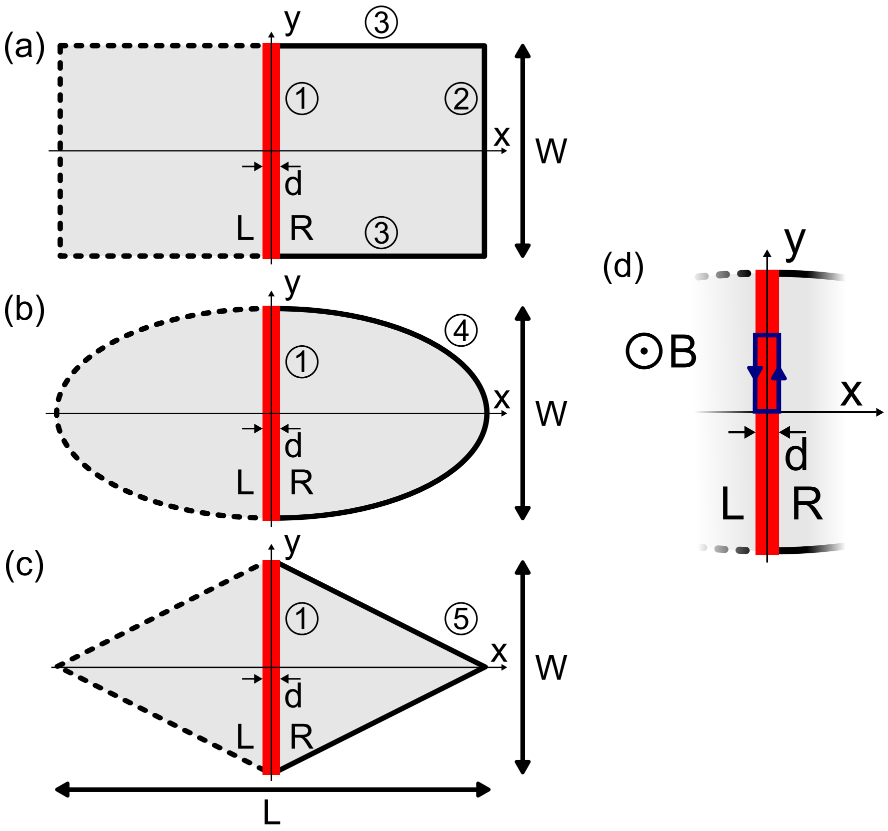

Figure 3.1: Schematics of the three geometries used for calculations in this chapter, being (a) the rectangle, (b) the ellipse and (c) the rhombus. They resemble superconducting thin films of width W and length L, which are separated by a normal metal junction of width d (colored red). By numbers we indicate different sections of the right electrode edge. The boundary conditions for these are summarized in Table 3.1. In (d) we show a zoom of the junction area under the magnetic induction $\boldsymbol{B} = B\hat{z}$. The dark blue path is used as loop integral to determine $I_c(B)$.

dimensions are smaller than the Pearl length, given by:

$$\Lambda = \frac{2\lambda_L^2}{t_{\text{film}}} \tag{3.1}$$

Here t_{film} the thickness of the superconducting films. This implies that the self fields of the screening currents are far smaller than the applied external field. Additionally we assume that the junction is in the narrow limit, meaning that the junction is less wide than the Josephson penetration length, which for planar junctions in the thin film limit is the given by[4, 5, 7]:

$$l = \frac{\Phi_0 t_{\mathrm{junc}} W}{4\pi\mu_0\lambda_{\mathrm{L}}^2 I_{\mathrm{c}}(0)} \tag{3.2}$$

Here t_{junc} is the thickness of the junction. Figure 3.1 shows a schematic of three of such films, having different geometries. The junction, colored red in Figure 3.1, is running along the y-direction from $-W/2$ to $W/2$. In Figure 3.1d, we sketch a zoom of a junction, where we specify the integration contour (similar to Figure 2.3) under a magnetic induction of $\boldsymbol{B} = B\hat{z}$. In order to calculate $I_{\mathrm{c}}(B)$, the current running along this integration contour $J_y(\frac{d}{2}, y)$ needs to be evaluated. To do so, first note that the supercurrent is conserved and therefore $\boldsymbol{\nabla}\cdot\boldsymbol{J} = 0$. By choosing the convenient gauge $\boldsymbol{A} = -yB\hat{x}$, we find $\nabla\times\boldsymbol{A} = B\hat{z} = \boldsymbol{B}$ and $\nabla\cdot\boldsymbol{A} = 0$. Therefore, the divergence of the second Ginzburg-Landau equation (Eq. 2.4) reduces to:

$$\nabla^2\gamma = 0 \tag{3.3}$$

Here γ is the gauge-covariant phase of the superconducting wave function, and we recognize that we mapped the second Ginzburg-Landau equation onto the Laplace equation. With sufficient boundary conditions, it can be solved for a unique solution, which allows us to calculate $J_y(\frac{d}{2}, y)$. The boundary conditions arise from the prerequisite that no supercurrent can exit the sample at its outer boundaries. Furthermore, we assume a weak Josephson coupling, meaning that the shielding currents in the electrodes are far larger than the Josephson currents between the electrodes, which we approximate as $J_x(\frac{d}{2}, y) = 0$. Therefore we can write:

$$\boldsymbol{J}\cdot\hat{\boldsymbol{n}}_{\mathrm{R}} = 0 \tag{3.4}$$

Where $\hat{\boldsymbol{n}}_{\mathrm{R}}$ is the unit vector, normal to the outer edges of the right electrode. Combined with the second Ginzburg-Landau equation, this leads to a set of Neumann boundary conditions:

$$(\boldsymbol{\nabla}\gamma)\cdot\hat{\boldsymbol{n}}_{\mathrm{R}} = -\frac{2\pi}{\Phi_0}\boldsymbol{A}\cdot\hat{\boldsymbol{n}}_{\mathrm{R}} \tag{3.5}$$

Which is sufficient to solve for $\gamma(x, y)$. Next, Eq. 2.28 allows us to find the gauge-invariant phase difference over the junction $\varphi(y)$. Note that we have conveniently chosen $A_{\mathrm{y}} = 0$. We then find:

$$2\mu_0\lambda_{\mathrm{L}}^2\int_0^y J_{y,R}\left(\frac{d}{2},y'\right)\mathrm{d}y' = 2\int_0^y \frac{\mathrm{d}\gamma}{\mathrm{d}y'}\left(\frac{d}{2},y'\right)\mathrm{d}y' = 2\gamma\left(\frac{d}{2},y\right) \tag{3.6}$$

Therefore, $\varphi(y)$ is given by the simple expression:

$$\varphi(y) = \varphi(0) + \frac{2\pi dB}{\Phi_0}y + 2\gamma\left(\frac{d}{2},y\right) \tag{3.7}$$

Finally, $I_c(B)$ is found by following the discussion in Chapter 2:

$$\frac{I_c(B)}{I_c(0)} = \frac{1}{W}\left|\int_{-W/2}^{W/2}\cos\left(\frac{2\pi dB}{\Phi_0}y + 2\gamma\left(\frac{d}{2},y\right)\right)\mathrm{d}y\right| \tag{3.8}$$

We see that finding $I_c(B)$ becomes equal to a boundary condition problem of solving the Laplace equation in the geometry of the electrodes. Indeed, the solution is completely determined by the geometry of the sample and is independent of λ_{L}.

3.3. COMPARING DIFFERENT GEOMETRIES

As it is not trivial to find a general analytical solution to the boundary problem of Eq. 3.3 for the ellipsoid and rhomboid geometries, we solve the Laplace equation numerically using COMSOL Multiphysics 5.4. We define the right electrode geometry in 2D, divided into a triangular grid, on which COMSOL carries out the calculations. Crucial for correctly solving Eq. 3.3, is a grid size that is small enough to capture small changes

Boundary	$(\nabla\gamma)\cdot\hat{\boldsymbol{n}}_\Omega$
①	$\frac{2\pi B}{\Phi_0}y$
②	$-\frac{2\pi B}{\Phi_0}y$
③	0
④	$\frac{2\pi B}{\Phi_0}\frac{Wxy}{L\sqrt{(\frac{Wx}{L})^2+(\frac{Ly}{W})^2}}$
⑤	$-\frac{2\pi B}{\Phi_0}\frac{Wy}{\sqrt{W^2+L^2}}$

Table 3.1: The Neumann boundary conditions for each edge section, listed by the numbering used in Figure 3.1.

in γ and, on the edges, $\hat{\boldsymbol{n}}_\mathrm{R}$. We found a maximum element size (i.e., the grid edge size) of $0.01 \ln(1 + L/W)$ nanometer to be a good compromise between computation time and precision. Using trigonometry we evaluate $\boldsymbol{A} \cdot \hat{\boldsymbol{n}}_\mathrm{R}$ for each geometry and list the corresponding boundary conditions in Table 3.1 (here the numbering corresponds to the numbers in Figure 3.1).

3.3.1. SIMULATION RESULTS

Clem showed that the analytical solution for the rectangular geometry is an infinite series of sines and hyperbolic tangents. For the rectangle, this leads to the maximum in $\gamma\left(\frac{d}{2}, y\right)$ to occur at $W/2$, which can be approximated as:

$$\gamma\left(\frac{d}{2}, \frac{W}{2}\right) = \frac{7\,\zeta(3)}{\pi^2} \frac{BW^2}{\Phi_0} \tanh\left(\frac{\pi^3}{28\,\zeta(3)} \frac{L}{W}\right) \tag{3.9}$$

Here ζ is the Riemann zeta function. Now we generalize this approximation to include the other geometries. We find that the simulated $\gamma\left(\frac{d}{2}, y\right)$ universally follows:

$$\gamma\left(\frac{d}{2}, y\right) = \frac{7\,\zeta(3)}{\pi^2} \frac{BW^2}{\Phi_0} \tanh\left(\frac{\pi^3}{28\,\zeta(3)} \frac{A}{W^2}\right) f\left(\frac{y}{W}\right) \tag{3.10}$$

Where $f\left(\frac{y}{W}\right)$ is a dimensionless function defined by the specific geometry and A is the total surface area of the electrodes. Note that we have substituted $\frac{L}{W}$ in the argument of the hyperbolic tangent for $\frac{A}{W^2}$; the reason for this choice will become apparent below when discussing the period of the $I_\mathrm{c}(B)$-pattern. Figure 3.2a shows the calculated $\gamma(x, y)$ for a disk geometry (i.e., an ellipse where $L = W$), normalized to the applied magnetic field and width of the junction $\gamma\Phi_0/BW^2$. We plot $f\left(\frac{y}{W}\right)$ for this disk in Figure 3.2b. Since $\gamma(y)$ (and therefore $\varphi(y)$ as well) scale linearly with the magnetic field, we can evaluate the integral of Eq. 3.8 numerically for different values of B. The resulting interference pattern (Figure 3.2c) resembles a Fraunhofer pattern at first sight. However, the peak height decreases less strongly than $1/B$, and the width of the middle lobe is not twice the width of the side lobes. In the inset of Figure 3.2c, we plot the width of the nth side lobe (ΔB_n); the width increases and reaches an asymptotic value for large n.

In order to compare the interference patterns of junctions of different geometry, we define the period of the oscillations to be the width of the fifth side lobe ($\Delta B = \Delta B_5$). In the inset of Figure 3.2c, this is shown by the vertical reference line. The width of the fifth side lobe is not only sufficiently close to the asymptotic value but also experimentally accessible without the need for large magnetic fields. We now compare the periodicity of the interference patterns for different geometries by plotting the dimensionless

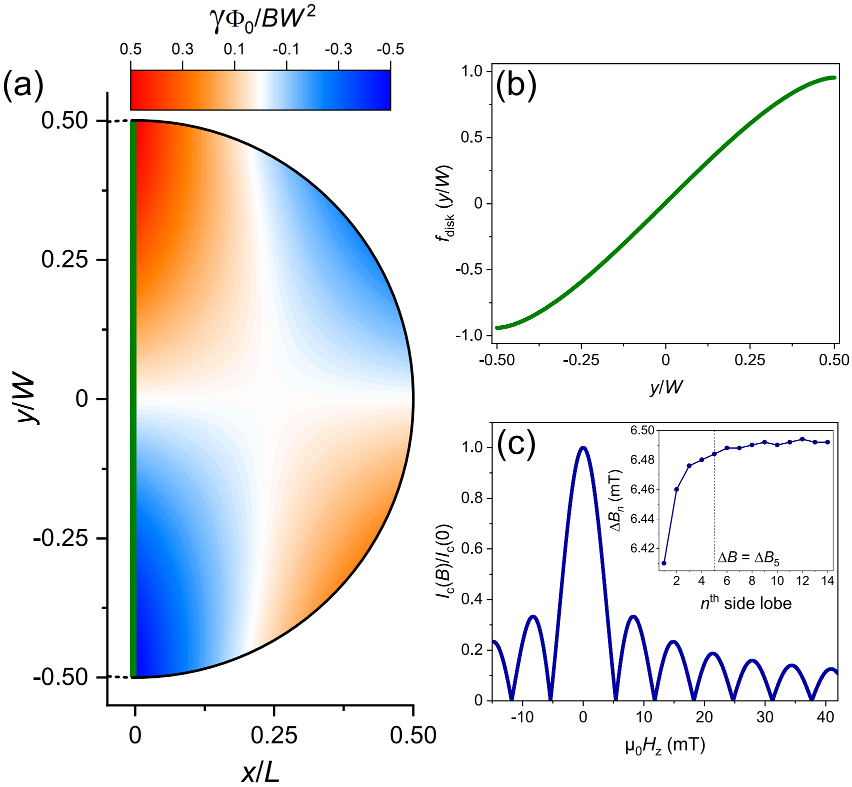

Figure 3.2: (a) Gauge-covariant phase simulated in the right electrode of a disk-shaped planar Josephson junction, normalized to the applied magnetic field and width of the junction $\gamma\Phi_0/BW^2$. The junction is shown as a green line. This result lets us extract the gauge-covariant phase along the junction. It follows the scaling of Eq. 3.10, and it is determined by a dimensionless function, which is plotted in (b). (c) Shows the interference pattern calculated integration of the result in (a) using Equation 3.8 for different values of B. The typical interference pattern looks like a Fraunhofer pattern at first sight. However, the peak height decreases less strongly than $1/B$, and the width of the side lobes is larger than half of the middle lobe, which is 10.76 mT wide. Furthermore, the width of the nth side lobe increases and reaches an asymptotic value for large values of n, which is evident from the inset of (c), where we plot the width of the nth side lobe. The width of the fifth side lobe is used for comparisons between simulations and experiments.

value $\Delta BW^2/\Phi_0$ as a function of the aspect ratio L/W in Figure 3.3a on a log-log scale. First, we find the results obtained on the rectangular junction to match the analytical results obtained by Clem[7]. Furthermore, the periodicity of the pattern increases as the sample dimensions are diminished. In a laterally smaller sample, the screening currents are more confined to the junction, and therefore the effective length L_{eff} is smaller, yielding a larger ΔB. Finally, we evaluated the width of the junction (d) to be irrelevant in determining ΔB. Specifically, its contribution to the period is in the µT range for realistic sizes of d. The consequence is that ΔB is determined by the maximum of γ, i.e., $\gamma(\frac{d}{2}, \frac{W}{2})$.

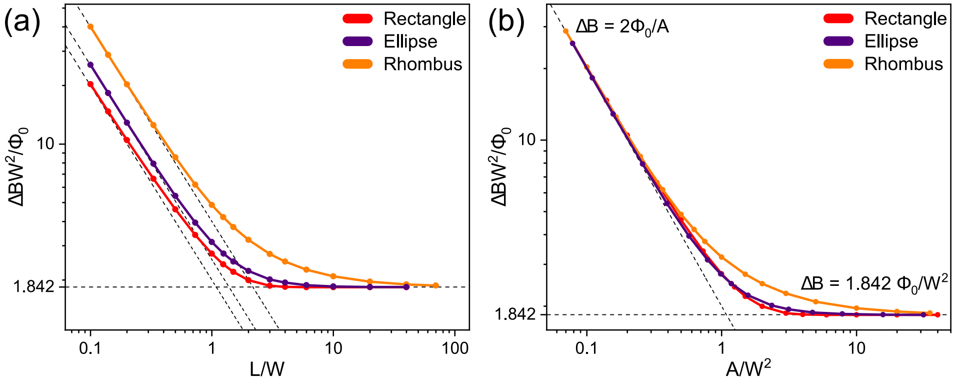

Figure 3.3: dimensionless measure of the period ΔB (the width of the fifth side lobe) of the calculated interference pattern $I_c(B)$ for the three geometries. In (a) we plot this value on log-log scale versus the aspect ratio L/W, in (b) it is plotted versus the total electrode area A, scaled by the width of the film squared. Figure (b) reveals two limits for ΔB for $L \gg W$ and $L \ll W$. The first corresponds to the limit of an infinite superconducting strip $\Delta B = 1.842\Phi_0/W^2$, whereas in the latter we find $\Delta B = 2\Phi_0/A$. Contrary to ΔB, $I_c(B)$ itself is not geometry independent in this limit.

ΔB reaches asymptotic values for the limits $L \gg W$ and $L \ll W$ for all three geometries. The value of ΔB becomes geometry independent in these limits, as revealed by rescaling the results from Figure 3.3a to a $\frac{A}{W^2}$ dependence, displayed in Figure 3.3b. In the first limit, $L \gg W$, all three geometries become an infinite superconducting strip. Here we find $\Delta B = 1.842\Phi_0/W^2$, which matches literature[6, 7]. In this limit, we find $\gamma\left(\frac{d}{2}, y\right)$ to follow:

$$\gamma\left(\frac{d}{2}, y\right) = \frac{7\,\zeta(3)}{\pi^2}\frac{BW^2}{\Phi_0} f_{\text{strip}}\left(\frac{y}{W}\right) = \frac{\pi}{2}\frac{1}{1.842}\frac{BW^2}{\Phi_0} f_{\text{strip}}\left(\frac{y}{W}\right) \tag{3.11}$$

Where $f_{\text{strip}}\left(\frac{y}{W}\right)$ is a dimensionless function running from -1 to 1, plotted in Figure 3.4a. In the other limit, $L \ll W$, Eq. 3.10 reduces to:

$$\gamma\left(\frac{d}{2}, y\right) = \frac{\pi AB}{4\Phi_0} f\left(\frac{y}{W}\right) = \frac{\pi}{2}\frac{AB}{2\Phi_0} f\left(\frac{y}{W}\right) \tag{3.12}$$

Figure 3.4b shows $f\left(\frac{y}{W}\right)$ in the limit $L \ll W$, for all three geometries. Since the maximum of $f\left(\frac{y}{W}\right)$ becomes independent of the underlying geometry and equal to unity, we find a geometry independent period, where $\Delta B = 2\Phi_0/A$. We can generalize this concept to find a general expression for ΔB:

$$\Delta B = \frac{\pi}{2}\frac{1}{\max(\gamma/B)} = \frac{\pi}{2}\frac{B}{\gamma(\frac{d}{2}, \frac{W}{2})} \tag{3.13}$$

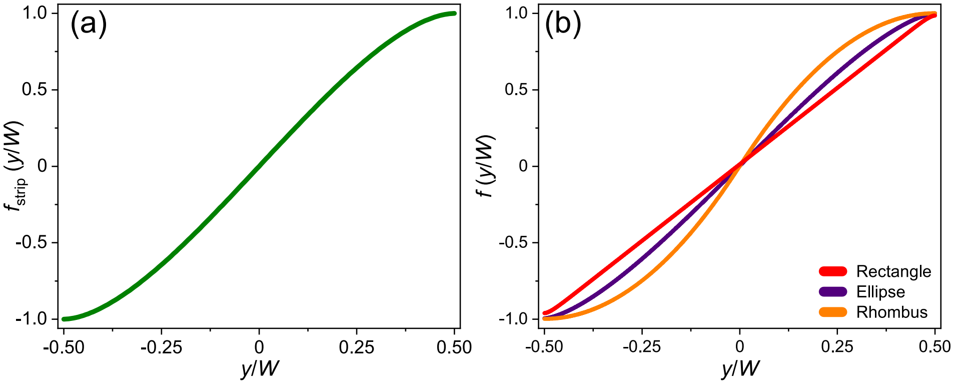

Figure 3.4: dimensionless scaling functions $f\left(\frac{y}{W}\right)$ from Eq. 3.10, for the limit $L \gg W$ in (a) and $L \ll W$ in (b). The maximum of these functions is located at $y = |W/2|$ and equals unity. Therefore, ΔB (large n limit of the nth side lobe of $I_c(B)$) is universal for these limits. However, for the limit $L \ll W$, $f\left(\frac{y}{W}\right)$ is not geometry independent, which means $I_c(B)$ itself is not geometry independent in this limit.

Note that $\max(f(\frac{y}{W})) \approx 1$ for all ratios L/W, and thus Eq. 3.13 can serve as a good approximation for ΔB. Therefore, we justify the relation of Eq. 3.10 as it demonstrates the emerging universal limits where $\Delta B = 2\Phi_0/A$ and $\Delta B = 1.842\Phi_0/W^2$, as well as provides a good approximation of ΔB between the limiting cases.

Although ΔB is geometry independent in the limit $L \ll W$, $I_c(B)$ itself is not universal in this limit. This is caused by the fact that $f\left(\frac{y}{W}\right)$ differs between geometries for $y \neq |W/2|$. For the rectangular geometry, for example, this function is linear in y: $f\left(\frac{y}{W}\right) = \frac{2y}{W}$. Therefore, we retrieve the Fraunhofer pattern, where $L_{\text{eff}} = L/2 + d$. The effective length equals the length of a single superconducting electrode plus the junction length. This can be understood by considering that the screening currents trace loops in the electrodes, that reduce to two parallel and opposite current tracks, when $L \ll W$. The tracks that contribute to $J_y(\frac{d}{2}, y)$ effectively cover half of each electrode, yielding $L_{\text{eff}} = L/4 + L/4 + d$. $\gamma\left(\frac{d}{2}, y\right)$ in the rhomboid geometry is radically different; it is well approximated by a sine function: $f\left(\frac{y}{W}\right) = \sin\left(\frac{\pi y}{W}\right)$. This leads to an interference pattern that is far closer to the pattern shown in Figure 3.2c, and not a Fraunhofer pattern. In conclusion: the shape and periodicity of the $I_c(B)$-pattern for low magnetic fields is independent of ΔB_n in the limit of large n, which is universal for $L \ll W$.

3.3.2. COMPARISON TO EXPERIMENTS

In order to verify the dependence on the geometry, we have fabricated five ellipse-shaped planar S−N−S junctions for different ratios of L/W. Besides, we made a rectangular-shaped junction with dimensions well in the $L \gg W$ limit.

First, a four-probe contact geometry is patterned on Si substrates using electron-beam lithography. Next, an Ag (20 nm), MoGe (55 nm) bilayer is deposited by sputter deposition. Next, we use Focused Ion beam (FIB) milling to structure elliptical devices in the bilayer. By applying an ultra-low beam current of 1.5 pA, the weak link is formed by a line cut in the MoGe layer at the center of the device. This completely removes the superconductor on top but leaves a normal metal connection. The resulting trench

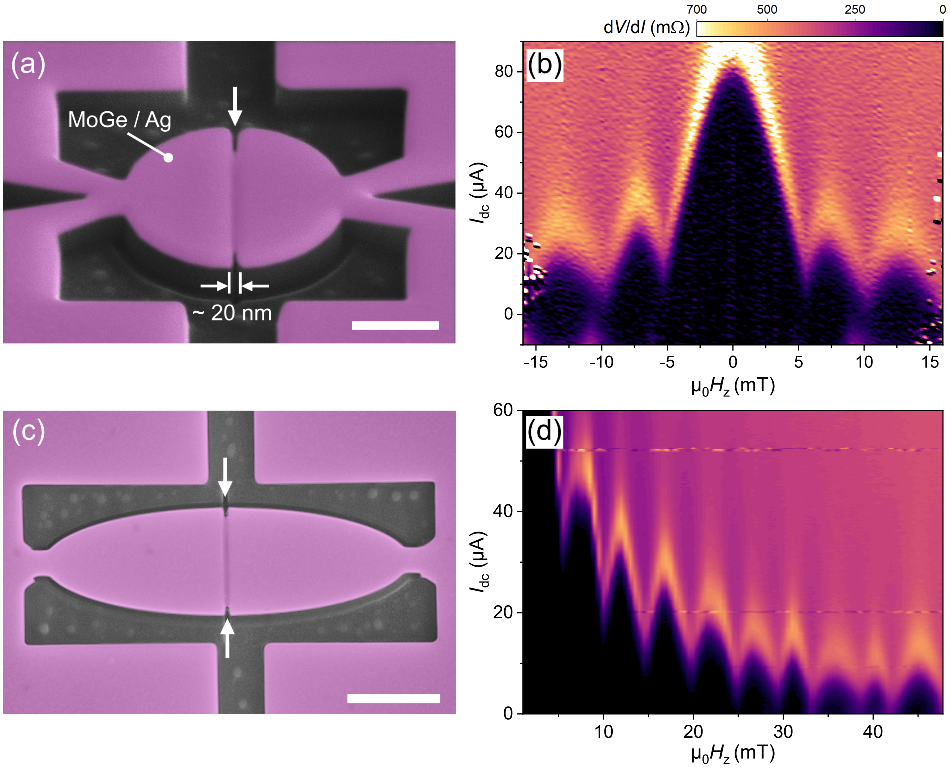

Figure 3.5: Two S−N−S junction samples with a circular and ellipsoid geometry, produced from an Ag/MoGe bilayer and their corresponding $I_c(B)$-patterns. (a) A false colored scanning electron micrograph of a disk-shaped sample, viewed under an angle. The white arrow indicates the junction. Note the notches on the side of the sample due to an increased milling rate at the edges of the disk. The scale bar equals 500 nm. The corresponding $I_c(B)$, displayed in (b), is a Fraunhofer-like pattern. As expected, the peak height of the side lobes is decreasing less rapidly than $1/B$. Contrary to the calculated pattern in Figure 3.2c, the middle peak is twice as wide as the neighboring ones. (c) depicts a top-view false colored scanning electron micrograph of an ellipse-shaped junction. Again we indicate the notches with white arrows; the scale bar represents 1 μm. In (d), we plot the corresponding interference pattern, which is used to extract the periodicity of the oscillations.

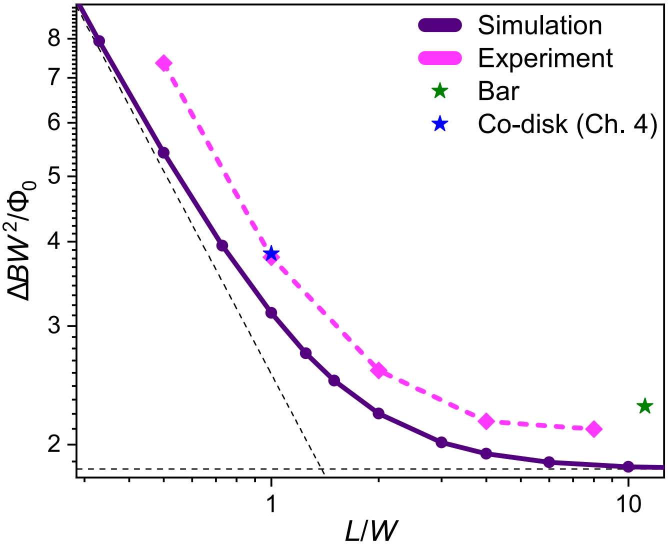

Figure 3.6: Calculated periodicity ΔB of the fifth lobe of the interference pattern $I_c(B)$ obtained for the ellipse-shaped samples, compared to experimentally acquired values. We plot the dimensionless measure $\frac{\Delta BW^2}{\Phi_0}$ versus the aspect ratio L/W. The blue star indicates the periodicity of the cobalt disk junctions discussed in Chapter 4 and the green star represents the results obtained on a bar shaped sample. Although we can well predicted the L/W-dependence, we find a constant offset between the experimental values and the simulations. This can be explained by the notches visible in Figure 3.5a and 3.5c, which make the junction width shorter than the width of the electrodes (W).

separates the MoGe electrodes by a roughly 20 nm weak link, allowing Josephson coupling in this S−N−S system. Figures 3.5a and 3.5c show false colored scanning electron micrographs of two of such devices, for $L = W$ and $L = 4W$ respectively. We follow the same fabrication procedure for the S−F−S devices presented in Chapters 4 and 5.

Two corresponding interference patterns obtained on the samples in 3.5a and 3.5c are shown in Figure 3.5b and 3.5d. Clearly, the period of the interference patterns scales with L/W. However, we find that the middle peak is twice the width of the neighboring ones and the amplitude of the side lobes of the $I_c(B)$-pattern feature a similar width, instead of the asymptotic behavior predicted by our theory (see Figure 3.2c). This can be explained by the fact that $l \approx 100$ nm (Eq. 3.2; based on $\lambda = 535$ nm[9]), which is small with respect to W. Our samples are therefore not in the narrow junction limit and allow Josephson vortices to stabilize in the junction. The width of the middle lobe can therefore not be predicted by our theory. However, Boris et al. have shown that ΔB_n for large n still follows the predictions of non-local electrodynamics[4]. Therefore, we can still compare the measured ΔB to our theoretical model.

To compare the period of the $I_c(B)$-pattern to our theory, we extract the width of the fifth lobe of the interference pattern for all measured samples and plot it along with the calculated values in Figure 3.6a. By star symbols, we also mark the periodicity of the oscillations of the Co-based S–F–S junctions discussed in Chapter 4 and the periodicity of the bar-shaped sample. Although there is a constant offset between the measured periodicity and the calculated values, the overall trend is well predicted.

This constant offset can be explained by a trivial side effect of the FIB structuring method. During FIB processing, removed material is redeposited elsewhere on the sample. Even though redeposition does not affect the devices, it leads to a dependence of the milling rate on the geometry. A more exposed part of the sample, i.e., the edges of the device, will mill faster than in the bulk of the material. Consequently, notches develop on the side of the device when milling the trench. These notches make the width of the weak link slightly smaller than the width of the electrodes, which can result in a constant offset between the simulations and experiments. A method of accounting for the influence of the notches is modifying the Fourier transform for application to thin film planar junctions, which I will discuss below.

However, there is also an inconsistency between our experimental data and the theory. We cannot explain why the rectangular-shaped junction exhibits an $\Delta B W^2/\Phi_0$ that is larger than our ellipses with high L/W-ratios. In fact, in the limit of $L \gg W$, we expect a universal limit that is independent of the size of the notches (see for example references [10] and [11]). At the moment this is unexplained.

3.4. CONSEQUENCES FOR THE FOURIER ANALYSIS

In Chapter 2 it became clear that $I_\mathrm{c}(B)$ is related to the critical current distribution in the junction, by Fourier transform. For macroscopic junctions, where the screening currents are Meissner-like, we have evaluated $\varphi_B(y) = \frac{2\pi L_\mathrm{eff} B}{\Phi_0} y$. For the mesoscopic devices discussed here, this quantity needs to be replaced by Eq. 3.7, yielding:

$$I_\mathrm{c}(B) = \left| \int_{-\infty}^{\infty} J_\mathrm{c}(y) e^{i2\gamma\left(\frac{d}{2},y\right)} \,\mathrm{d}y \right| = \left| \int_{-\infty}^{\infty} J_\mathrm{c}(y) e^{i2\pi\left(\frac{7\,\zeta(3)}{\pi^3}\frac{BW^2}{\Phi_0}\tanh\left(\frac{\pi^4}{112\,\zeta(3)}\right) f_\mathrm{disk}\left(\frac{y}{W}\right)\right)} \,\mathrm{d}y \right| \quad (3.14)$$

Where we omitted the contribution from the weak link, as its magnitude is negligible. In the second part we specified $\gamma\left(\frac{d}{2}, y\right)$ for a disk-shaped junction. Now we can define a new pair of conjugate variables: the length $\tilde{y} = W f_\mathrm{disk}\left(\frac{y}{W}\right)$ and the reduced field $\tilde{\beta} = \frac{7\,\zeta(3)}{\pi^3}\frac{BW}{\Phi_0}\tanh\left(\frac{\pi^4}{112\,\zeta(3)}\right)$, to arrive at:

$$I_\mathrm{c}(\tilde{\beta}) = \left| \int_{-\infty}^{\infty} \tilde{J}_\mathrm{c}(\tilde{y}) e^{i2\pi\tilde{\beta}\tilde{y}} \,\mathrm{d}\tilde{y} \right| = |\mathfrak{I}_\mathrm{c}| \quad (3.15)$$

Where we made a change of coordinates and $\tilde{J}_\mathrm{c}$ is defined as:

$$\tilde{J}_\mathrm{c}\left(\frac{\tilde{y}}{W}\right) = \frac{\mathrm{d}g}{\mathrm{d}\tilde{y}}\left(\frac{\tilde{y}}{W}\right) J_\mathrm{c}\left(Wg\left(\frac{\tilde{y}}{W}\right)\right) \tag{3.16}$$

Here the function $g\left(\frac{\tilde{y}}{W}\right)$ is the inverse of $f\left(\frac{y}{W}\right)$, or $g\left(\frac{\tilde{y}}{W}\right) = f^{-1}\left(\frac{y}{W}\right)$, dropping the subscript, as a similar procedure can be done for the general scaling relation of Eq. 3.10. We conclude that the Fourier transform is still valid, albeit including a rescaling of the axes to retrieve the actual current density distribution $J_\mathrm{c}(y)$. In the next section I will detail how the Fourier analysis is carried out technically for a disk-shaped junction.

3.4.1. TECHNICAL DETAILS OF THE FOURIER ANALYSIS

The transform $\mathfrak{I}_\mathrm{c}$ is complex and therefore its real and imaginary parts encode for the even and odd components in $I_c(\beta)$ respectively. Since the interference patterns discussed in this thesis are relatively symmetric (i.e., an even function of the applied magnetic field), we can assume $\mathfrak{I}_\mathrm{c}$ to be dominantly real:

$$I_\mathrm{c,even}(\tilde{\beta}) = \int_{-\infty}^{\infty} \tilde{J}_\mathrm{c,even}(\tilde{y}) \cos\left(\tilde{\beta}\tilde{y}\right) \mathrm{d}\tilde{y} \tag{3.17}$$

Therefore the real part of $\mathfrak{I}_\mathrm{c}$ is an oscillating function that flips sign at each zero crossing. The imaginary part is expected to be significantly smaller than the real part, except at the zero-crossing where the even part vanishes. Therefore, the imaginary part of $\mathfrak{I}_\mathrm{c}$ ($I_\mathrm{c,odd}(\tilde{\beta})$) can be approximated by the critical current at the minima in the experimental interference pattern. Also $I_\mathrm{c,odd}(\tilde{\beta})$ is flipping its sign between each minimum and between the minima we approximate $I_\mathrm{c,odd}(\tilde{\beta})$ by linear interpolation. The inverse transform yielding $\tilde{J}_\mathrm{c}(\tilde{y})$ from $I_\mathrm{c}(\tilde{\beta})$ is then given by:

$$\tilde{J}_\mathrm{c}(\tilde{y}) = \left|\int_{-\infty}^{\infty} \left(I_\mathrm{c,even}(\tilde{\beta}) + i\, I_\mathrm{c,odd}(\tilde{\beta})\right) e^{-i\tilde{\beta}\tilde{y}}\, \mathrm{d}\tilde{\beta}\right| = \left|\int_{-\infty}^{\infty} \mathfrak{I}_\mathrm{c}\, e^{-i\tilde{\beta}\tilde{y}}\, \mathrm{d}\tilde{\beta}\right| \tag{3.18}$$

As discussed in the previous chapter, we find I_c from the data by a defining a voltage threshold; this is depicted in Figure 3.7a for a disk-shaped junction. We vertically translate the extracted I_c values such that the global minimum equals zero current. This step in the data analysis prevents the overestimation of $I_\mathrm{c,odd}(\tilde{\beta})$, which would result in an overly anti-symmetric current density distribution. $I_\mathrm{c,even}(\tilde{\beta})$ is found by multiplying the translated I_c by a flipping function that changes the sign of each subsequent lobe of the interference pattern, as can be observed in Figure 3.7b.

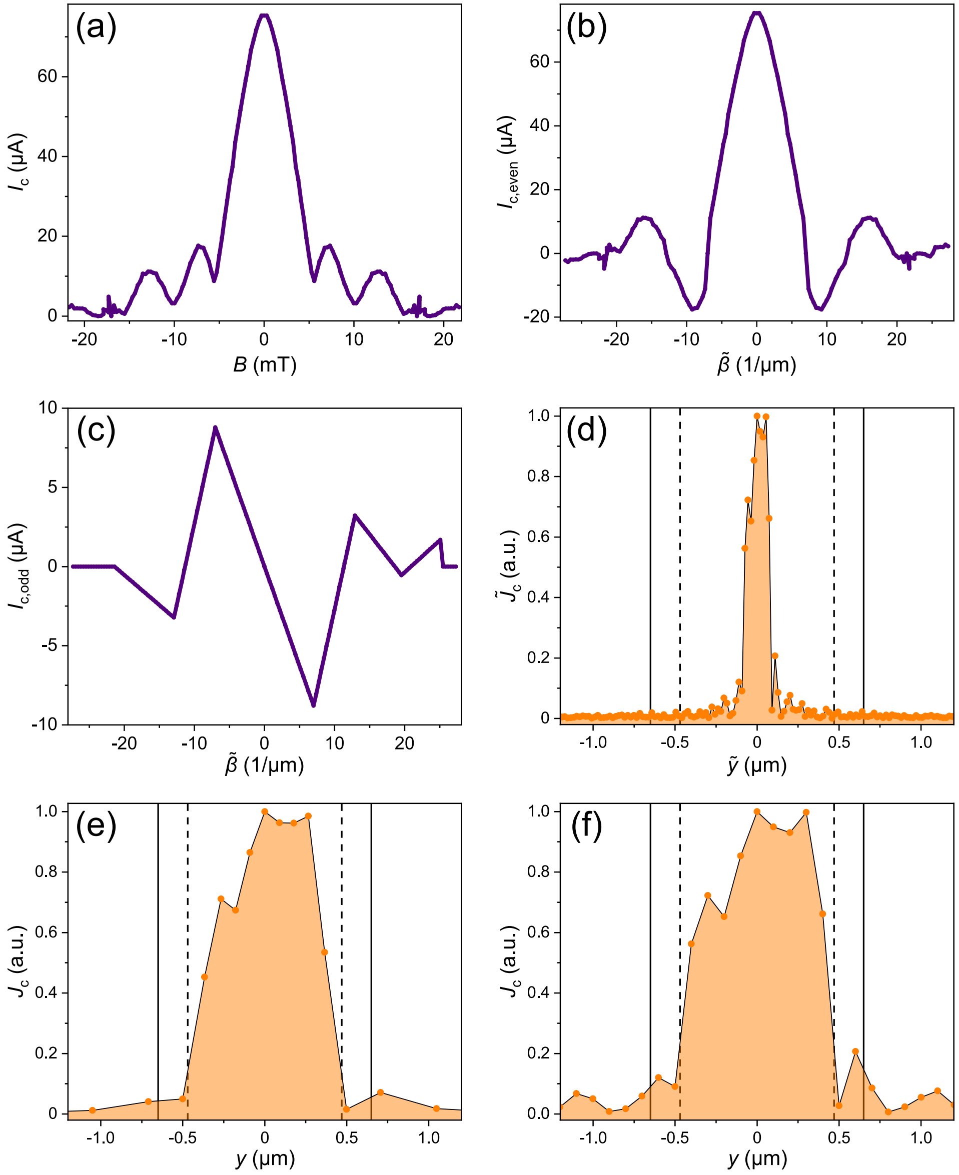

Figure 3.7: Overview of the subsequent steps of the Fourier transform analysis. (a) Extracted critical current on the basis of a voltage cut-off. In order to not overestimate the imaginary part of the complex critical current, the global minimum of the interference pattern is shifted to zero current. (b) and (c) respectively show the real and imaginary part of the complex critical current extracted from the interference pattern depicted in (a). Here the subsequent lobes are flipped to obtain the real part, and the minima are interpolated to obtain the imaginary part. (d) The resulting critical current density distribution, calculated using the Fourier transform described in Eq. 3.18. The result of (d) is scaled using $f_{\mathrm{disk}}\left(\frac{y}{W}\right)$, to retrieve the actual $J_c(y)$, which is plotted in (e). Finally, in (f), we carried out a regular Fourier analysis using a linear approximation of $f_{\mathrm{disk}}\left(\frac{y}{W}\right)$, circumventing the need for rescaling the axes. In (d), (e), and (f), we indicate the boundaries of the electrodes ($-W/2$ and $W/2$) by solid reference lines and the boundaries of the actual weak link (W minus the notches) by dotted reference lines. We find a uniform current density distribution, as expected for a single junction. The influence of the notches can be seen since no current flows outside the actual width of the weak link.

Here we also rescale the field axis to $\tilde{\beta}$. We follow the above procedure for finding $I_{\mathrm{c,odd}}(\tilde{\beta})$, which is depicted in Figure 3.7c. The corresponding critical current density distribution is found by a numerical Fourier transform carried out in Python using the Numpy package, yielding the distribution $\tilde{J}_{\mathrm{c}}(\tilde{y})$, depicted in Figure 3.7d. Finally both axes are rescaled using $f_{\mathrm{disk}}\left(\frac{y}{W}\right)$ to retrieve $J_{\mathrm{c}}(y)$, which is shown in Figure 3.7e.[1] Here we indicate $-W/2$ and $W/2$ by solid reference lines and the boundaries of the actual weak link by dotted reference lines. We observe a constant distribution of critical current throughout the junction, which is expected for a uniform S−N−S junction. Furthermore, the current is confined to the actual junction, not the full width of the superconducting film. This explains the constant offset in Figure 3.6a.

Note that the spatial resolution of current density distribution is determined by the field range in the measured $I_{\mathrm{c}}(B)$-pattern, which is limited by the possible discontinuities, typically found in junctions with a ferromagnetic weak link. This sets a bound to the precision in determining the width of possible current channels. Furthermore, due to rescaling $\tilde{J}_{\mathrm{c}}(\tilde{y})$ to $J_{\mathrm{c}}(y)$, the binning becomes non-uniform, yielding a lower resolution near the edges of the device. As alternative, we carry out the Fourier transform using a linear approximation of $f_{\mathrm{disk}}\left(\frac{y}{W}\right)$, depicted in Figure 3.7f. This mitigates the need for rescaling the axes and improves point density on the position-axis. Obviously, the linear approximation of $f_{\mathrm{disk}}\left(\frac{y}{W}\right)$ breaks down near the edges, yielding less precise results.

3.5. CONCLUSION

In conclusion, this chapter analyzed the periodicity ΔB of the interference pattern $I_{\mathrm{c}}(B)$ for thin film planar S−N−S Josephson junctions, both theoretically and experimentally. Specifically, we examine junctions separating rectangular, ellipsoid, and rhomboid films of width W and length L. By mapping the second Ginzburg-Landau equation to the two-dimensional Laplace equation, we solve $I_{\mathrm{c}}(B)$ for different ratios of L/W. We show that ΔB has two universal limits for $L \gg W$ and $L \ll W$, independent of the sample geometry. The first corresponds to an infinite superconducting strip, and the latter is caused by an emerging universal dependence of the phase difference on the junction electrode surface area. By fabricating elliptically-shaped S−N−S junctions, having different ratios for L/W, we experimentally verify the geometry dependence of ΔB. Lastly, we adapt the Fourier relation between $I_{\mathrm{c}}(B)$ and the critical current density distribution to suit planar junctions in the thin film limit. This proves to be vital in correctly predicting the location of current channels in the disk- and elliptically-shaped S−F−S junctions discussed in the next part of this thesis.

---

[1] For illustrative purposes, I have chosen to absorb part of the prefactor in $\tilde{y}$, as this this yields a larger contrast between Figure 3.7d and Figure 3.7e. Naturally, any choice of $\tilde{y}$ and $\tilde{\beta}$ is allowed, as long as it is consistent with γ.

REFERENCES

[1] Pearl, J. Current distribution in superconducting films carrying quantized fluxoids. *Appl. Phys. Lett.* **5**, 65–66 (1964).

[2] Ivanchenko, Y. & Soboleva, T. Nonlocal interaction in Josephson junctions. *Phys. Lett. A* **147**, 65–69 (1990).

[3] Abdumalikov, A. A., Jr., Alfimov, G. L. & Malishevskii, A. S. Nonlocal electrodynamics of Josephson vortices in superconducting circuits. *Supercond. Sci. Technol.* **22**, 023001 (2009).

[4] Boris, A. A. *et al.* Evidence for nonlocal electrodynamics in planar Josephson junctions. *Phys. Rev. Lett.* **111**, 117002 (2013).

[5] Kogan, V. G., Dobrovitski, V. V., Clem, J. R., Mawatari, Y. & Mints, R. G. Josephson junction in a thin film. *Phys. Rev. B* **63**, 144501 (2001).

[6] Moshe, M., Kogan, V. G. & Mints, R. G. Edge-type Josephson junctions in narrow thin-film strips. *Phys. Rev. B* **78**, 020510(R) (2008).

[7] Clem, J. R. Josephson junctions in thin and narrow rectangular superconducting strips. *Phys. Rev. B* **81**, 144515 (2010).

[8] Rodan-Legrain, D. *et al.* Highly tunable junctions and non-local Josephson effect in magic-angle graphene tunnelling devices. *Nat. Nanotechnol.* **16**, 769–775 (2021).

[9] Mandal, S. *et al.* Destruction of superconductivity through phase fluctuations in ultrathin a-moge films. *Phys. Rev. B* **102**, 060501 (2020).

[10] Golod, T., Kapran, O. & Krasnov, V. Planar superconductor-ferromagnet-superconductor Josephson junctions as scanning-probe sensors. *Phys. Rev. Applied* **11**, 014062 (2019).

[11] Hovhannisyan, R. A., Golod, T. & Krasnov, V. M. Holographic reconstruction of magnetic field distribution in a Josephson junction from diffraction-like $I_c(H)$ patterns. *Phys. Rev. B* **105**, 214513 (2022).

Mesoscopic S–F-hybrid Josephson junctions

2

4

SUPERCONDUCTING TRIPLET RIM CURRENTS IN A SPIN-TEXTURED FERROMAGNETIC DISK

R. Fermin, D. van Dinter, M. Hubert, B. Woltjes, M. Silaev, J. Aarts & K. Lahabi

Since the discovery of the long-range superconducting proximity effect, the interaction between spin-triplet Cooper pairs and magnetic structures such as domain walls and vortices has been the subject of intense theoretical discussions, while the relevant experiments remain scarce. Using the procedure from Chapter 3, we fabricate disk-shaped Josephson junctions with a ferromagnetic cobalt barrier, which features a highly controllable spin texture. Here, the vortex magnetization of Co and the Cooper pairs of Nb conspire to induce long-range triplet (LRT) superconductivity in the ferromagnet. Surprisingly, the LRT correlations emerge in highly localized (sub-80 nm) channels at the rim of the ferromagnet, despite its trivial band structure. We show that these robust rim currents arise from the magnetization texture acting as an effective spin-orbit coupling, which results in spin accumulation at the bilayer–vacuum boundary. Lastly, we demonstrate that both 0 *and* π *channels can be realized in the same device by altering the spin texture of the ferromagnet.*

This chapter is based on the paper published in *Nano Letters* **22**, 2209-2216 (2022).

4.1. INTRODUCTION

The appearance of localized supercurrents at the edges of a Josephson junction is generally attributed to the topology of the electronic band structure and edge states[1]. Edge states and the accompanying edge currents are typically found in ultraclean systems such as 2D electron gases[2], nanowires[3], and graphene[4]. Here, we report the emergence of highly localized (sub-80 nm) spin-polarized supercurrents at the rim of disk-shaped Josephson junctions with a diffusive ferromagnetic barrier (Co). As we demonstrate, however, the rim currents are not related to the electronic band structure but rather a direct result of the interactions between spin-triplet Cooper pairs and the non-trivial spin texture of the ferromagnet.

At the interface between a superconductor and a ferromagnet, short-range triplet (SRT; in Dirac notation $\frac{1}{\sqrt{2}}(|\uparrow\downarrow\rangle + |\downarrow\uparrow\rangle)$, i.e., triplets without spin projection along the quantization axis) Cooper pairs with zero spin projection emerge naturally via spin-mixing of singlet pairs and decay over a few nanometers (ξ_{F}(Co) ~ 3 nm [5]) inside the ferromagnet. Long-range triplet (LRT, in Dirac notation $|\uparrow\uparrow\rangle$ and $|\downarrow\downarrow\rangle$) pairs can, on the other hand, propagate over substantially larger distances[6, 7]. Half-metallic systems can even show the LRT proximity effect over hundreds of nanometers[8–11]. Due to their spin polarization, the LRT Cooper pairs can provide the means to combine the absence of Joule heating and decoherence with the functionality of spintronic devices[12, 13]. However, the controlled generation of LRT currents has proven to be a demanding process, commonly realized in complex superconductor-ferromagnet hybrids, involving multiple F layers with noncollinear magnetization[14–24]. Furthermore, a substantial body of research considered the possibility of generating and controlling LRT correlations using spin-textured systems, such as domain walls[6, 25–28] and vortices[29, 30]. However, the experimental evidence to verify such models remains scarce[31]. In other recent developments, it was suggested that theoretically, spin mixing can also be achieved by spin-orbit coupling (SOC)[32–36]. This led to researching long-range proximity effects with Josephson junctions containing heavy metal interlayers[37–43]. In addition, recent studies suggest that spin-orbit coupling (SOC) can lead to spin accumulation at the edges of Josephson devices[35, 44, 45] and, in some cases, generation of LRT currents[46–49]. At present there is a complete lack of experiments that can examine the influence of SOC on LRT transport. As a consequence, the interplay between triplet pairing and magnetic texture as well as SOC remains elusive.

To address these issues, we use the control of the junction geometry gained in Chapter 3 to fabricate disk-shaped S−F−S Josephson junctions that feature a ferromagnetic vortex spin texture capable of converting singlet Cooper pairs into LRT currents. These exhibit a (~ 20 nm) cobalt weak link, which eliminates any singlet or SRT transport. We show that a magnetization gradient of the vortex can act as an effective SOC, which leads to spin accumulation at the rims of the device. This is verified by our transport experiments, which show that the LRT transport is highly localized at the rims of the

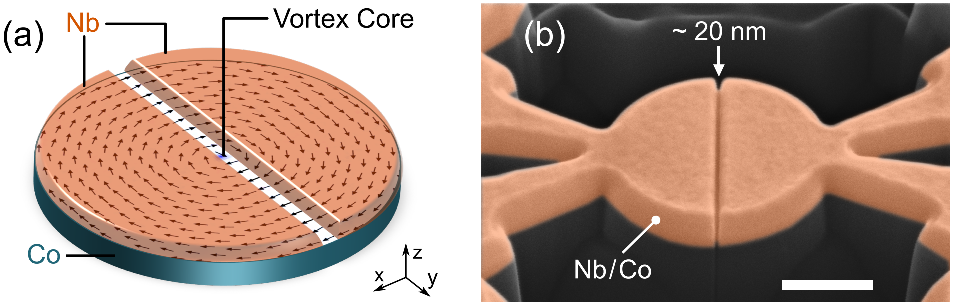

Figure 4.1: (a) Schematic of the Josephson device. The Nb electrodes are separated by a trench, forming a Co weak link. The pattern on the Co layer corresponds to micromagnetic simulations of a micrometer-size disk. (for more information on the micromagnetic simulations, see Appendix A of Chapter 5). The arrows correspond to the in-plane magnetization, while the out-of-plane component is represented by color, which only appears at the vortex core (blue region; less than 5 nm in diameter). Schematic courtesy of Kaveh Lahabi. (b) False colored scanning electron micrograph of a structured bilayer. The 20 nm gap indicates the Co weak link at the bottom of the trench. The scale bar is equivalent to 400 nm.

ferromagnet, resulting in a distinct double-slit supercurrent interference pattern. By modifying the spin texture in a controllable manner, we show that both 0 and π segments can emerge in a single junction. Utilizing the linearized Usadel equation, we examine the microscopic origin of the rim currents in the proximized ferromagnet. Our findings suggest that, in addition to spin texture, superconductor-vacuum boundary conditions play an essential role in the singlet to LRT conversion.

4.2. ESTABLISHING LONG-RANGE TRIPLET TRANSPORT

Using equal methods as introduced in Chapter 3, we fabricate S−F−S disk junctions from an Nb/Co bilayer (thickness of 45 nm and 60 nm, respectively). Generally, in a disk-shaped ferromagnet of these size ranges, the magnetic moments will align in a vortex magnetization pattern[50, 51]. Therefore, we obtain a weak link containing a ferromagnetic vortex coupled by two superconducting leads. A schematic representation of such a junction is shown in Figure 4.1a, along with a false colored scanning electron micrograph of an actual device in Figure 4.1b. Figure 4.2a shows resistance as a function of temperature for a typical disk junction. A micron-wide weak link has a resistance of 200 mΩ and becomes fully proximized at low temperatures. We unambiguously establish the Josephson transport in our device by observing their Shapiro response to microwave radiation. The IV-curves show clear Shapiro steps (discrete voltage steps of $hf/2e$, where h is the Planck constant, f is the frequency, and e is the electron charge), which is a result of the phase-locking between the applied microwaves and the Josephson currents (see Figure 4.2(b)).

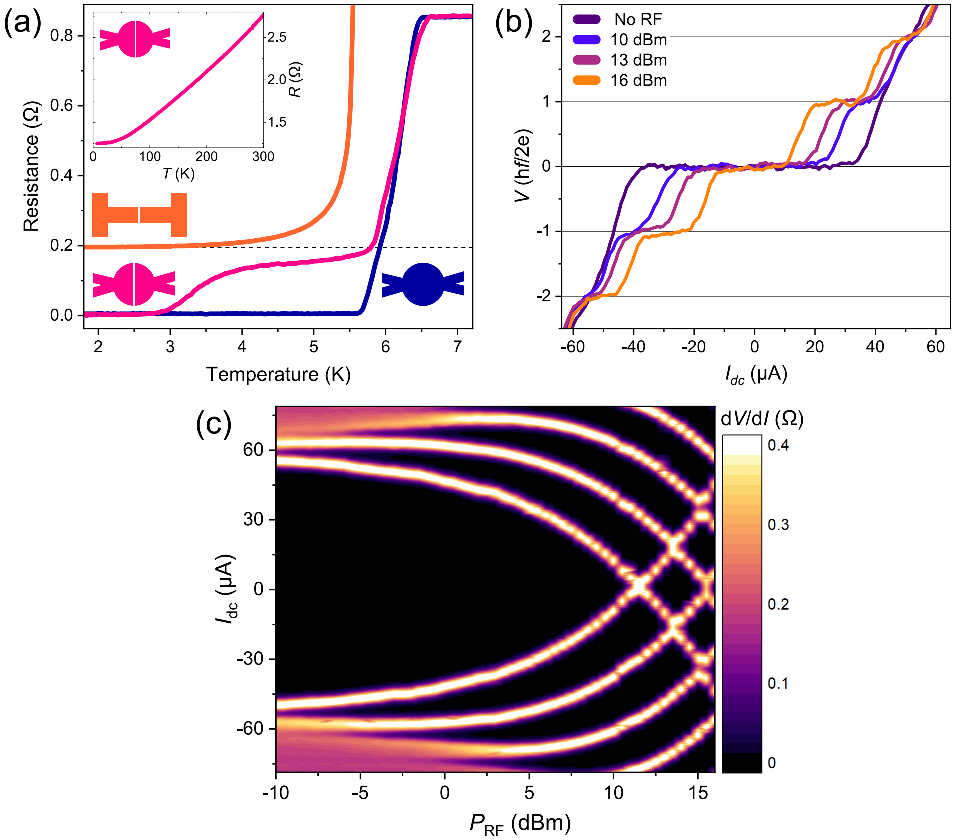

Figure 4.2: Overview of the basic transport properties of the devices. (a) Resistance as a function of temperature of a proximized disk device (pink) is compared to a Co−Nb disk without a trench (blue) and a bar-shaped device with uniform magnetization (orange). The bar-shaped device is not proximized due to the lack of spin texture (for more information, see Appendix A). (b) IV-characteristics at 2 K of a proximized disk device, measured while irradiating the sample with $f = 1.1$ GHz of microwave radiation for different powers. The voltage is normalized in units of $hf/2e$. (c) Evolution of the Shapiro response as a function of RF power represented as $\mathrm{d}V/\mathrm{d}I(\Omega)$ color map.

A direct method to examine the presence of LRT correlations is to verify that the proximity effect will disappear once the mechanism for the emergence of LRT pairing is eliminated. For instance, in the case of S/F′/F/F′/S multilayer junctions used in previous studies, where the generation of LRT correlations requires a magnetic non-collinearity between the F and F′ layers, the control experiment would show that I_c is heavily suppressed if the F′ layers were either removed or magnetized parallel (or antiparallel) to the F layer[15, 16, 18, 20, 23, 52]. The same argument applies here: if the proximity effect is due to LRT correlations produced by the spin texture of the junction, the I_c must vanish once the magnetization is uniform. We verify this through two experiments described in Appendix A. First, we examined the transport in bar-shaped control samples, where shape anisotropy ensures that (even in the absence of in-plane fields) the cobalt layer has a uniform magnetization along the long axis of the bar (see

Figure 4.2a and Figure A.1). These samples were fabricated via the same procedure as the primary disk-shaped junctions and received the same FIB treatment to structure their weak link. This is evident by the fact that the bar-shaped junctions and the disk devices have a matching barrier resistance ($\approx$ 200 mΩ). Despite multiple attempts, however, the bar-shaped control samples show no sign of long-range proximity. We also prepared disk-shaped control junctions where, by applying a lower dose of Ga-ions when structuring the weak link, we leave some residual Nb at the bottom of the trench, forming a nonmagnetic channel for singlet transport. Such junctions are completely insensitive to the magnetic state of the cobalt disk and are robust against the in-plane fields used for altering the spin texture; they maintain their I_c at fields as high as 2 T (see Figure A.3b). In contrast, for the triplet devices, this happens when we remove the spin texture by applying an in-plane field of 180 mT, which completely suppresses the I_c (see Figure A.3a).

4.3. TRIPLET CURRENTS CONFINED TO THE RIMS OF THE DISK

We establish the presence of rim currents by obtaining $I_c(B)$ of our junctions. Note that the out-of-plane fields used in these experiments are too small to disturb the stable vortex magnetization of the Co disk.

In a conventional S–N–S junction, the supercurrent is distributed uniformly across the weak link, yielding the interference patterns presented in Chapter 3. As shown in Figure 4.3, our S–F–S devices show a completely different behavior: two-channel interference patterns characterized by equal-width lobes and slow decay of oscillation amplitude. All the triplet junctions we measured (over ten devices) show such a two-channel interference pattern. This is illustrated in Figure 4.3, where we show the $I_c(B)$-patterns for two junctions with different diameters (1.62 and 1.05 µm). Note that the period of the oscillations scales inversely with the area of the junction, which is determined by the radius of the disk. We apply inverse Fourier transform to the $I_c(B)$-patterns to reconstruct the spatial distribution of supercurrent density. Figure 4.3 shows the results of our Fourier analysis for both devices. Regardless of the sample area, we consistently find the supercurrent to be highly localized at the rim of the sample: the rim current channels are 70 nm or less in width, limited by the resolution of the Fourier analysis[1]. Furthermore, the channels are highly symmetric, as indicated by the sharp cusps of the $I_c(B)$-pattern. Note that the trench is deepest on the sides of the disk (due to the geometry dependence on the milling rate, as can be seen by the small notches on the sides of the disk in Figure 4.1b), making the formation of accidental singlet edge channels even

---

[1] Here we have used the linear approximation of $f\left(\frac{y}{W}\right)$ to improve resolution, see section 3.4.1. In the published version of this chapter, we carried out the analysis by establishing a scaling relation between the period of the oscillations and the diameter of the disk. Here I adapted the Fourier analysis to incorporate the results from Chapter 3.

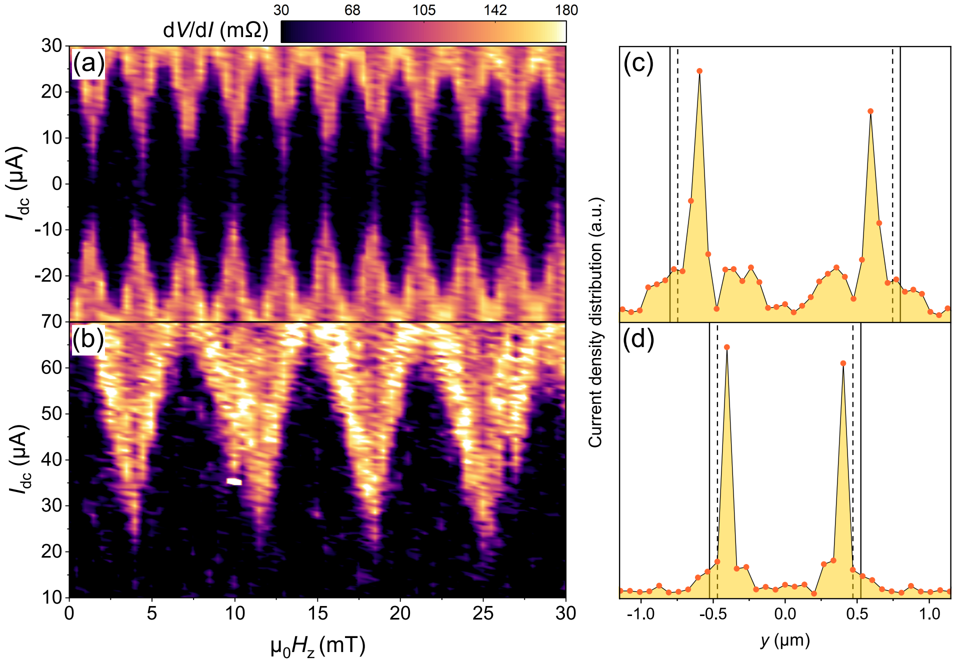

Figure 4.3: (a) and (b) Show superconducting interference patterns of two junctions with different diameters. The pattern is obtained by measuring the differential resistance as a function of d.c. current and magnetic field. The disk diameters in (a) and (b) are 1.62 μm and 1.05 μm, respectively. The period of the oscillations scales inversely with the junction area. In both cases, the junctions show a clear two-channel interference pattern. (c) and (d) depict the critical current density profiles obtained by the Fourier analysis of the patterns in (a) and (b) respectively. The vertical lines indicate the boundaries of the device.

less probable. More importantly, the two-channel behavior is completely absent in all the singlet control samples. If the barrier contains residual Nb, the junction yields a standard single-channel diffraction pattern (Figure A.2). Similarly, the current density in the S–N–S disk devices presented in Chapter 3 is distributed uniformly. This means the two-channel behavior is not a trivial result of the disk geometry.

4.4. ALTERING THE MAGNETIC TEXTURE BY AN IN-PLANE FIELD

So far, we have shown the unconventional distribution of supercurrents through the spin-textured ferromagnetic weak link. We investigate this further by modifying the spin texture using an in-plane magnetic field. Our micromagnetic simulations show that in-plane fields can alter the spin texture by effectively moving the vortex core along the axis perpendicular to the field (see Figure 4.4). For small in-plane fields, the core displacement has an almost linear response and is fully reversible. Using a vector magnet system, we can apply a constant in-plane magnetic field while simultaneously acquiring the $I_c(B)$-pattern as described above. Figure 4.4 shows the $I_c(B)$-patterns mea-

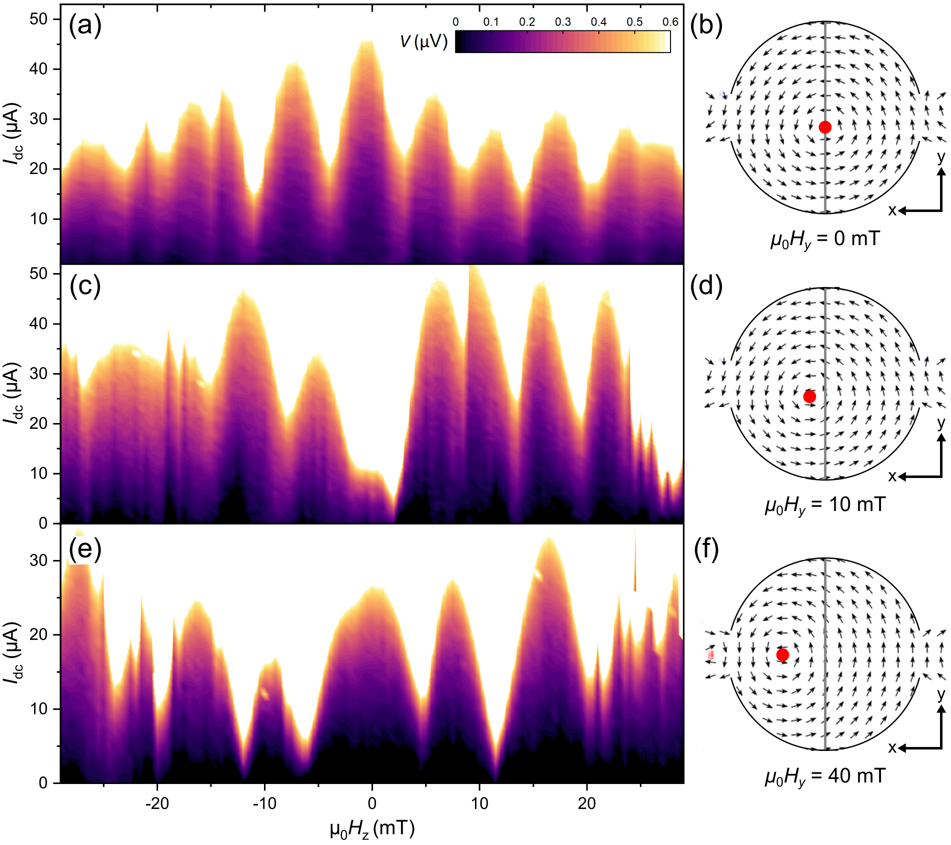

Figure 4.4: Supercurrent interference patterns (left column) measured at different in-plane fields and the corresponding simulated spin textures (right column). The gray line represents the position of the weak link, and the red dot indicates the location of the vortex core. (a) and (b) At zero in-plane field, the vortex is at the center of the disk, and a SQUID pattern is observed, i.e., lobes of equal width and slow decay of peak height. (c) and (d) Applying $\mu_0 H_\mathrm{y}$ = 10 mT breaks the axial symmetry of the vortex magnetization. This results in the suppression of the middle peak in the interference pattern, characteristic of a $0-\pi$ SQUID. (e) and (f) At $\mu_0 H_\mathrm{y}$ = 40 mT the vortex core is displaced by over 100 nm. The middle peak of the interference pattern is recovered, and its width is doubled with respect to the original pattern. The peak height increases as a function of the out-of-plane field, regardless of sweep direction.

sured for different in-plane fields, applied along the trench (y-axis), together with the corresponding micromagnetic simulations.

At zero in-plane field (Figure 4.4a), we observe the aforementioned two-channel (SQUID) interference pattern, with maximum I_c at zero field. At $\mu_0 H_\mathrm{y}$ = 10 mT we observe a strong suppression of I_c for zero out of plane field. Remarkably, however, I_c is recovered upon increasing the out-of-plane field in either direction. The resulting $I_\mathrm{c}(B)$-pattern bears a resemblance to a $0-\pi$ SQUID: all the lobes are similar in width, and I_c is suppressed around zero. By increasing the H_y to 40 mT, the vortex core has traveled over 100 nm away from the junction (Figure 4.4e). Interestingly, we find the

I_c to recover for zero out-of-plane field. This reentrant behavior is accompanied by drastic changes to the $I_\mathrm{c}(B)$-pattern. The central lobe is now twice as wide, indicating a modified supercurrent distribution, which no longer corresponds to the original two channels. Even more striking is the amplitude of the I_c oscillations: instead of decaying, the lobes grow taller as we increase the magnitude of the out-of-plane field. This is the universal characteristic of $0-\pi$ junctions, i.e., a junction consisting of multiple 0 and π segments connected in parallel[53–55]. Note that the observed evolution of the interference pattern with the in-plane field cannot be attributed to stray fields or misalignment with the magnet axes since the $I_\mathrm{c}(B)$-patterns are independent of magnetic field sweep direction. More importantly, the behavior is completely absent in control samples with no LRT component (see Appendix A), which yield Fraunhofer-like patterns, regardless of the amplitude or direction of the in-plane field.

4.5. MODELING LRT GENERATION AT THE RIMS OF THE DISK

To analyze the generation of LRT correlations at the rim of the disk, we will use the linearised Usadel equations, which are spin-charge coupled diffusion equations for superconductors[7, 56]. They read:

$$[D\nabla^2 - 2(\omega + 3/\tau_\mathrm{sf})]f_s + 2(\boldsymbol{h}\cdot\boldsymbol{f}) = 0 \tag{4.1}$$

$$[D\nabla^2 - 2(\omega + 1/\tau_\mathrm{sf})]\boldsymbol{f} - 2f_s\boldsymbol{h} = 0 \tag{4.2}$$

where D is diffusion coefficient, $\boldsymbol{h}$ is the exchange field proportional to the magnetic moment, τ_sf is the spin relaxation rate and ω is the Matsubara frequency. $\hat{f}$ is the anomalous Green's function which takes into account triplet and singlet superconducting correlations, which is defined as:

$$\hat{f} = f_s\hat{\sigma}_0 + i(\boldsymbol{f}\cdot\boldsymbol{\hat{\sigma}}) \tag{4.3}$$

Here $\hat{\sigma}_0$ and $\boldsymbol{\hat{\sigma}}$ are the Pauli spin matrices, the first term corresponds to the singlet component, and the last three terms encode the triplet components. In the Supporting Information of the published material[57], we present the full technical details of the Usadel calculations; here, I present the main findings of said calculations. We now continue by describing the mechanism behind the formation of the rim currents using a model that links the vortex spin texture to the SOC.

4.5.1. MAPPING SPIN TEXTURE TO SPIN-ORBIT COUPLING

Within the cobalt weak link, the gradient of the local spin texture of the disk junctions is, at the rims of the device, not substantially larger than that of a bar-shaped device. This implies that, even though the LRT currents emerge at the rims, they are formed by a process that is sensitive to the global spin texture of the disk.

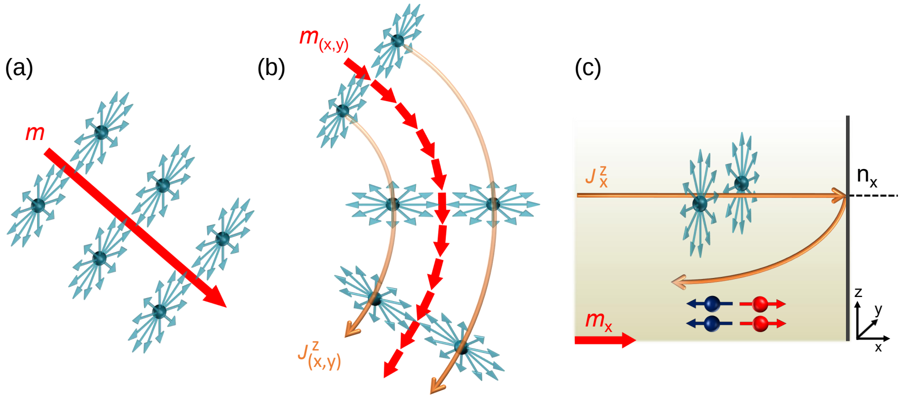

Figure 4.5: (a) SRT Cooper pairs (cyan) in a system with uniform magnetization. The SRT correlations have zero spin projection along the quantization axis, defined by the local magnetization vector $\boldsymbol{m}$ (red arrow). No equilibrium spin current (ESC) or LRT pairs are generated. (b) In the presence of spin texture, the SRT pairs continuously alter the orientation of their spin plane to remain normal to the local magnetization vector $\boldsymbol{m}_{(x,y)}$, producing an ESC $\boldsymbol{J}^z_{(x,y)}$ (orange arrows), which adiabatically follows the local spin gauge field $\nabla\theta_{\rm v} = (\boldsymbol{m}\times\nabla\boldsymbol{m})_z$. (c) When the ESC is incident on a bilayer−vacuum boundary, the adiabatic approximation breaks down. As the ESC cannot propagate outside the bilayer, the total spin current at the boundary must remain zero. To compensate for the adiabatic spin current, a condensate of LRT pairs (in red and blue) with $S_x = \pm 1$ emerges near the vacuum boundary to generate an opposing spin current. Schematic courtesy of Kaveh Lahabi.

It was demonstrated that the combination of SOC and exchange field [35, 45, 47] or Zeeman field [44, 58] can result in an equilibrium spin current (ESC) which accumulates at the superconducting/vacuum boundaries. A similar process occurs in the presence of spin texture $\boldsymbol{m}(r)$, which produces the pure gauge SU(2) field that acts as effective spin-orbit coupling denoted by $i\hat{U}^\dagger\nabla\hat{U}$[33, 34, 59]. Here, $\hat{U}(\boldsymbol{r})$ is the spin-rotation matrix, determined by the transformation to the local spin quantization axis. Note that the vortex spin texture $\boldsymbol{m} = m(-\sin\theta_{\rm v}, \cos\theta_{\rm v}, 0)$ can be transformed into a uniform one by applying this spin-rotation operation. This induces an effective SOC term $i\hat{U}^\dagger\nabla\hat{U}\,\hat{\sigma}_z\nabla\theta_{\rm v}$, through the spatial derivative of $\hat{f}$:

$$\nabla_{\rm j}\hat{f} \to \nabla_{\rm j}\hat{f} + i\nabla_{\rm j}\theta_{\rm v}[\hat{\sigma}_z, \hat{f}] = \hat{\boldsymbol{\sigma}}(\nabla_{\rm j}\boldsymbol{f} - \nabla_{\rm j}\theta_{\rm v}[\boldsymbol{z}\times\boldsymbol{f}]) \qquad (4.4)$$

Where $j = x, y, z$ is the index in coordinate space and $\theta_\mathrm{v} = \arctan[(y - y_\mathrm{v})/(x - x_\mathrm{v})]$ ($x_\mathrm{v}, y_\mathrm{v}$ are the coordinates of the vortex center). Hence, our system is analogous to one with an uniform magnetization and an intrinsic, spatially-inhomogeneous, SOC with the amplitude $|\nabla\theta_\mathrm{v}| = 1/r_\mathrm{v}$ (where r_v is the distance to the vortex core: $r_\mathrm{v} = \sqrt{(x - x_\mathrm{v})^2 + (y - y_\mathrm{v})^2}$), and therefore hosts the aforementioned ESC.

The ESC is carried by the SRT Cooper pairs, which spontaneously appear both at the bottom of the S electrodes and at the top of the F layer. The ESC can be thought of as a spin-imbalance in this SRT condensate. The direction of the ESC is determined by the in-plane gradients of the magnetic texture and flows parallel to the S–F interface. In terms of $\boldsymbol{f}$ it then becomes $J_\mathrm{j}^{\gamma} \propto |f_\mathrm{SRT}|^2(\boldsymbol{m} \times \nabla_\mathrm{j}\boldsymbol{m})_\gamma$ (here $\gamma = x, y, z$ is the index in spin space). A ferromagnetic vortex texture yields $J_\mathrm{j}^{z} \propto |f_\mathrm{SRT}|^2\nabla_\mathrm{j}\theta_\mathrm{v} = |f_\mathrm{SRT}|^2 m_\mathrm{j}/r_\mathrm{v}$ which is in accordance with the general gauge-invariant expression for the spin current[60].

4.5.2. MECHANISM FOR GENERATING LRT RIM CURRENTS

Having established the equivalency between spin texture and SOC, we now provide a possible mechanism that relates the ESC to the emergence of LRT rim currents (see Figure 4.5 for a schematic representation). In the absence of spin texture, there is no ESC (Figure 4.5a). If the spin texture gradient is nonzero, the ESC adiabatically follows the local spin gauge field ($\boldsymbol{J}^z \parallel \nabla\theta_\mathrm{v} = (\boldsymbol{m}\times\nabla\boldsymbol{m})_z$; see Figure 4.5b). When the spin current encounters the bilayer–vacuum boundary (for instance, due to deviations from the ideal circular geometry) the adiabatic approximation breaks down, resulting in an accumulation of spin at the rims of the device. Naturally, the spin accumulation decays over the spin diffusion length, which for cobalt is approximately 60 nm[61]. Near the interface, the adiabatic ESC can develop a non-zero normal component $\boldsymbol{m} \times (n_\mathrm{j}\nabla_\mathrm{j})\boldsymbol{m} \neq 0$, where $\boldsymbol{n}$ is the interface normal. Since the total spin current is zero across the boundary, $n_\mathrm{j}J_\mathrm{j}^z = 0$, the ESC is compensated by a spin current carried by an LRT condensate, which emerges near the vacuum boundary (Figure 4.5c). This leads to a coupling between $\boldsymbol{f}_\mathrm{SRT} \parallel \boldsymbol{m}$ and $\nabla\boldsymbol{f}_\mathrm{LRT} \perp \boldsymbol{m}$, such that:

$$(\boldsymbol{n}\nabla)\boldsymbol{f} = -(n_\mathrm{j}\nabla_\mathrm{j}\theta_\mathrm{v})[\boldsymbol{z} \times \boldsymbol{f}] \tag{4.5}$$

Here the right-hand side of Eq. 4.5 contains the spin current perpendicular to the bilayer–vacuum boundary. A similar SRT to LRT conversion process has been proposed to occur at the sample boundaries of S–N–S junctions with intrinsic SOC and a spin active interface[46] or in one-dimensional systems with a geometric curvature[47].

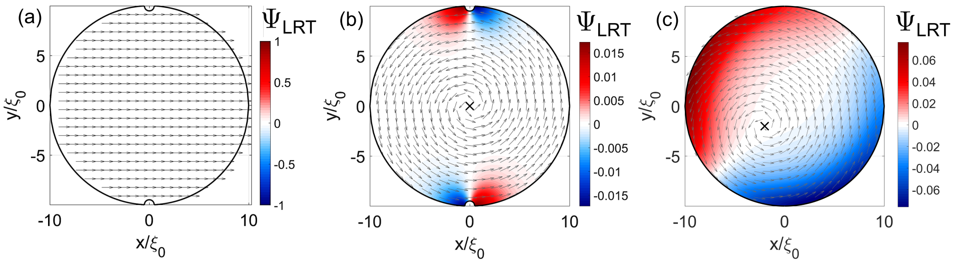

Figure 4.6: Simulated distribution of Ψ_{LRT} in a S/F bilayer for three different spin configurations, where the amplitude is normalized to $(\gamma\xi_0)f_{\mathrm{SRT}}$ (γ is the S–F interface transparency). Arrows show the direction of the in-plane spin texture. The simulated geometry includes notches that arise from FIB processing of the actual devices. (a) A homogeneous magnetization, where LRT correlations are completely absent. (b) In the presence of a magnetic vortex, LRT Cooper pairs are generated at the notches, forming two LRT current channels. (c) If the vortex core is shifted from the junction, an asymmetry arises between the signs of the LRT channels, resulting in $0-\pi$ SQUID-like configuration, also in the absence of the notches. Image courtesy of Mikhail Silaev.

By solving the linearized Usadel equation for a 2D disk-shaped S–F bilayer (without the trench), we simulate the distribution of the LRT amplitude Ψ_{LRT}, where $\boldsymbol{f}_{\mathrm{LRT}} = \Psi_{\mathrm{LRT}}(m_y, -m_x, 0)$. The results for three different spin textures are presented in Figure 4.6. For a uniform magnetization, the LRT correlations are completely absent, regardless of sample geometry (Figure 4.6a). For a perfectly symmetric vortex pattern, any deviation from the ideal circular geometry at the sample–vacuum boundary (i.e., rim roughness or disorder) results in the emergence of LRT correlations. In our simulation (Figure 4.6a,b), we use notches on the sides of the disk, also present in our devices, to demonstrate the effect of nonideal boundaries. However, in practice, any deviation from the perfect circular geometry or disorder at boundaries results in a similar outcome. Interestingly, even in the ideal circular geometry with flawless boundaries (i.e., atomically clean and smooth edges), the LRT currents would still appear if the magnetic vortex is not perfectly centered (see Figure 4.6c). Note that for perfect circular symmetry, with the vortex at the center, J_{j}^{z} will always remain parallel to m_{j} and no LRT is generated.

Our simulations also provide insights into the phase of LRT correlations. When the vortex core is aligned with the trench (at $x = 0$), the LRT currents will result in two π-channels, as indicated by the sign change of Ψ_{LRT}. In Figure 4.6c, the vortex is displaced from the center (e.g., due to an in-plane field), and the LRT channels develop opposite signs at the trench. This asymmetry is consistent with the observed $0-\pi$ SQUID interference pattern, measured under a constant in-plane field (Figure 4.4).

4.6. DISCUSSION

While the model presented here can describe the emergence of LRT correlations at the bilayer–vacuum boundaries and the appearance of spontaneous supercurrents in our junctions (i.e., $0-\pi$ segments), we should point out that this formalism is restricted to 2D slices of the bilayer. Accounting for the superconductor-vacuum interface formed by the trench is more challenging, as it requires a full three-dimensional model and the knowledge of the exact trench dimensions (e.g., its extent in the Co layer).[2]

It should be noted that there is a fundamental difference between the devices presented here and those reported in a previous work, where the disk-shaped junctions consisted of a magnetic multilayer (S$-$F$'-$F$-$F$''-$S)[21]. In contrast to the Nb/Ni/Cu/Co/Cu/Ni/Nb junctions, where long-range proximity was the result of the magnetic noncollinearity between the Co and Ni layers, the LRT correlations of the devices presented here, are generated directly by the spin texture of a single ferromagnet. This is evident from the irreversible enhancement of I_c by magnetic conditioning of the Ni 1.5 nm layer. In contrast, in the case of single ferromagnet devices, the transport characteristics are unaltered by magnetic conditioning. The vortex magnetization is the global ground state of the Co-disk: regardless of the magnetic history, the disk will revert to the vortex magnetization at zero field, which is confirmed by micromagnetic simulations. Furthermore, both types of devices exhibit radically different behavior as a function of in-plane fields. However, there are similarities: both devices show a two-channel interference pattern, although the current channels are considerably more confined in the case of a single ferromagnetic weak link.

4.7. CONCLUSION

In summary, we have revealed the interplay between triplet superconductivity and magnetic texture, which manifests as LRT supercurrents localized at the rim of the ferromagnet. We elucidate the origin of the rim currents by mapping the magnetic texture to an effective SOC, which leads to the emergence of equilibrium spin currents – carried by the triplet Cooper pairs present at the S$-$F interface. We also propose a mechanism for converting the spin currents into equal-spin LRT correlations based on the breakdown of the adiabatic approximation at the sample$-$vacuum boundaries. Lastly, we show that the nature of LRT transport undergoes drastic changes when the spin texture is modified. As illustrated here, by applying relatively small magnetic fields, the same Josephson junction can be tuned to function as both standard (0-0) and $0-\pi$ SQUIDs. The capacity to control supercurrents with the spin texture of a single ferromagnetic layer opens exciting prospects for regulating transport in superconducting devices. Since the curie temperature of the ferromagnet far exceeds the superconducting critical temperature, these spin-textured SF-hybrid devices form a prime candidate for researching non-volatile superconducting memory elements, which is the topic of the following chapter.

---

[2] For a further discussion on this topic, the reader is referred to the supplementary information of reference [57].

APPENDICES

A. CONTROL EXPERIMENTS

In this Appendix, we establish the vital role of spin texture in generating long-range triplet (LRT) correlations. Furthermore, we show that junctions, where singlet correlations dominate transport, are not affected by the spin texture and that the two-channel behavior is absent.

We fabricated control samples with a rectangular configuration, where the Co layer is uniformly magnetized along its long axis (i.e., having no spin texture). The bar-shaped devices have equal width (1 μm) and layer thicknesses as the triplet disk devices (see top inset of Figure A.1a). Due to the 5:1 aspect ratio, no magnetic vortex is stable in the cobalt layer. The same focused ion beam milling procedure was applied to form the weak link. Figure A.1a shows the resistance versus temperature of five of such junctions. For devices A to D a similar Ga-ion dose is used for preparing the trench as the triplet disk devices (Nb is completely removed from the weak link). In device E, however, the weak link is fabricated by applying a lower dose, which results in the incomplete removal of the Nb layer in the trench. As shown in Figure A.1a, only device E shows signs of short-range proximity effect, with a heavily suppressed critical current. Figure A.1b shows the $I_c(B)$-pattern of device E. In contrast to the triplet disk junctions, we observe a distorted single-channel pattern with a rapidly decaying $I_c(B)$. The pattern is shifted and distorted due to the magnetic dipole fields of the ferromagnet.

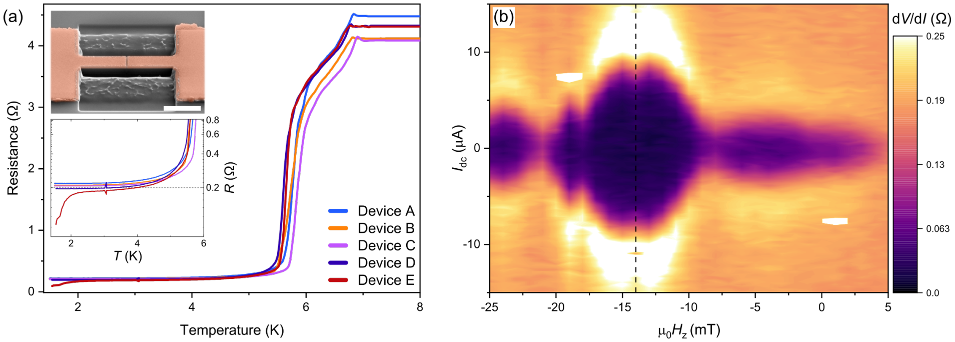

Figure A.1: (a) Resistance versus temperature obtained on five bar-shaped junctions lacking any spin texture, using a measurement current of 10 μA. The weak link in devices A to D is fabricated following the same method as the triplet disk devices. The low T resistance of these devices equals the weak link resistance (0.2 Ω). As seen from the lower inset, only device E shows weak signs of proximity effect, with a heavily suppressed critical current. This device was fabricated using a lower Ga-ion dose, resulting in an Nb-residue in the weak link. The top inset shows a false-colored scanning electron micrograph of a bar junction where the scale bar corresponds to 2 μm. (b) shows the $I_c(B)$-pattern obtained on device E. The Fraunhofer-like pattern indicates a uniform current distribution throughout the weak link. The middle lobe is shifted to -14 mT due to the magnetic stray fields of the ferromagnet.

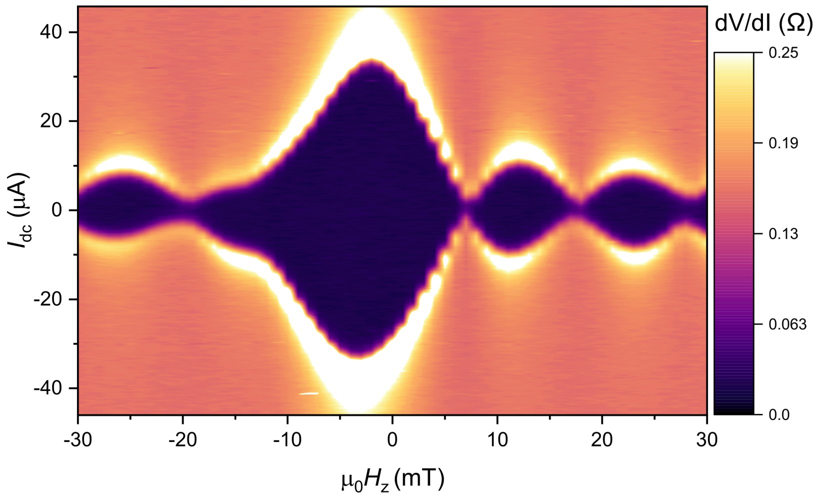

Figure A.2: $I_c(B)$-pattern recorded on a disk-shaped sample containing a shallow trench (i.e., with a Nb-residue in the weak link) and therefore dominated by singlet transport. The central peak is twice as wide as neighboring ones, and the peak height decreases in a $1/B$ fashion. Superconductivity in this sample is found to be unaffected by the removal of the spin texture of the ferromagnet by the application of an in-plane field.

Additionally, we fabricated disk-shaped control samples where the Nb is not completely removed from the weak link to study the interaction of singlet supercurrents with the vortex spin texture. Figure A.2 shows an $I_c(B)$-pattern of such a device. Contrary to the triplet devices, we observe a clear single-channel Fraunhofer-like pattern with the central lobe being twice as wide as the subsequent ones and a $1/B$ decay of the peak height. The missing minimum on the negative field side of the pattern may be attributed to a nearby Abrikosov vortex in one of the superconducting leads[62]. This demonstrates that, despite the ferromagnetic vortex in the Co-layer, the singlet supercurrent is distributed uniformly across the junction. Note that conventional weak link devices maintain their critical current, even when the spin texture is removed by applying an in-plane field. In Figure A.3 we compare the behavior of a device with triplet channels to that of a device with a shallow trench, i.e., a conventional weak link, under the influence of an in-plane field H_y along the trench. The triplet device shows variations in I_c due to 0-π transitions and vice versa, and the disappearance of the critical current around 180 mT. The conventional device containing the shallow trench (Figure A.2) retains an I_c of around 10 μA up to 2 T.

Finally, it must be noted that the two-channel behavior is not a trivial consequence of the disk configuration or a byproduct of the FIB milling used in forming the weak link, as is demonstrated by the interference patterns obtained on the S−N−S junctions presented in Chapter 3. For all those devices, we found an undistorted single-channel $I_c(B)$-pattern, corresponding to a uniform distribution of supercurrent in the junction. To summarize, our control experiments demonstrate that the rim channels only ap-

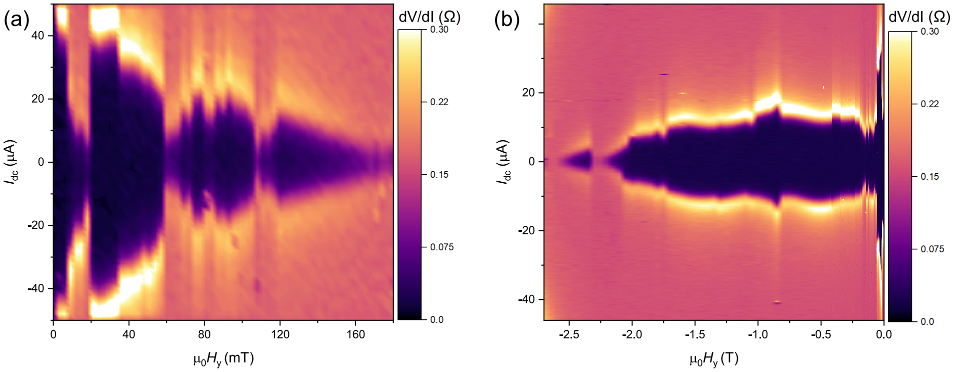

Figure A.3: In-plane $I_c(H_y)$ for a sample with triplet channels and a sample with a conventional weak link. (a) The triplet sample loses its critical current above 180 mT in-plane field along the trench. At these fields, the spin texture of the disk has become uniform and therefore the generator for LRT correlations is absent. On the sample in (a) we obtained the data shown in Figure 4.4. (b) The sample with a shallow trench retains a I_c up to above 2 T, far above the fields required for stabilizing a uniform spin texture.

pear when transport is carried by the LRT correlations. In contrast to singlet or SRT transport, the LRT currents are also highly sensitive to the changes in cobalt spin texture, which are brought about by relatively small in-plane fields.

REFERENCES

[1] Sato, M. & Ando, Y. Topological superconductors: a review. *Rep. Prog. Phys.* **80**, 076501 (2017).

[2] Hart, S. *et al.* Induced superconductivity in the quantum spin Hall edge. *Nat. Phys.* **10**, 638–643 (2014).

[3] Murani, A. *et al.* Ballistic edge states in Bismuth nanowires revealed by SQUID interferometry. *Nat. Commun.* **8**, 15941 (2017).

[4] Allen, M. T. *et al.* Spatially resolved edge currents and guided-wave electronic states in graphene. *Nat. Phys.* **12**, 128–133 (2016).

[5] Robinson, J. W. A., Piano, S., Burnell, G., Bell, C. & Blamire, M. G. Critical Current Oscillations in Strong Ferromagnetic π Junctions. *Phys. Rev. Lett.* **97**, 177003 (2006).

[6] Bergeret, F. S., Volkov, A. F. & Efetov, K. B. Long-range proximity effects in superconductor-ferromagnet structures. *Phys. Rev. Lett.* **86**, 4096 (2001).

[7] Bergeret, F. S., Volkov, A. F. & Efetov, K. B. Odd triplet superconductivity and related phenomena in superconductor-ferromagnet structures. *Rev. Mod. Phys.* **77**, 1321 (2005).

[8] Eschrig, M. & Löfwander, T. Triplet supercurrents in clean and disordered half-metallic ferromagnets. *Nat. Phys.* **4**, 138–143 (2008).

[9] Keizer, R. S. *et al.* A spin triplet supercurrent through the half-metallic ferromagnet CrO_2. *Nature* **439**, 825–827 (2006).

[10] Anwar, M. S., Czeschka, F., Hesselberth, M., Porcu, M. & Aarts, J. Long-range supercurrents through half-metallic ferromagnetic CrO_2. *Phys. Rev. B* **82**, 100501 (2010).

[11] Singh, A., Jansen, C., Lahabi, K. & Aarts, J. High-Quality CrO_2 Nanowires for Dissipation-less Spintronics. *Phys. Rev. X* **6**, 041012 (2016).

[12] Linder, J. & Robinson, J. W. A. Superconducting spintronics. *Nat Phys* **11**, 307–315 (2015).

[13] Eschrig, M. Spin-polarized supercurrents for spintronics: a review of current progress. *Rep. Prog. Phys.* **78**, 104501 (2015).

[14] Houzet, M. & Buzdin, A. I. Long range triplet Josephson effect through a ferromagnetic trilayer. *Phys. Rev. B* **76**, 060504 (2007).

[15] Khaire, T. S., Khasawneh, M. A., Pratt, W. P. & Birge, N. O. Observation of spin-triplet superconductivity in Co-based Josephson junctions. *Phys. Rev. Lett.* **104**, 137002 (2010).

[16] Robinson, J. W. A., Witt, J. D. S. & Blamire, M. G. Controlled injection of spin-triplet supercurrents into a strong ferromagnet. *Science* **329**, 59 (2010).

[17] Anwar, M. S., Veldhorst, M., Brinkman, A. & Aarts, J. Long range supercurrents in ferromagnetic CrO_2 using a multilayer contact structure. *Appl. Phys. Lett.* **100**, 052602 (2012).

[18] Leksin, P. V. *et al.* Evidence for triplet superconductivity in a superconductor-ferromagnet spin valve. *Phys. Rev. Lett.* **109**, 1–5 (2012).

[19] Iovan, A., Golod, T. & Krasnov, V. M. Controllable generation of a spin-triplet supercurrent in a Josephson spin valve. *Phys. Rev. B* **90**, 134514 (2014).

[20] Martinez, W. M., Pratt, W. P. & Birge, N. O. Amplitude Control of the Spin-Triplet Supercurrent in S/F/S Josephson Junctions. *Phys. Rev. Lett.* **116**, 1–5 (2016).

[21] Lahabi, K. *et al.* Controlling supercurrents and their spatial distribution in ferromagnets. *Nat. Commun.* **8**, 2056 (2017).

[22] Kapran, O. M., Iovan, A., Golod, T. & Krasnov, V. M. Observation of the dominant spin-triplet supercurrent in Josephson spin valves with strong Ni ferromagnets. *Phys. Rev. Res.* **2**, 1–10 (2020).

[23] Aguilar, V. *et al.* Spin-polarized triplet supercurrent in Josephson junctions with perpendicular ferromagnetic layers. *Phys. Rev. B* **102**, 024518 (2020).

[24] Komori, S. *et al.* Spin-orbit coupling suppression and singlet-state blocking of spin-triplet Cooper pairs. *Sci. Adv.* **7**, eabe0128 (2021).

[25] Fominov, Y. V., Volkov, A. F. & Efetov, K. B. Josephson effect due to the long-range odd-frequency triplet superconductivity in SFS junctions with Néel domain walls. *Phys. Rev. B* **75**, 104509 (2007).

[26] Volkov, A. F. & Efetov, K. B. Odd triplet superconductivity in a superconductor/ferromagnet structure with a narrow domain wall. *Phys. Rev. B* **78**, 1–11 (2008).

[27] Kalcheim, Y., Kirzhner, T., Koren, G. & Millo, O. Long-range proximity effect in $La_{2/3}Ca_{1/3}MnO_3$/(100)$YBa_2Cu_3O_{7-\delta}$ ferromagnet/superconductor bilayers: Evidence for induced triplet superconductivity in the ferromagnet. *Phys. Rev. B* **83**, 2–7 (2011).

[28] Aikebaier, F., Virtanen, P. & Heikkilä, T. Superconductivity near a magnetic domain wall. *Phys. Rev. B* **99**, 1–11 (2019).

[29] Silaev, M. A. Possibility of a long-range proximity effect in a ferromagnetic nanoparticle. *Phys. Rev. B* **79**, 184505 (2009).

[30] Kalenkov, M. S., Zaikin, A. D. & Petrashov, V. T. Triplet superconductivity in a ferromagnetic vortex. *Phys. Rev. Lett.* **107**, 087003 (2011).

[31] Bhatia, E. *et al.* Nanoscale Domain Wall Engineered Spin-Triplet Josephson Junctions and SQUID. *Nano Lett.* **21**, 3092–3097 (2021).

[32] Niu, Z. A spin triplet supercurrent in half metal ferromagnet/superconductor junctions with the interfacial rashba spin-orbit coupling. *Appl. Phys. Lett.* **101**, 062601 (2012).

[33] Bergeret, F. S. & Tokatly, I. V. Singlet-triplet conversion and the long-range proximity effect in superconductor-ferromagnet structures with generic spin dependent fields. *Phys. Rev. Lett.* **110**, 117003 (2013).

[34] Bergeret, F. S. & Tokatly, I. V. Spin-orbit coupling as a source of long-range triplet proximity effect in superconductor-ferromagnet hybrid structures. *Phys. Rev. B* **89**, 134517 (2014).

[35] Alidoust, M. & Halterman, K. Spontaneous edge accumulation of spin currents in finite-size two-dimensional diffusive spin–orbit coupled SFS heterostructures. *New J. Phys.* **17**, 033001 (2015).

[36] Jacobsen, S. H., Ouassou, J. A. & Linder, J. Critical temperature and tunneling spectroscopy of superconductor-ferromagnet hybrids with intrinsic rashba-dresselhaus spin-orbit coupling. *Phys. Rev. B* **92**, 024510 (2015).

[37] Satchell, N. & Birge, N. O. Supercurrent in ferromagnetic Josephson junctions with heavy metal interlayers. *Phys. Rev. B* **97**, 1–8 (2018).

[38] Jeon, K. R. *et al.* Enhanced spin pumping into superconductors provides evidence for superconducting pure spin currents. *Nat. Mater.* **17**, 499–503 (2018).

[39] Bujnowski, B., Biele, R. & Bergeret, F. S. Switchable Josephson current in junctions with spin-orbit coupling. *Phys. Rev. B* **100**, 1–9 (2019).

[40] Eskilt, J. R., Amundsen, M., Banerjee, N. & Linder, J. Long-ranged triplet supercurrent in a single in-plane ferromagnet with spin-orbit coupled contacts to superconductors. *Phys. Rev. B* **100**, 224519 (2019).

[41] Jeon, K. R. *et al.* Tunable Pure Spin Supercurrents and the Demonstration of Their Gateability in a Spin-Wave Device. *Phys. Rev. X* **10**, 31020 (2020).

[42] Satchell, N., Loloee, R. & Birge, N. O. Supercurrent in ferromagnetic Josephson junctions with heavy-metal interlayers. II. Canted magnetization. *Phys. Rev. B* **99**, 174519 (2019).

[43] Silaev, M. A., Bobkova, I. V. & Bobkov, A. M. Odd triplet superconductivity induced by a moving condensate. *Phys. Rev. B* **102**, 100507 (2020).

[44] Tokatly, I. V., Bujnowski, B. & Bergeret, F. S. Universal correspondence between edge spin accumulation and equilibrium spin currents in nanowires with spin-orbit coupling. *Phys. Rev. B* **100**, 214422 (2019).

[45] Bobkova, I. V. & Barash, Y. S. Effects of spin-orbit interaction on superconductor-ferromagnet heterostructures: Spontaneous electric and spin surface currents. *J. Exp. Theor.* **80**, 494–499 (2004).

[46] Alidoust, M. & Halterman, K. Long-range spin-triplet correlations and edge spin currents in diffusive spin–orbit coupled SNS hybrids with a single spin-active interface. *J. Condens. Matter Phys.* **27**, 235301 (2015).

[47] Salamone, T., Svendsen, M. B. M., Amundsen, M. & Jacobsen, S. Curvature-induced long ranged supercurrents in diffusive SFS Josephson Junctions, with dynamic $0-\pi$ transition. *Phys. Rev. B* **104**, L060505 (2021).

[48] Mazanik, A. A. & Bobkova, I. V. Supercurrent-induced long-range triplet correlations and controllable Josephson effect in superconductor/ferromagnet hybrids with extrinsic spin-orbit coupling. *Phys. Rev. B* **105**, 144502 (2022).

[49] Bobkova, I. V., Bobkov, A. M. & Silaev, M. A. Dynamic spin-triplet order induced by alternating electric fields in superconductor-ferromagnet-superconductor Josephson junctions. *Phys. Rev. Lett.* **127**, 147701 (2021).

[50] Prejbeanu, I. L. *et al.* In-plane reversal mechanisms in circular Co dots. *J. Appl. Phys.* **91**, 7343–7345 (2002).

[51] Natali, M. *et al.* Correlated magnetic vortex chains in mesoscopic cobalt dot arrays. *Phys. Rev. Lett.* **88**, 157203 (2002).

[52] Glick, J. A. *et al.* Phase control in a spin-triplet SQUID. *Sci. Adv.* **4**, 1–8 (2018).

[53] Smilde, H. J. H. *et al.* d-Wave–Induced Josephson current counterflow in YBa$_2$Cu$_3$O$_7$/Nb zigzag junctions. *Phys. Rev. Lett.* **88**, 057004 (2002).

[54] Scharinger, S. *et al.* Interference patterns of multifacet $20 \times (0-\pi)$ Josephson junctions with ferromagnetic barrier. *Phys. Rev. B* **81**, 174535 (2010).

[55] Gürlich, C. *et al.* Visualizing supercurrents in ferromagnetic Josephson junctions with various arrangements of 0 and π segments. *Phys. Rev. B* **81**, 094502 (2010).

[56] Usadel, K. D. Generalized diffusion equation for superconducting alloys. *Phys. Rev. Lett.* **25**, 507–509 (1970).

[57] Fermin, R. *et al.* Superconducting triplet rim currents in a spin-textured ferromagnetic disk. *Nano Letters* **22**, 2209–2216 (2022).

[58] Bergeret, F. S. & Tokatly, I. V. Theory of the magnetic response in finite two-dimensional superconductors. *Phys. Rev. B* **102**, 060506(R) (2020).

[59] Tokatly, I. Equilibrium spin currents: non-abelian gauge invariance and color diamagnetism in condensed matter. *Phys. Rev. Lett.* **101**, 106601 (2008).

[60] Hill, D., Slastikov, V. & Tchernyshyov, O. Chiral magnetism: a geometric perspective. *SciPost Phys.* **10**, 78 (2021).

[61] Bass, J. & Pratt, W. P. Spin-diffusion lengths in metals and alloys, and spin-flipping at metal/metal interfaces: an experimentalist's critical review. *J. Condens. Matter Phys.* **19**, 183201 (2007).

[62] Golod, T., Pagliero, A. & Krasnov, V. M. Two mechanisms of Josephson phase shift generation by an Abrikosov vortex. *Phys. Rev. B* **100**, 174511 (2019).

5

MESOSCOPIC SUPERCONDUCTING MEMORY ELEMENTS BASED ON BISTABLE MAGNETIC TEXTURES

R. Fermin, N. Scheinowitz, J. Aarts & K. Lahabi

With the ever-increasing energy need to process big data, the realization of low-power computing technologies, such as superconducting logic and memories, has become a pressing issue. Developing fast and non-volatile superconducting memory elements, however, remains a challenge. Superconductor-ferromagnet hybrid devices, like the ones presented in Chapter 4, offer a promising solution, as they combine ultra-fast manipulation of spins with dissipationless readout. In this chapter, we present a new type of non-volatile Josephson junction memory that utilizes the bistable magnetic texture of a single mesoscopic ferromagnet. We use micromagnetic simulations to design an ellipse-shaped planar junction structured from an Nb/Co bilayer. The ellipse can be prepared as uniformly magnetized or as a pair of vortices at zero applied field. The two states yield considerably different critical currents, enabling reliable electrical readout of the element. We describe the mechanism used to control the critical current by applying numerical calculations to quantify the local stray field from the ferromagnet, which shifts the superconducting interference pattern. Our approach presents a novel route towards realizing superconducting memory applications by combining micromagnetic modeling with bistable spin-textured junctions.

This chapter is based on the paper published in *Phys. Rev. Res.* **4**, 033136 (2022).

5.1. INTRODUCTION

In recent years, energy-hungry data centers have accounted for more than 1% of the global electricity consumption, which is projected to increase to 3-13% by 2030[1]. As data centers are responsible for 0.3% of the overall carbon emissions, the development of low-power supercomputers has become an immediate global concern[2]. Due to their non-dissipative nature, superconducting logic and memory devices present a tantalizing route to address this issue, promising enormous savings, even accounting for cryogenic cooling[3–7]. While several classes of high-performance superconducting processors already exist, cryogenic memories remain relatively underdeveloped. Non-volatility and scalability, in particular, have been the major obstacles in the industrial realization of superconducting memories.

The combination of superconducting and ferromagnetic elements can tackle the non-volatility issue through S−F−S devices, in which different (stable) magnetic configurations yield different critical supercurrents. Much work has been done on stacked magnetic Josephson junctions with a weak ferromagnetic barrier, where small magnetic field pulses could switch the critical current. [8–11] However, the weak ferromagnet used in such systems has a typically low Curie temperature (around 10 K), limiting their non-volatility. Josephson memories have also been extensively studied in so-called pseudo-spin-valve (S−F−N−F′−S) devices, where the magnetization of two ferromagnetic layers, separated by a normal metal, could be set parallel or antiparallel to yield a change in critical current. [12–18] The work on pseudo-spin-valves has also been extended to multilayer Josephson devices featuring triplet supercurrents, which not only carry charge but also spin. [19, 20] Finally, all-oxide devices, which can operate at high temperatures, were recently examined. [21] In general, the existing non-volatile Josephson memories utilize an intricate layer set and face several obstacles, such as interlayer coupling between magnetic layers and stochastic distribution of magnetic flux in the junction. Other problems include insufficient contrast between states for electrical readout, and the requirement for applying a large writing field.

In this chapter, we address these challenges and present an alternative route for developing non-volatile Josephson memory elements, where information is stored by the spin texture of a single mesoscopic ferromagnet. Magnetic textures, in general, and specifically ferromagnetic vortices, can be manipulated by applying pulsed microwave radiation, leading to the realization of ultra-fast electronics[22–24]. Combining information inscription in spin textures with the non-dissipative nature of supercurrents can thus lead to the realization of high-speed, low-power, and non-volatile memory elements. Furthermore, the synergy between superconductivity and magnetic textures is amplified further by allowing for triplet supercurrents, paving the road for superconducting spintronics[25–27]. Textured S−F-hybrid devices open a new paradigm in superconducting memory applications.

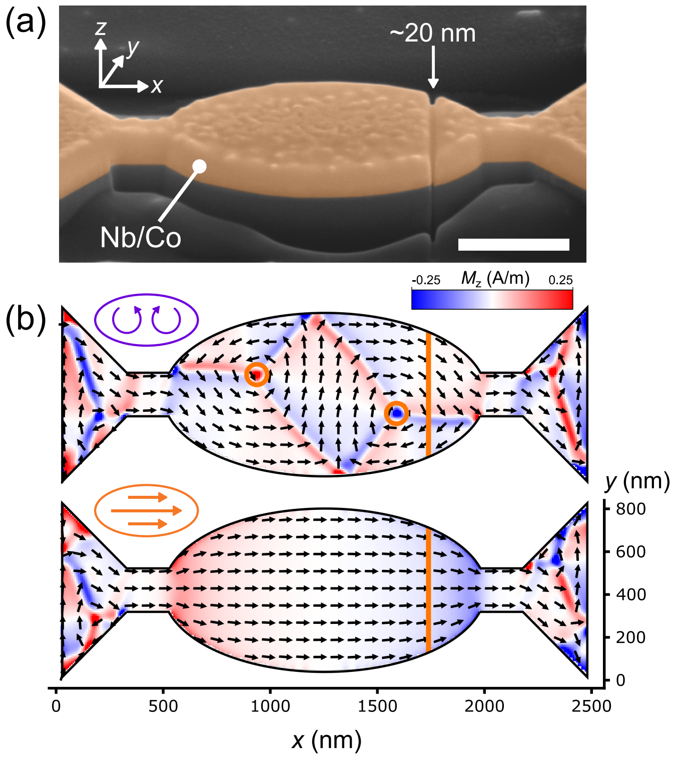

Figure 5.1: (a) False colored scanning electron micrograph of the ellipse-shaped S–F–S junction device A. The Co weak link is formed by the indicated trench (∽20 nm in size) that separates the two Nb electrodes. The scale bar corresponds to 500 nm. (b) Shows the simulated bistable spin textures at zero field. The cobalt is either magnetized along the long axis of the device (M-state) or hosts two stable vortices (V-state). Orange circles highlight the vortex cores, and the orange line indicates the trench location. The color scale indicates the out-of-plane magnetization of the top of the cobalt layer.

Here we show the realization of a micrometer-sized superconducting memory element based on bistable spin textures in the F-layer of elliptical versions of the S–F–S Josephson junctions presented in Chapter 4. By combining micromagnetic simulations with nanostructured hybrid devices, we are able to control the transport behavior of our devices with their magnetic texture. By applying a magnetic field of 40 mT as the writing operation, we can reliably switch between two stable spin textures: one is uniformly magnetized, and the other hosts a pair of ferromagnetic vortices. These correspond to minimum and maximum critical supercurrent of the junction, respectively. We obtain a factor of five difference in the critical current between the two states, which allows for a facile and reliable electrical readout of the element. By quantifying the local stray field from the ferromagnet, we show that the difference in critical current is caused by a shift in the superconducting interference pattern. Moreover, the magnetic bistability enables us to use writing fields that are considerably smaller than the local stray field from the ferromagnet. We confirm the memory is stable, non-volatile, and non-destructive upon readout.

5.2. ELLIPSE-SHAPED S–F–S JUNCTIONS

Using the procedure described in Chapter 3, we prepare elliptical S–F–S junctions from a cobalt (65 nm) niobium (50 nm) bilayer (deposited in an ultra-high vacuum by Ar-sputtering). Figure 5.1a shows a false-colored scanning electron micrograph of such an ellipse device, having dimensions of 1500 nm by 750 nm (long and short axes, respectively). Micromagnetic simulations show that the zero-field spin texture of such devices is expected to be bistable: either the cobalt layer is magnetized along the long axis of the ellipse (we call this the M-state) or two ferromagnetic vortices are stable near each focal point of the ellipse (V-state). We depict simulation results from these states in Figure 5.1b. The full technical details of the simulations are presented in Appendix A. Essentially, this allows for writing a bit with the value "0" (M-state) or "1" (V-state) into the spin texture of the device. We prepare the states by first applying a 40 mT in-plane field either parallel to the long or short axis of the devices. Next, after removing the field along the short (long) axis, the V-state (M-state) is stable in the device.

The trench is positioned near the focal point of the ellipse, which corresponds to the approximate location of a vortex core in the V-state. As discussed later, this particular location is designed to optimize the stray field-driven mechanism used to assign different critical currents to the M- and V-states. In this chapter, we describe two of these elliptical devices (devices A and B), although all observations are repeated for a large number of samples. Figure 5.2 shows the resistance versus temperature of device A, measured with a current of 20 µA. If the sample is prepared in the V-state, we find two transitions. The first corresponds to the bulk superconducting critical temperature of the Nb layer, the second is due to the superconducting proximity effect in the S–F–S junction formed by the trench. In contrast, the M-state does not show a second tran-

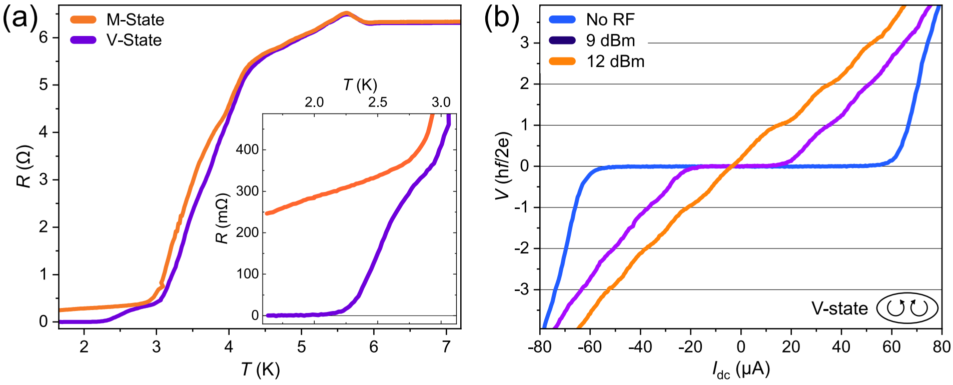

Figure 5.2: Basic transport characteristics of device A. In (a) we show the resistance versus temperature curves for both the M- and V-state, measured using 20 µA current bias. The critical current is suppressed below 20 µA in the M-state. The inset shows the low-temperature behavior. (b) depicts three IV-characteristics of the sample in the V-state, acquired under different RF radiation powers. The frequency is 1.6 GHz, and the temperature is 1.6 K. The measured voltage is normalized to $hf/2e$, and shows a clear Shapiro response.

sition, indicating that the critical current of the junction in this state is suppressed to below the measurement current. This difference in I_c between the two states allows us to read out the magnetic state of the memory element electrically. To unambiguously demonstrate the superconducting proximity effect in our devices, we show the appearance of Shapiro steps in the IV-characteristic of device A under the application of RF radiation, which is supplied by a nearby antenna. We carry out these measurements at 1.6 K in the V-state. The step height in the IV-characteristic shown in Figure 5.2b is in units $hf/2e$ (where h is the Planck constant, f is the frequency of the RF radiation, and e the electron charge), confirming the Shapiro response.

5.3. CONTROLLABLE SWITCHING

To show the bistability of the spin textures, we examine the dependence of I_c on the in-plane 'writing' fields H_x and H_y along the long and the short axis of the ellipse, respectively. The results are shown in Figure 5.3a,b, accompanied by the simulated spin textures in Figure 5.4. If the sample is in the M-state ("0"), I_c is 5 μA. The datum "1" can be written by increasing the field along the short axis of the ellipse. At a field of 40 mT, I_c grows to above 20 μA, which is accompanied by a buckling of the simulated spin texture. Upon decreasing the field to zero, the high I_c state is retained, and the buckled spin texture evolves into two vortices. Therefore, the device is converted into the V-state ("1"). Conversely, the M-state can be written in the device by applying a field parallel to the long axis of the ellipse. The field effectively displaces the vortices towards the edges of the sample. At a field of 15 mT, they are fully pushed out from the ellipse, and the spins align in the M-state. This is accompanied by a drop in I_c back to 5 μA. The low I_c is stable upon decreasing the field back to zero in the M-state.

Figure 5.3c,d show the total energy associated with the simulated spin texture as a function of externally applied field (i.e., the sum of the exchange, demagnetization, and Zeeman energies). Two branches can be discerned corresponding to the two states, both stable at zero field. In the simulations, the buckled state, which is required for the stabilization of the V-state state, appears above 45 mT. During the converse switching operation, a field of 25 mT is required to magnetize the ellipse. Remarkably, we find that both fields closely follow the experimental values with only a slight offset, which can be attributed to the reduced geometry of the contacts and the finite field steps used in the simulations.

We examine the performance of our devices by repeatably switching them between the two states while studying the transport behavior. Figure 5.5a shows the zero-field IV-characteristic of the two states. Based on the difference in I_c, we can define a readout current corresponding to a finite voltage in the M-state, but a zero voltage in the V-state. We cycle the device between the two states (using a 40 mT field) and acquire the voltage at the readout current in each state. In Figure 5.5b, we show a histogram of the measured voltage at a readout current of 30 μA, totaling 78 subsequent writing cycles. There is no overlap in the histogram, making the states highly distinguishable. Since the readout current density is far too low to alter the spin texture, the readout operation is fully non-destructive. Furthermore, by heating the ellipse to above the T_c of the superconducting layer between subsequent write and read operations, we confirm the non-volatility of its memory. This holds even when the sample is warmed to room temperature and stored for days. Additionally, to test the resilience to perturbations of the spin texture, we try to cycle between the states using a field of 10 mT. We find these fields insufficient to alter I_c, demonstrating the stability of our devices.

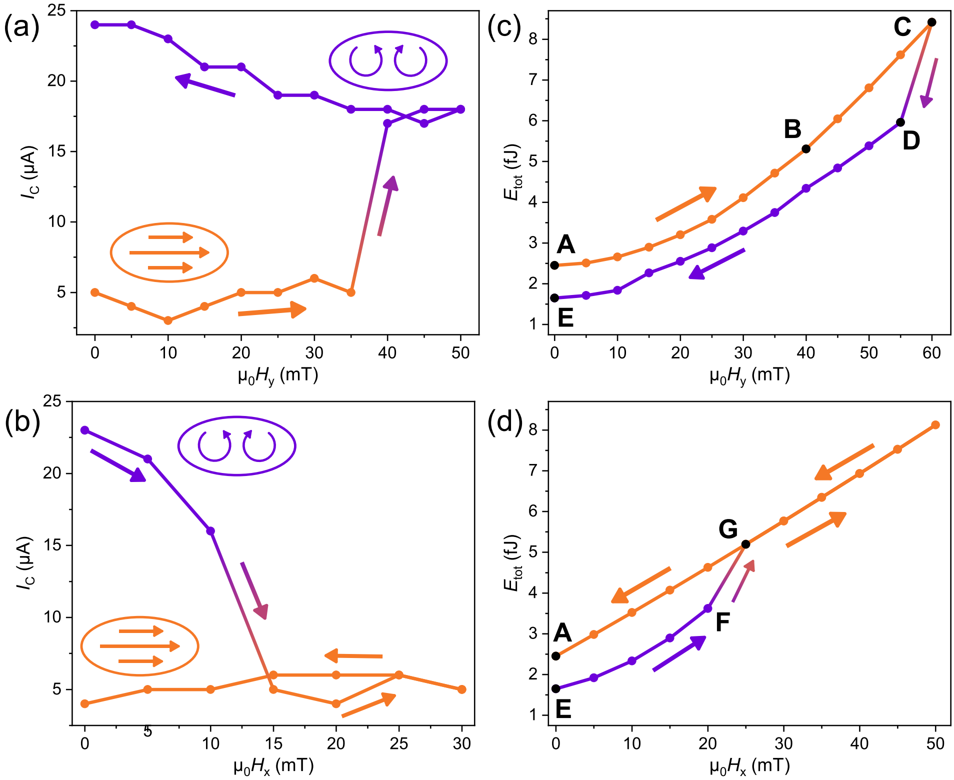

Figure 5.3: The critical current I_c, the total simulated energy E_{tot} and the spin texture of the device as a function of H$_x$ (field along the long axis), and H_y (along the short axis). Results obtained on device B at 1.7 K. (a) and (b) depict $I_c(H_y)$ and $I_c(H_x)$. In (a), the field is increased along the short axis of the ellipse. At 40 mT I_c increases sharply, effectively transforming the M-state into the V-state. The reverse operation is shown in (b): by increasing the field - parallel to the long axis of the ellipse - to 15 mT, the critical current drops to 5 μA, bringing the device back to the M-state. (c) and (d) show E_{tot} corresponding to the in-plane field sweeps. Two branches can be seen in both panels, corresponding to the V- and M-state. A change of magnetic state coincides with a jump from one branch to the other. We can predict the switching fields correctly within a small error. Snapshots of the spin texture during the simulations in (c) and (d) are shown in Figure 5.4. These data points are colored black in (c) and (d) and labeled with boldface letters accordingly.

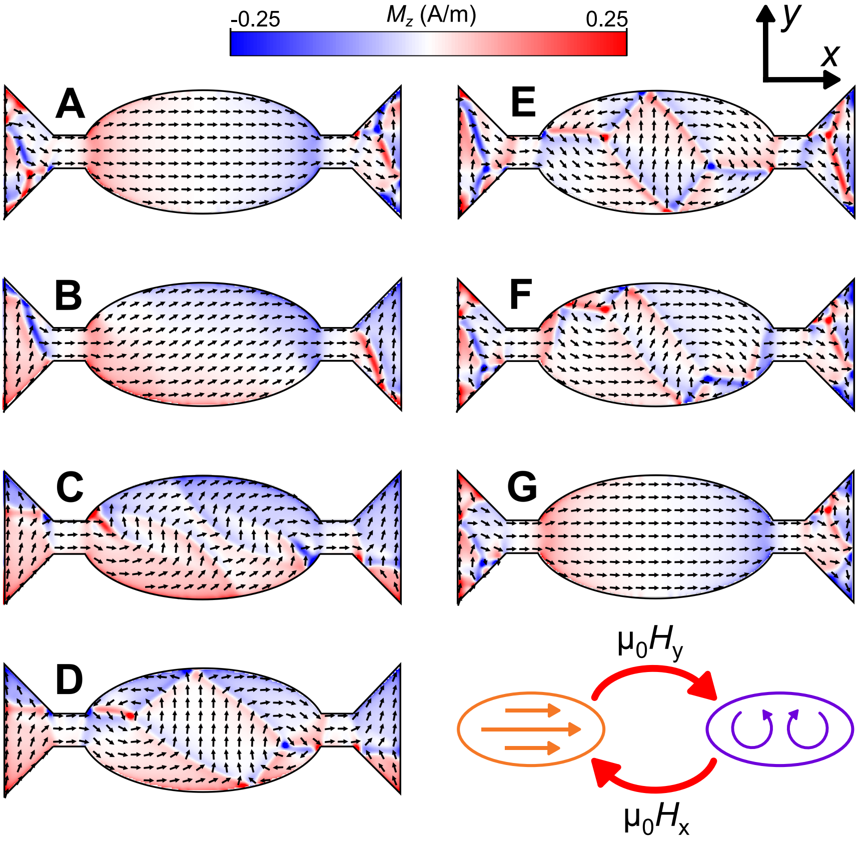

Figure 5.4: Snapshots of the spin texture during the simulated field sweeps presented in Figure 5.3. Here the color scale indicates the magnetization of the top of the Co-layer and the boldface letters correspond to the ones in Figure 5.3c,d.

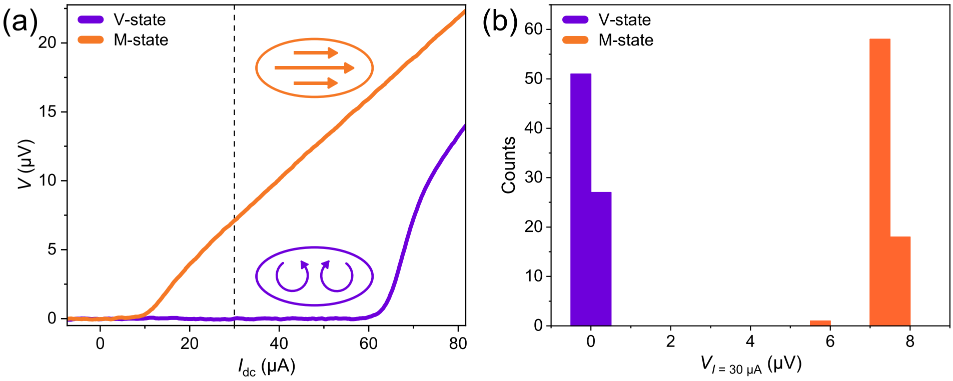

Figure 5.5: Fidelity of the writing cycles of device A. The IV-characteristics of the two states, measured at 1.6 K, are shown in (a). Based on these curves, we define a readout current corresponding to a finite voltage in the M-state and zero voltage in the V-state. We cycle the device between the two states 78 times and measure the voltage before each subsequent switch. (b) shows a histogram of the readout voltages, measured using a 30 μA current (the dotted line in (a)).

5.4. STRAY FIELD DRIVEN MECHANISM

We now discuss the mechanism used for suppressing the I_c in the M-state, based on the local stray field emerging from the ferromagnet. To illustrate this, we obtain the $I_c(B)$-pattern for Junction B. Note that the magnitude of the out-of-plane fields is insufficient to alter the global spin texture of the device (i.e., the out-of-plane fields cannot transform the M-state to the V-state or vice versa). We present such measurements, obtained on sample B, for the V-state and the left and right magnetized M-state in the color maps of Figure 5.6a-c. For this sample, we observe a pattern with a single middle lobe and heavily suppressed side lobes. Samples with higher I_c values show a Fraunhofer-like interference pattern, indicating a uniform distribution of I_c throughout the weak link, as can be seen in Appendix B, where we present additional interference patterns. The pattern is centered at zero field for the V-state (Figure 5.6c). By

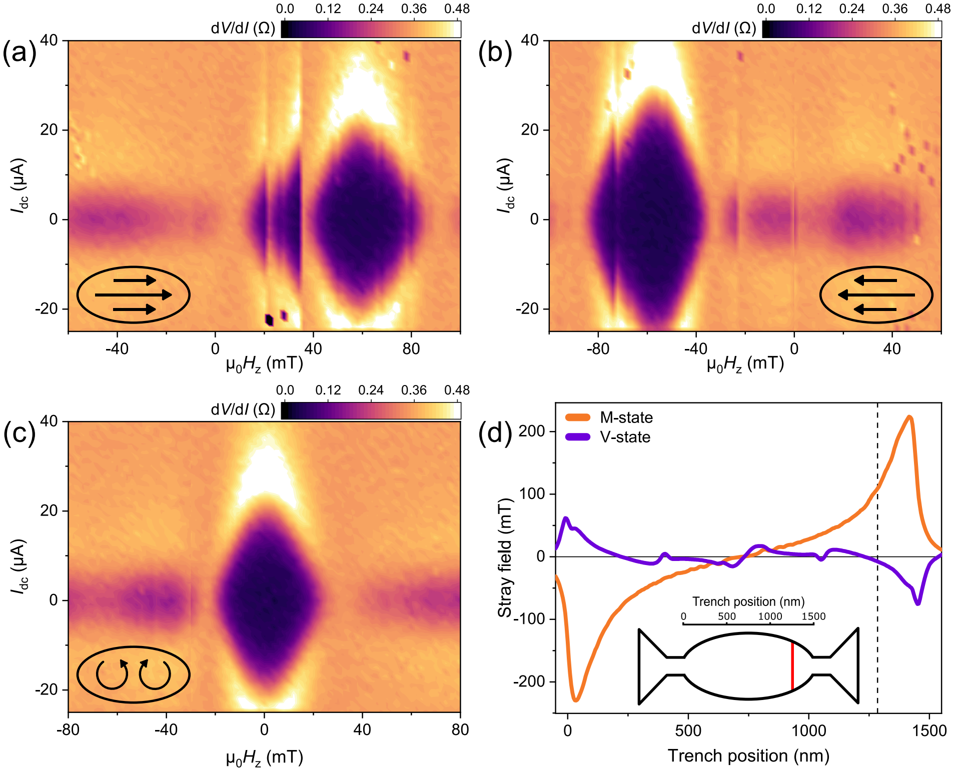

Figure 5.6: Stray fields cause a shift in $\mathrm{I_C}$. (a) to (c) respectively show the superconducting interference patterns in the right magnetized M-state, left magnetized M-state, and the V-state obtained on device B. Although the shape of the $I_c(B)$-pattern does not change, the middle lobe of the pattern is shifted in the V-state with respect to the pattern in the M-state (for both magnetizations). Some measurement glitches are visible in (a) and (b): these result from sudden small magnetic configurations in the sample. Stray fields from the ferromagnetic layer cause the shift, as is demonstrated in (d): the simulated field shift for different trench locations. The vertical line in (d) corresponds to the actual location of the trench (see Figure 5.1). The inset shows the geometry of the sample with the corresponding scale distribution. The red line indicates the actual location of the trench.

switching to either of the M-states (Figure 5.6a,b), the shape of the $I_c(B)$-pattern is not altered, yet shifted by around 60 mT from zero applied field. Moreover, the magnetization direction in the M-state determines the sign of this shift. Therefore, it is evident that the suppressed I_c of the M-state is a result of the local stray fields from the Co layer, introducing a shift in the $I_c(B)$-pattern. However, what makes our spin-textured devices truly stand out from previous Josephson memory elements, is that we use a writing field (40 mT) that is noticeably smaller than the resulting shift (60 mT).

In the following, we describe how the pattern shift can be quantified by simulating the stray flux entering the junction. We sum the z-component of the flux - evaluated in a thin sheet above the Cobalt layer - over an integration window to obtain the local stray fields threading area of the window. The size of this window is chosen to reflect the trench area, yielding an estimate of the stray fields penetrating the junction. Figure 5.6d displays the simulated (stray field-induced) pattern shift as a function of the window location; the vertical line indicates the location of the trench in the actual sample. This shows that the V-state corresponds to negligible stray fields penetrating the junction, accounting for the symmetric pattern in Figure 5.6c lacking horizontal offset. The M-state corresponds to an 80 mT shift, which closely follows the 60 mT offset in the $I_c(B)$-patterns. Note that the simulated stray field is symmetric with respect to the center of the sample. This reflects the sign change that occurs when the magnetization direction is reversed.

Note that the spin texture snapshots of Figure 5.4 show the source of the stray fields. In the M-state, the ellipse features a dipole-like field along its long axis, which is absent in the V-state. We do observe some stray fields in the V-state, although these average out over the junction area. Therefore the total shift in the $I_c(B)$-pattern remains zero. During the field sweep along the short axis of the ellipse (i.e., switch from M-state to V-state), the spin texture buckles before two vortices stabilize, as can be seen in the snapshots **B** and **C** in Figure 5.4. When this buckling occurs, the dipole-like field no longer points along the long axis of the ellipse, and consequently, the stray fields average out over the junction area. This explains why the high I_c state occurs before two vortices enter the ellipse.

5.5. PAIRING SYMMETRY OF THE SUPERCURRENTS

In Chapter 4, we found spin texture to be a prerequisite for the superconducting proximity effect, which led to the conclusion that the transport in the disk-shaped S–F–S junctions is dominated by long-range triplet (LRT) Cooper pairs. In this case, however, we cannot be certain about the LRT scenario. Due to the similarity to the circular devices, LRT correlations can be expected in the V-state of the ellipse-shaped devices described here. However, there are several inconsistencies; the most notable ones are discussed here. First, contrary to the disk-shaped devices, removing the spin texture from our junctions does not suppress the proximity effect, i.e., the maximum of $I_c(B)$ for both the M- and V-states are quite similar. Secondly, while the $I_c(B)$-patterns of the disk-shaped devices are highly sensitive to the subtle changes in the spin texture, the elliptic junctions show the same type of pattern for widely different magnetic states. These observations seem to counter the notion of the LRT correlations and indicate that transport in the elliptic junctions is carried by the short-range triplet correlations instead. However, one could argue that even the M-state still features some spin texture near the edges of the sample (due to the narrow tapered shape of the ellipse; see Figure 5.1b), which possibly allows for the generation of LRT correlations. Finally, the similar $I_c(B)$-patterns between the magnetic states can possibly be caused by the relatively short junction width. Indeed, the length of the trench in the disk-shaped devices is typically between 1 μm and 1.6 μm, whereas the trench length of the ellipse devices presented here is less than 600 nm; the current channels might therefore overlap sufficiently to produce a single channel interference pattern. At this stage, no conclusions can be drawn on the triplet or singlet nature of the supercurrents in the elliptical devices, and further experiments are necessary. We emphasize, however, that the mechanism for the shift in the $I_c(B)$-patterns (i.e., the stray fields) holds for both singlet and triplet pairing symmetries.

5.6. CONCLUSION AND OUTLOOK

We demonstrate the realization of a non-volatile superconducting memory element based on magnetic textures in an S–F–S Josephson junction. The ellipsoidal shape of the device leads to two stable magnetic states at zero applied magnetic field: a fully magnetized state and a state containing ferromagnetic vortices. These can be associated with the data "0" and "1", respectively. By applying and removing an externally applied in-plane field, we can reliably switch between these states, performing a write operation. We find a strong suppression of the critical current in the magnetized state, which allows for a non-destructive determination of the spin state, and therefore, electrical readout of the bit. By combining transport experiments and micromagnetic simulations, we show that the difference in critical current between the two states results from internal stray fields originating from the ferromagnetic layer of the device, which creates a local offset field in the junction. Since the ferromagnetic textures can be controllably manipulated with RF radiation, storing information in mesoscopic S–F devices can provide an exciting avenue for realizing ultra-fast electronics. Besides, strain-mediated switching of similar elliptical devices has been recently theoretically studied and shown to be a good alternative to switching using externally applied fields[28]. Combined with the possibility of long-range triplet supercurrents in hybrid devices, the memory devices presented here can form an essential building block for superconducting spintronics.

APPENDICES

A. MICROMAGNETIC SIMULATIONS

The micromagnetic simulations on the elliptical samples are performed using the GPU-based MuMax^3 program[29]. The cobalt layer is divided into a mesh of 5 nm cubic cells. The exchange coefficient is set to 3×10^{-11} J/m, and the saturation magnetization is 1.4×10^{-6} A/m. We choose the Gilbert damping constant to be 0.5, to allow for faster convergence and therefore increased computation speed. As the cobalt film is polycrystalline due to the Ar-sputtering method, we use a zero anisotropy constant. The micromagnetic simulations of the disk devices presented in the previous chapter are carried out within the Object Oriented MicroMagnetic Framework (OOMMF) simulation software. A full description of these simulations is reported elsewhere, although the parameters used are identical to those described here[30]. The only difference lies in the calculation method: OOMMF is CPU-based, whereas MuMax^3 is GPU-based.

We have included vacuum cells around the magnetic structure in all our simulations. These feature no spin, yet magnetic fields can penetrate them. Therefore, in each steady-state solution, we gain full insight into the stray fields around the magnetic layer. In order to calculate the stray fields penetrating the junction, we sum the z-component of these stray fields directly above the magnetic layer (i.e., penetrating the superconducting layer perpendicular to the charge transport direction). We define a window of area A and find the field penetrating this window by dividing the flux Φ by its area. The total flux is given by the sum of the flux in each cell, which is determined by the product of the z-component of the field penetrating the cell and the cell area. Since each cell has the same area by design, this leads to:

$$\Delta B = \frac{\Phi}{A} = \frac{1}{A}\sum B_{z,\mathrm{i}}\, A_{\mathrm{cell,i}} = \frac{1}{N_{\mathrm{cells}}}\sum B_{z,\mathrm{i}} \tag{5.1}$$

Here we recognize that the total field penetrating the window equals the average field per cell, which can be evaluated from the simulation results.

Ideally, the area of the integration window is chosen to reflect the effective area of the junction. However, in Chapter 3, we found that devices of these dimensions are in the non-local limit. The effective area is therefore determined by the geometry and not by λ_{L}. Moreover, although we provide a method for calculating the magnitude of the effective area in Chapter 3, we cannot specify the geometry of this area. Besides, due to the taped shape of the ellipse, using the calculated effective area and assuming a rectangular junction area would lead to incorrectly accounting for fields outside the sample geometry. More importantly, evaluating the effective area would require a separate calculation for each junction position, a process that is, as of now, not automatized (i.e., for every geometry, the Neumann boundary conditions are found by hand).

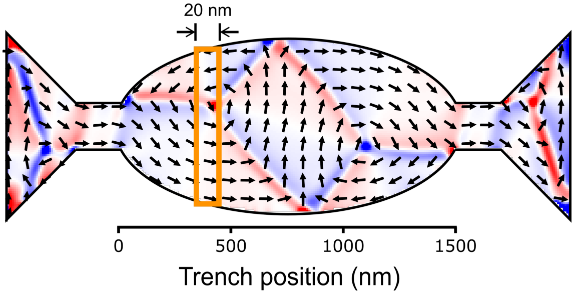

Figure A.1: Graphical representation of the integration window, used to calculate the local stray fields (in orange). The integration window is chosen to reflect the size of the physical junction. The width equals that of the trench (20 nm), and the length is equal to the local width of the ellipse. By positioning the integration window at different locations (i.e., trench positions), we can evaluate the stray fields at different locations along the ellipse. The axis labeled ‘Trench position’ coincides with the x-axis of Figure 5d of the main text.

We also assumed symmetric superconducting electrodes in our calculations presented in Chapter 3. When the trench is not centered, the superconducting electrodes are not symmetric, complicating the calculations. In order to solve these issues, we specify a rectangular window with a fixed width (set by the junction width: 20 nm) and a variable length. We match the length of the window to that of the local width of the ellipse. By this choice, we minimize the summation of the field outside the device geometry. By varying the location of the center of the integration window, we evaluate an expression of the stray fields that locally penetrate the superconductor. A graphical representation of the integration window is shown in Figure A.1.

B. ADDITIONAL DATA

In this chapter, we provide results on two different devices, named A and B. In this Appendix, we provide additional data obtained on these samples. Supporting Figure B.1 shows the in-plane field sweeps obtained on device A. Similar to device B, there is a transition from the M-state to the V-state at 40 mT when increasing the field along the short axis of the ellipse. This is accompanied by an increase in critical current, which is retained upon reducing the field to zero. The converse operation is carried out by applying the field along the long axis of the ellipse. We find that 5 mT is sufficient to reduce the critical current to the value corresponding to the M-state. This is lower than the corresponding field for device B (15 mT). Figure B.2 shows the typical IV-characteristics of the V-state and M-state for device B. A clear voltage difference is measured at a readout current of, for example, 15 µA. No histogram was obtained on this device. Finally, we present a full dataset obtained on a third device in Figures B.3,B.4 and, B.5, named device C.

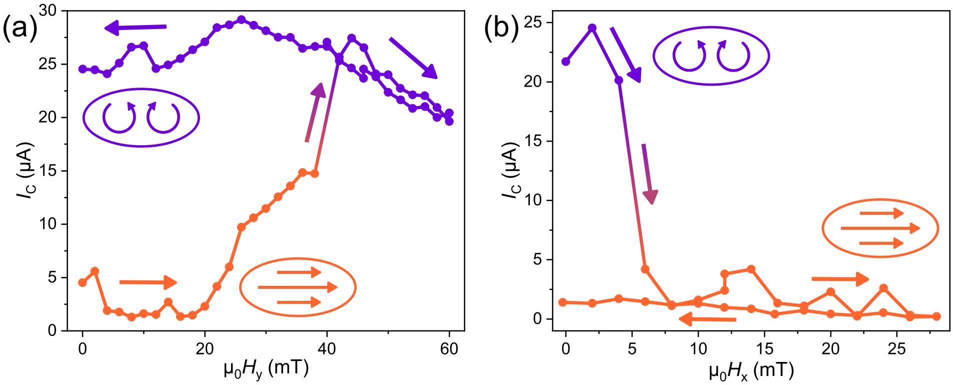

Figure B.1: The critical current I_c as a function of H_x (field along the long axis), and H_y (field along the short axis). Similar data as presented in Figure 5.3 of the main text, obtained on device A at 1.7 K. (a) and (b) depict $I_c(H_y)$ and $I_c(H_x)$ respectively. In (a) the field is increased along the short axis of the ellipse. Like sample B, at 40 mT I_c increases sharply, effectively transforming the M-state into the V-state. By increasing the field parallel to the long axis of the ellipse (shown in (b)), the critical current drops to the low I_c state at 5 mT. This is lower than the 15 mT, needed to switch device B.

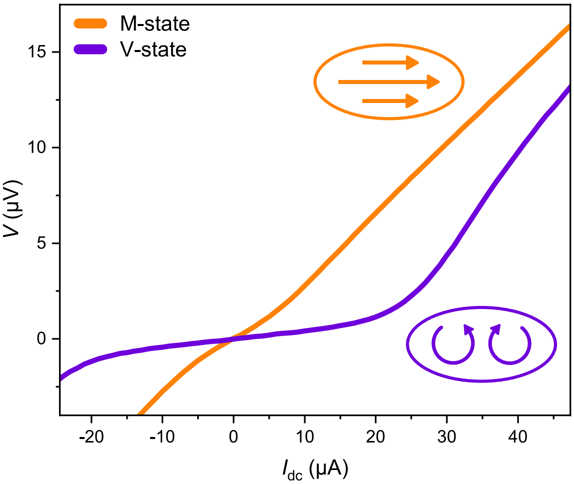

Figure B.2: The typical IV for both states in device B. By choosing a proper read-out current (e.g. 15 µA), a clear voltage difference between the two states can be measured.

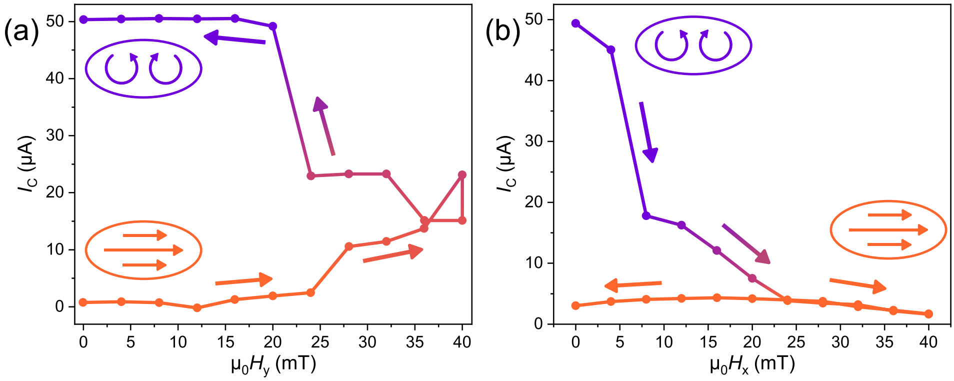

Figure B.3: The critical current I_c as function of H_y (field along the short axis, shown in (a)), and H$_x$ (field along the long axis, shown in (b)). Similar data as presented in Figure 3 of the main text, obtained on a third device, called device C. Data acquired at 2 K. In (a), the field is increased along the short axis of the ellipse; by increasing the field to 40 mT, the spin texture is buckled and upon reducing the field to zero, the V-state and entailing high I_c state is retrieved. By increasing the field parallel to the long axis of the ellipse, the critical current drops to the low I_c state corresponding to the M-state.

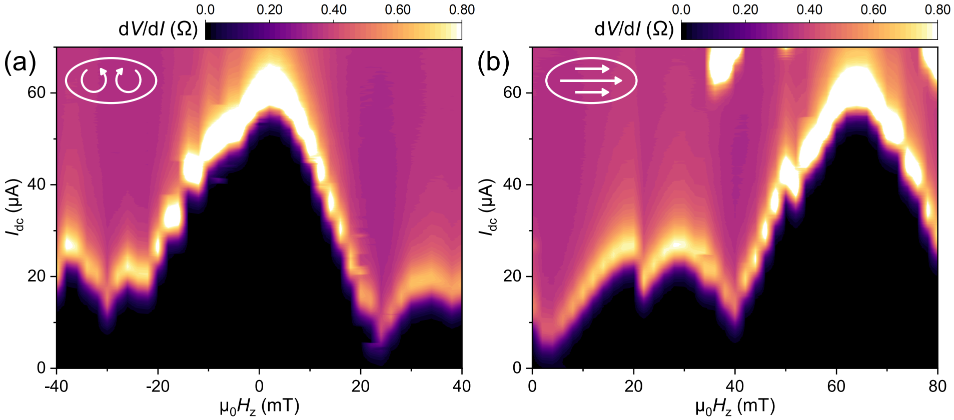

Figure B.4: (a) to (b) respectively show the $I_c(B)$-patterns in the V-state and the M-state in a third device, named device C. Although the shape of the $I_c(B)$-pattern does not change, the center lobe of the pattern is shifted in the V-state with respect to the pattern in the M-state. This is the same behavior as observed for device B (presented in the main text).

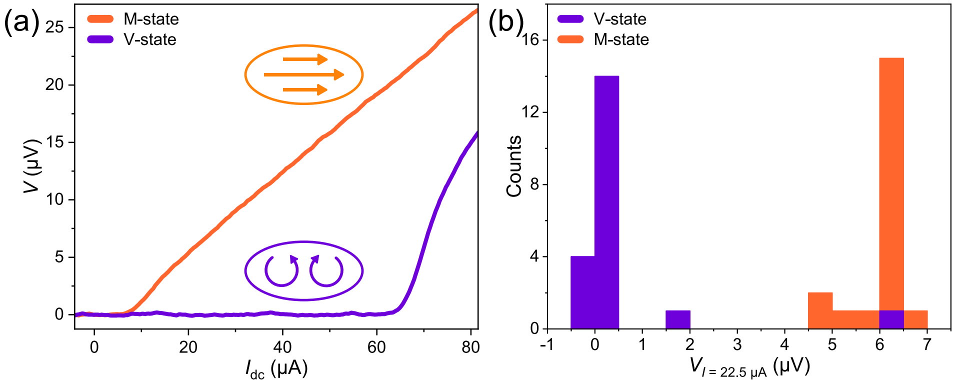

Figure B.5: Fidelity of writing cycles in a third device, named device C. In (a) we show the IV-characteristic for both states. We define a read-out current of 22.5 μA. We cycle the device between the states 20 times and record the voltage at the read-out current. (b) shows a histogram of these voltages.

REFERENCES

[1] Andrae, A. & Edler, T. On Global Electricity Usage of Communication Technology: Trends to 2030. *Challenges* **6**, 117–157 (2015).

[2] Jones, N. How to stop data centres from gobbling up the world's electricity. *Nature* **561**, 163–166 (2018).

[3] Holmes, D. S., Ripple, A. L. & Manheimer, M. A. Energy-Efficient Superconducting Computing—Power Budgets and Requirements. *IEEE Trans. Appl. Supercond.* **23**, 1701610–1701610 (2013).

[4] Soloviev, I. I. *et al.* Beyond Moore's technologies: Operation principles of a superconductor alternative. *Beilstein J. Nanotechnol.* **8**, 2689–2710 (2017).

[5] Chen, L. *et al.* Miniaturization of the superconducting memory cell via a three-dimensional Nb nano-superconducting quantum interference device. *ACS Nano* **14**, 11002–11008 (2020).

[6] Butters, B. A. *et al.* A scalable superconducting nanowire memory cell and preliminary array test. *Supercond. Sci. Technol.* **34**, 035003 (2021).

[7] Hilgenkamp, H. Josephson Memories. *J. Supercond. Nov. Magn.* **34**, 1621–1625 (2021).

[8] Larkin, T. I. *et al.* Ferromagnetic Josephson switching device with high characteristic voltage. *Appl. Phys. Lett.* **100**, 222601 (2012).

[9] Vernik, I. V. *et al.* Magnetic Josephson junctions with superconducting interlayer for cryogenic memory. *IEEE Trans. Appl. Supercond.* **23**, 1701208 (2013).

[10] Caruso, R. *et al.* RF assisted switching in magnetic Josephson junctions. *J. Appl. Phys.* **123**, 133901 (2018).

[11] Caruso, R. *et al.* Properties of ferromagnetic Josephson junctions for memory applications. *IEEE Trans. Appl. Supercond.* **28**, 1800606 (2018).

[12] Baek, B., Rippard, W. H., Benz, S. P., Russek, S. E. & Dresselhaus, P. D. Hybrid superconducting-magnetic memory device using competing order parameters. *Nat. Commun.* **5**, 3888 (2014).

[13] Golod, T., Iovan, A. & Krasnov, V. M. Single Abrikosov vortices as quantized information bits. *Nat. Commun.* **6**, 8628 (2015).

[14] Dayton, I. M. *et al.* Experimental demonstration of a Josephson magnetic memory cell with a programmable π-junction. *IEEE Magn. Lett.* **9** (2018).

[15] Nevirkovets, I. P. & Mukhanov, O. A. Memory cell for high-density arrays based on a multiterminal superconducting-ferromagnetic device. *Phys. Rev. Applied* **10**, 034013 (2018).

[16] Niedzielski, B. M. *et al.* Spin-valve Josephson junctions for cryogenic memory. *Phys. Rev. B* **97**, 024517 (2018).

[17] Madden, A. E., Willard, J. C., Loloee, R. & Birge, N. O. Phase controllable Josephson junctions for cryogenic memory. *Supercond. Sci. Technol.* **32**, 015001 (2018).

[18] Satchell, N. *et al.* Spin-valve Josephson junctions with perpendicular magnetic anisotropy for cryogenic memory. *Appl. Phys. Lett.* **116**, 022601 (2020).

[19] Martinez, W. M., Pratt, W. P. & Birge, N. O. Amplitude Control of the Spin-Triplet Supercurrent in S/F/S Josephson Junctions. *Phys. Rev. Lett.* **116**, 1–5 (2016).

[20] Glick, J. A. *et al.* Phase control in a spin-triplet SQUID. *Sci. Adv.* **4**, 1–8 (2018).

[21] de Andrés Prada, R. *et al.* Memory-functionality superconductor/ferromagnet/superconductor junctions based on the high-T_c cuprate superconductors $YBa_2Cu_3O_{7-x}$ and the colossal magnetoresistive manganite ferromagnets $La_{2/3}X_{1/3}MnO_{3+\delta}$(X=Ca,Sr). *Phys. Rev. B* **99**, 214510 (2019).

[22] Weigand, M. *et al.* Vortex core switching by coherent excitation with single in-plane magnetic field pulses. *Phys. Rev. Lett.* **102**, 077201 (2009).

[23] Uhlíř, V. *et al.* Dynamic switching of the spin circulation in tapered magnetic nanodisks. *Nat. Nanotechnol.* **8**, 341–346 (2013).

[24] Kammerer, M. *et al.* Magnetic vortex core reversal by excitation of spin waves. *Nat. Commun.* **2**, 279 (2011).

[25] Linder, J. & Robinson, J. W. A. Superconducting spintronics. *Nat Phys* **11**, 307–315 (2015).

[26] Eschrig, M. & Löfwander, T. Triplet supercurrents in clean and disordered half-metallic ferromagnets. *Nat. Phys.* **4**, 138–143 (2008).

[27] Yang, G., Ciccarelli, C. & Robinson, J. W. A. Boosting spintronics with superconductivity. *APL Mater.* **9**, 050703 (2021).

[28] Song, X. *et al.* Strain-mediated voltage-controlled magnetic double-vortex states in elliptical nanostructures. *J. Magn. Magn. Mater.* **547**, 168729 (2022).

[29] Vansteenkiste, A. *et al.* The design and verification of MuMax3. *AIP Adv.* **4**, 107133 (2014).

[30] Lahabi, K. *et al.* Controlling supercurrents and their spatial distribution in ferromagnets. *Nat. Commun.* **8**, 2056 (2017).

STRONGLY CORRELATED RUTHENIUM OXIDE MICROSTRUCTURES

3

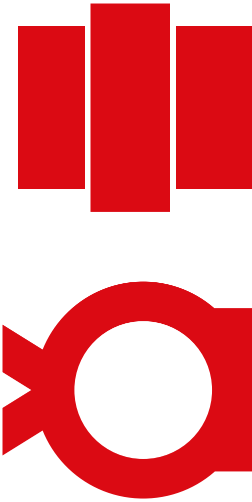

6

UNIVERSAL SIZE-DEPENDENT NONLINEAR CHARGE TRANSPORT IN SINGLE CRYSTALS OF THE MOTT INSULATOR Ca_2RuO_4

R. Fermin*, G. Avallone*, K. Lahabi, V. Granata, R. Fittipaldi, C. Cirillo, C. Attanasio, A. Vecchione & J. Aarts

The surprisingly low current density required for inducing the insulator-to-metal transition has made Ca_2RuO_4 *an attractive candidate material for developing Mott-based electronics devices. However, the mechanism driving the resistive switching remains a controversial topic in the field of strongly correlated electron systems. In this chapter, we probe an uncovered region of phase space by studying high-purity* Ca_2RuO_4 *single crystals, using the sample size as the principal tuning parameter. Upon reducing the crystal size, we find a four orders of magnitude increase in the current density required for driving* Ca_2RuO_4 *out of the insulating state into a non-equilibrium (also called metastable) phase, which is the precursor to the fully metallic phase. By integrating a microscopic platinum thermometer and performing thermal simulations, we gain insight into the local temperature during simultaneous application of current and establish that the size dependence is not a result of Joule heating. The findings suggest an inhomogeneous current distribution in the nominally homogeneous crystal. Our study calls for a reexamination of the interplay between sample size, charge current, and temperature in driving* Ca_2RuO_4 *towards the Mott insulator-to-metal transition.*

This chapter is based on the paper published in *npj Quantum Materials* **6**, 91 (2021).

*These authors contributed equally to this study

6.1. INTRODUCTION

The 4*d* electron Mott insulator Ca_2RuO_4[1] has become the subject of intense research in recent years due to its intriguing electrical [2, 3, 3–14] and magnetic properties[15, 16]. These range from a paramagnetic insulating phase at room temperature to ferromagnetism below 30 K under applied pressure[3], and a superconducting transition at ~0.4 K[2]. However, its most remarkable feature is arguably its current-driven insulator-to-metal transition (IMT) which occurs at unusually low electric field or current density thresholds (~ 40 V/cm or few A/cm^2 respectively)[17, 18]. This is in contrast to previous reports on Mott insulators, where the IMT is limited to low temperatures and/or to the application of high E-fields[19, 20]. The capacity to switch between resistive states at room temperature is a desirable property to realize current switchable memories, neuromorphic devices, and next-generation oxide electronics[21, 22].

The underlying mechanism responsible for such low current densities is still a topic of intense debate, as the driving force behind the IMT is not limited by the application of current. Due to its high resistivity in the insulating state, Joule heating plays a sig-

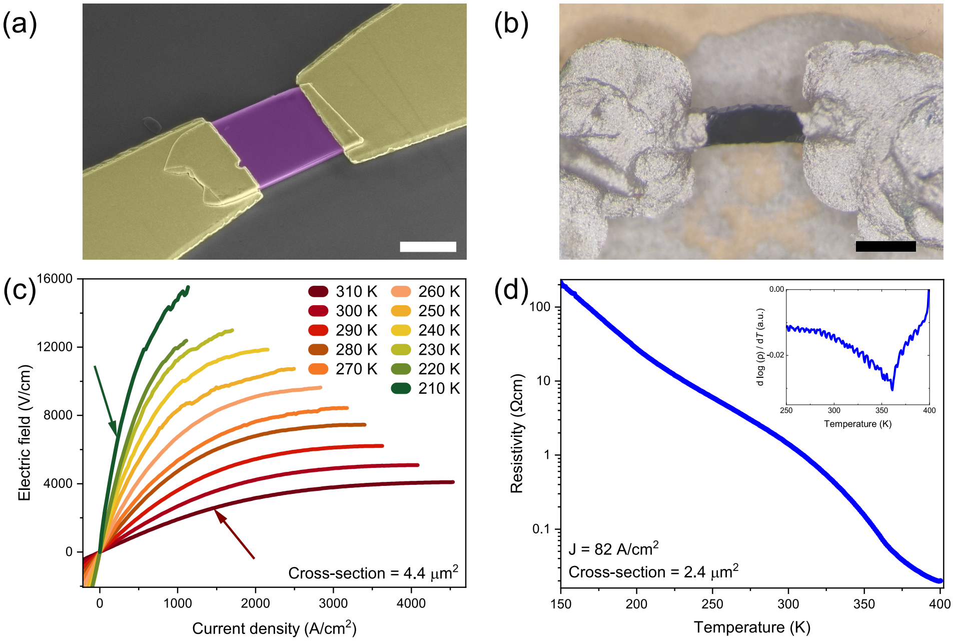

Figure 6.1: (a) Displays a false colored scanning electron micrograph of a microscopic sample (in purple) that is contacted by yellow colored Ti/Au contacts. The scale bar represents 0.3 µm. (b) Shows an optical microscope image of an mm-sized sample, where the scale bar measures 500 µm. Panel (c) shows JE-characteristics acquired on a microscopic sample at different temperatures. The arrows indicate the current density that corresponds to the Figure of Merit. Note that these curves are obtained below the IMT. The resistivity versus temperature of a typical microscopic sample is shown in panel (d). In the microscopic size range, we do not observe a sharp temperature-induced IMT. However, as indicated by the inset (the derivative of the curve in the main Figure), there is a clear inflection point indicating the thermal transition.

nificant role since the IMT can also be thermally driven by heating the crystal above 357 K[8]. This has led to ambiguity about the origin of the IMT, and whether it is thermally or electronically driven, as evident by the large number of works discussing local heating[7, 18, 23–27]. Specifically, in a recent work, it was found that the IMT is always accompanied by a local temperature increase to the transition temperature[23]. Moreover, as a precursor to the metallic phase, a third and non-equilibrium (also called metastable) phase has been detected by X-ray, neutron diffraction experiments, and additionally with Raman spectroscopy[4–6]. This non-equilibrium phase seems to be induced by low current densities, but its role in the current-driven IMT remains elusive. Another major hurdle is the pronounced structural transition accompanying the IMT, in which the RuO_2 octahedra are elongated, and the unit cell is transformed from orthorhombic to tetragonal[3–5, 7, 17, 28, 29]. This transition leads to a strong temperature dependence of the unit cell volume (~1% between 100 K and 400 K), introducing large internal strains in the crystal, often resulting in the formation of cracks or even shattering the crystal upon reentering the insulating phase[28].

Although it is much debated whether the IMT is primarily triggered by Joule heating or driven by electronic effects, a parameter that has been left unexplored in this discussion is the size of the samples. Decreasing the size of bulk samples down to µm range gives considerably more control over current paths in the crystal (due to the uniform rectangular cross section). Furthermore, micro cracks and step-like terraced edges, which occur naturally in mm-sized bulk crystals, are scarce in microscopic samples. Also, since the voltage contacts cover the entire side of the microscopic samples, the current injection is more homogeneous. This contrasts with mm-sized crystals where point contacts, and their entailing current crowding effects, are more common. Finally, the microscopic samples are expected to be less susceptible to thermal gradients and heating effects due to the enhancement of the surface-to-volume ratio and the direct contact with an isothermal substrate.

In this chapter, we carry out an extensive size-dependent study using a large number (39) of ultra-pure single crystal samples of Ca_2RuO_4, ranging between the hundreds of nm and the millimeter scale. We examine the role of the current density in inducing the non-equilibrium phase, which we can probe reversibly (i.e., without inducing the IMT and consequently damaging or altering the crystal). Upon decreasing the cross section, we find a dramatic enhancement of the required current density by at least four orders of magnitude. Furthermore, by integrating a micrometer-sized platinum thermometer, we are able to directly probe the local temperature of the microscopic samples, and demonstrate that the pronounced size dependence is not caused by thermal effects. Our findings call for a careful reexamination of the relevant mechanism behind the non-equilibrium phase and its relation to the IMT in Ca_2RuO_4.

6.2. CHARACTERIZING MICROSCOPIC SAMPLES

To examine the crossover from mm-sized bulk behavior to the microscopic one, we have produced samples of varying cross section between 0.5 mm^2 and 0.5 µm^2. The microscopic samples were fabricated using mechanical exfoliation[30, 31]. This enables us to produce micron-sized "crystal flakes," which can be lithographically contacted for electrical transport measurements without compromising the material quality. In addition to the microscopic samples, we have fabricated mm-sized bulk samples that are hand-contacted by using silver paint. We employed a focused Ga^+-ion beam (FIB) to control the cross section systematically. Figures 6.1a and 6.1b show scanning electron microscope and optical microscope images of samples in microscopic and mm-sized ranges, respectively. In Appendix A the sample fabrication is further detailed.

All measurements are carried out by biasing a current in the ab-plane rather than a voltage since inducing the metallic state by applying an electric field is more abrupt, and therefore the crystals are more likely to break. Furthermore, the current density as a function of electric field is hysteretic, complicating the study of size effects. We have conducted electric field versus current density (JE-characteristic) and resistivity as a function of temperature measurements and found that the microscopic samples qualitatively show similar behavior as the mm-sized bulk samples[4]. Typical results obtained on microscopic samples are summarized in Figures 6.1c and 6.1d. It is important to note that, despite several orders of magnitude of size variation, we find the room temperature resistivity of all our samples (microscopic and mm-sized bulk) to be comparable and in good agreement with the literature values[1]. Curiously, however, the temperature-induced IMT is broadened in microscopic samples with respect to those observed in mm-sized bulk samples (see Figure 6.1d). We attribute the broadening of the transition to the small sample thickness since similar effects are observed in thin film samples[32–35]. We did observe an abrupt change in resistivity upon cooling a relatively thick (0.5 µm) microscopic sample through the metal to insulator transition for further discussion on this aspect the reader is referred to Appendix B.

6.3. COMPARING SAMPLES OF DIFFERENT CROSS SECTION

Figure 6.1c shows JE-characteristics obtained on a microscopic sample at different temperatures. These curves qualitatively show similar behavior as the mm-sized bulk samples. However, the current density required for triggering the metastable phase, which is indicated by a negative $\mathrm{d}E/\mathrm{d}J$ as a function of J, exceeds the literature values (for mm-sized crystals) by at least four orders of magnitude[7, 17, 23]. This is demonstrated in Figure 6.2, where we plot the differential resistivity $\mathrm{d}E/\mathrm{d}J$ as a function of J for selected samples. The current density at which $\mathrm{d}E/\mathrm{d}J$ begins to decline, corresponding to nonlinear conduction, increases if the sample size is reduced to microscopic scales. In order to compare the nonlinear conduction under applied current between different samples in a systematic manner, we propose a Figure of Merit (FOM) that can be applied to samples of different sizes. First, differential resistivity versus current density curves are computed by analytically differentiating the JE-characteristics (upper panel of Figure 6.2). The curves are then normalized to their low current value (i.e., currents for which the resistivity is current independent; the lower panel of Figure 6.2). Next, we choose the current density at which the slope of the JE-curve has halved as our Figure of Merit, called the 50%-slope current density. The choice for this FOM is suitable since we can compare the size dependence of the JE-characteristics in a regime where heating effects play a relatively unimportant role. Furthermore, at the FOM current density, the metallic phase is not yet induced in the sample[4]. However, the shape of the JE-curves is the same between all measured samples. This means that the current density at which the metallic phase is induced scales with the FOM. Therefore, the FOM allows us to make a prediction of the metastable and metallic phases. Lastly, the slope of the differential resistivity appears to be maximal at the FOM. Therefore, the choice of this FOM leads to a small uncertainty in the estimated current density, which is not the case when using the current density at the maximum E-field, for

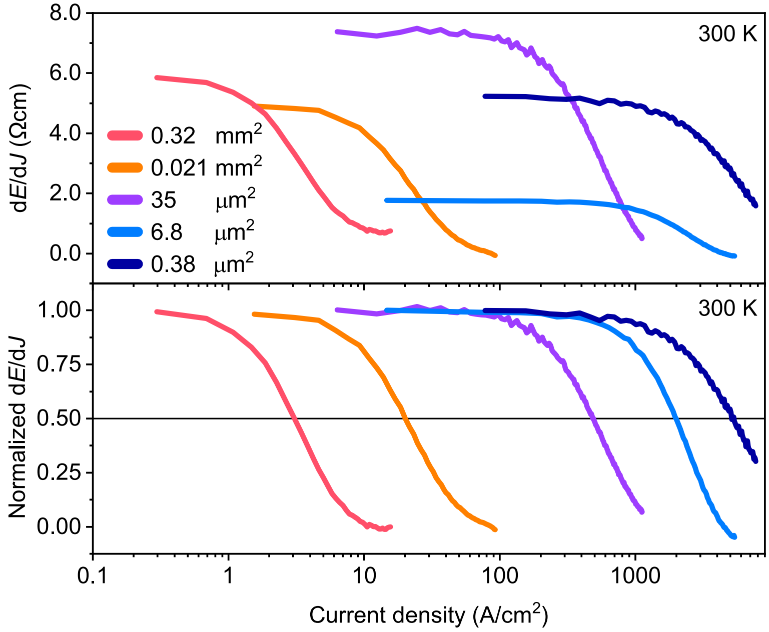

Figure 6.2: The top panel shows the differential resistivity dE/dJ as a function of current density of a few selected samples at room temperature. The legend shows the cross-sectional area of these samples. For all microscopic and mm-sized bulk samples, the low current resistivity at room temperature corresponds to the literature values. In the lower panel, the differential resistivity of these samples is normalized with respect to the low current resistivity (i.e., where the resistivity is current independent). Even though the JE-characteristics of all samples are qualitatively the same, the current density scale at which they exhibit nonlinear conduction differs orders of magnitude. The current density at which the slope of the JE-characteristic is halved is chosen as the Figure of Merit (FOM). We show the FOM by the horizontal reference line in the lower panel.

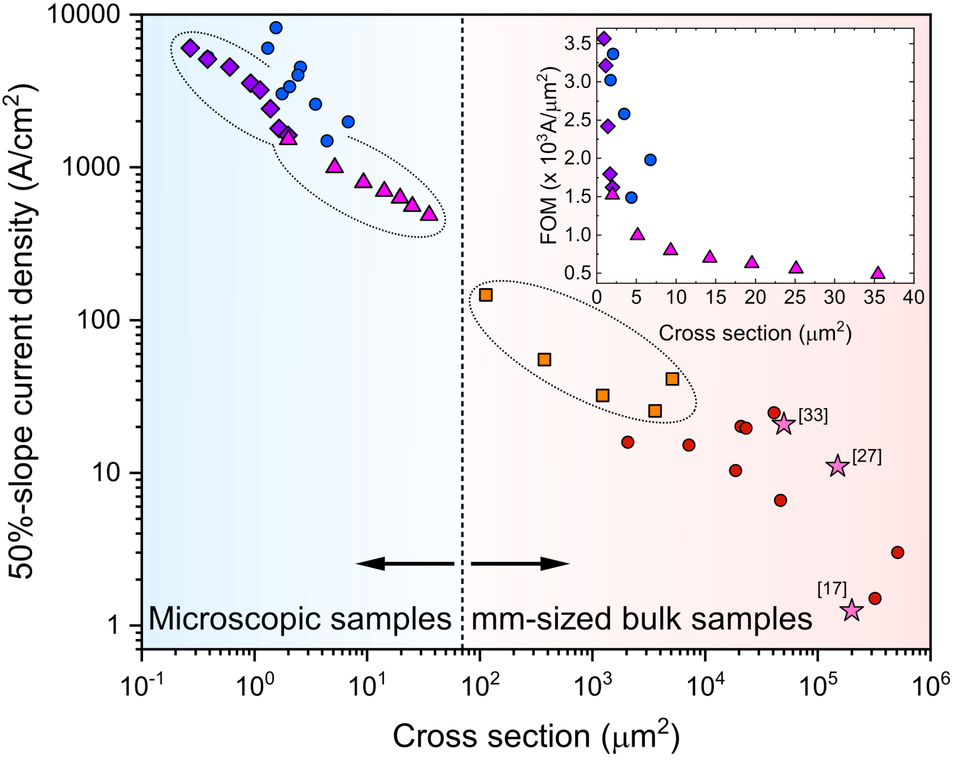

Figure 6.3: The FOM as a function of cross-sectional area for all measured samples at room temperature on a log-log scale. N.B. each data point corresponds to a single sample. The thinning study samples are depicted with a unique non-circular symbol and a different color. The inset displays the FOM vs sample cross section for selected samples on linear scales. The star-symbols correspond to the FOM extracted from literature; the label indicates the reference number.

instance.

Figure 6.3 displays the FOM as a function of the sample cross section for all measured samples. The current density required for nonlinear conduction grows monotonically with decreasing sample dimensions, and the FOM shows a power law dependence on the cross-sectional area. To exclude any potential artifacts associated with sample preparation, we performed a thinning study on three samples over an extensive size range. We incrementally modify the width and thickness of the same crystal through consecutive FIB structuring steps and measure the JE-characteristic, after each one. Following this procedure, we changed the width of a single microscopic sample during up to seven different thinning steps. Moreover, in an mm-sized bulk sample, we decreased the sample width by a factor of 50. Samples on which a thinning experiment is carried out are encircled and highlighted in Figure 6.3 by a non-circular symbol and a different color. Scanning electron micrographs of these samples are shown in Figure 6.4. The FOM as a function of only the width or thickness of the sample (see Appendix

C) reveals the size dependence is not exclusively formed by any of these two parameters but is instead a combination between them, which means that neither of these dimensions is more significant in determining the transport properties of the crystal. The cross section is the most straightforward combination of the two parameters, which is chosen in Figure 6.3.

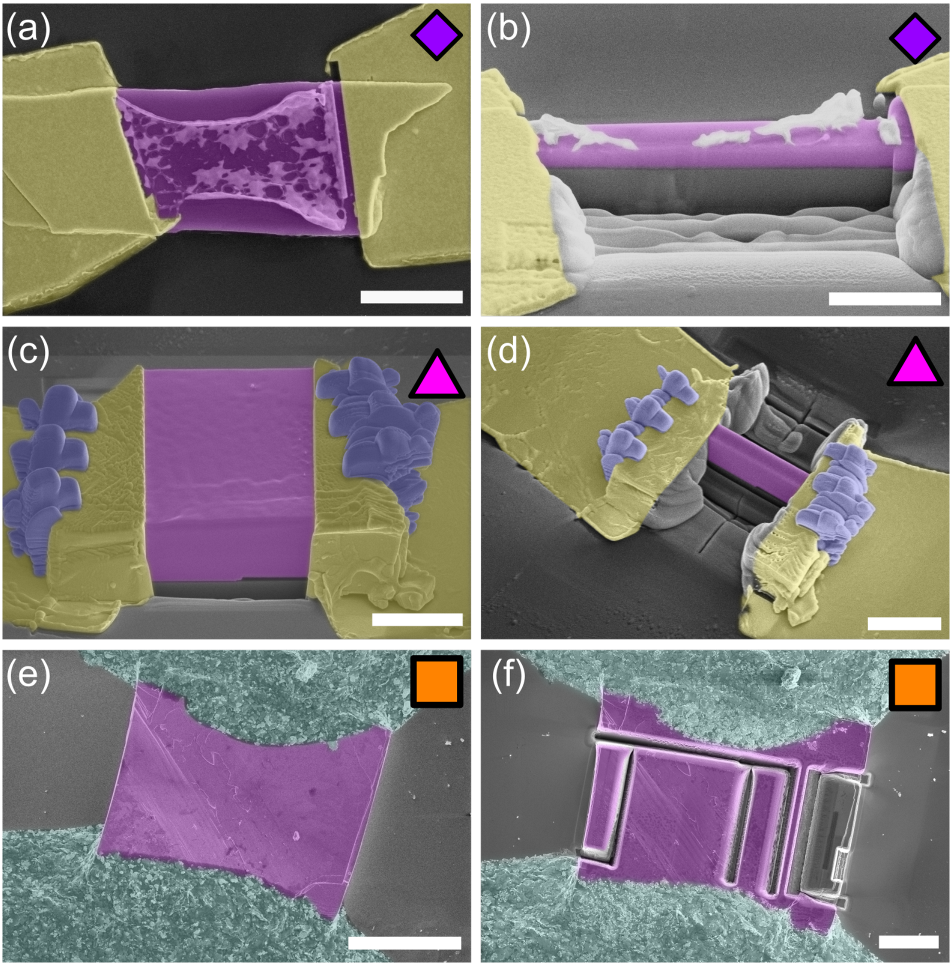

Figure 6.4: False colored scanning electron micrographs of samples used for the thinning experiment in different stages of thinning. In all images, purple indicates the crystal, and yellow indicates titanium/gold contacts to the sample. (a) and (b) correspond to the sample indicated by diamond signs in Figure 6.3. It covers the smallest size ranges; the scale bars correspond to 3 µm and 2 µm, respectively. Some lithography resist residue can be observed in white. The sample depicted in (c) and (d) covers the intermediate sizes (scale bars are respectively 4 µm and 5 µm long) and is represented by triangles in 6.3. Indicated in blue is the electron beam induced deposited tungsten used to strengthen the contacts to the crystal. The third sample of the thinning study is shown in images (e) and (f). It is a relatively small mm-sized bulk sample contacted using silver epoxy (false colored in light blue). Orange squares depict the FOM data of this sample in 6.3. The scale bars in these images represent 100 µm and 50 µm, respectively.

Despite the clear trend in Figure 6.3, there is a sample-to-sample variation that cannot be explained by the uncertainty in the measured crystal dimensions. The deviation from the trend in the mm-sized samples can be explained by irregular current paths in the sample and inconstant cross-sectional area throughout the length of the sample. For the microscopic samples, this does not hold. However, the ratio between width and thickness differs among the samples, and therefore they are expected to respond differently to decreasing dimensions if surface layer effects are important. Furthermore, oxygen relocation can modify the crystal structure when passing a current, resulting in a change of transport properties between current cycles. This is consistent with our observations, where, in some cases, the JE-characteristic slightly changes after different current or temperature cycles. These arguments explain the increased spread observed in Figure 6.3.

6.4. THE ROLE OF TEMPERATURE

Measuring the local sample temperature proved to be vital in many proceeding studies[7, 18, 23–27]. These experiments, where the temperature is locally measured in Ca_2RuO_4, are carried out on mm-sized bulk samples using optical techniques, as local contact thermometry is experimentally challenging to realize at these dimensions. On the other hand, microscopic samples do not have this limitation and enable contact thermometry to give insight into the local sample temperature. This section describes measurements acquired using such a thermometer, accompanied by thermal simulations.

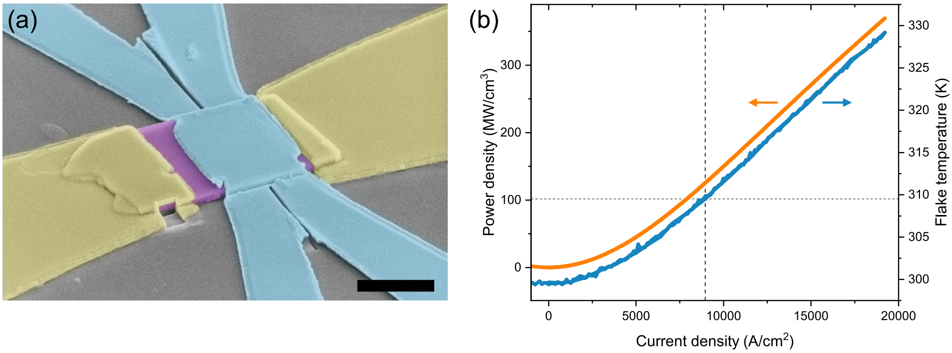

Figure 6.5: (a) Displays a false colored scanning electron micrograph of a microscopic sample (purple) with, in blue, the embedded Pt-thermometer, which can be employed to locally measure the temperature. The yellow parts are the Ti/Au contacts. This is the same sample as depicted in Figure 6.1a; it has a cross-sectional area of 1.6 μm^2 and the scale bar represents 3 µm. (b) displays the measured power density calculated by multiplying the current density by the electric field, depicted with the measured local sample temperature. There is a one-to-one correspondence of the local temperature to the power density, indicating that the temperature increase is due to Joule heating. The dissipated power is used as input data for the simulations (see section 6.4.2).

6.4.1. MICRO-SCALE THERMOMETRY

We designed and fabricated a platinum thermometer on top of selected microscopic samples. Since platinum has a linear temperature dependence, we can accurately measure the temperature of the microscopic samples while simultaneously driving a current using an independent bias. The full details on the fabrication of the Pt-thermometer are provided in Appendix A. Figure 6.5a shows a false colored scanning electron micrograph of the same sample depicted in Figure 6.1a, after the deposition of the Pt-thermometer. We calculate the power density dissipated in the sample by multiplying the measured electric field by the applied current density. In Figure 6.5b, we plot this quantity along with the measured local sample temperature. The shapes of the two curves match closely, which gives a strong indication that we are measuring the temperature increase caused by Joule heating. Note that at the FOM current density, the locally measured temperature increase is less than 10 K. Therefore, we conclude that Joule heating is non-zero but similar to mm-sized bulk samples[23].

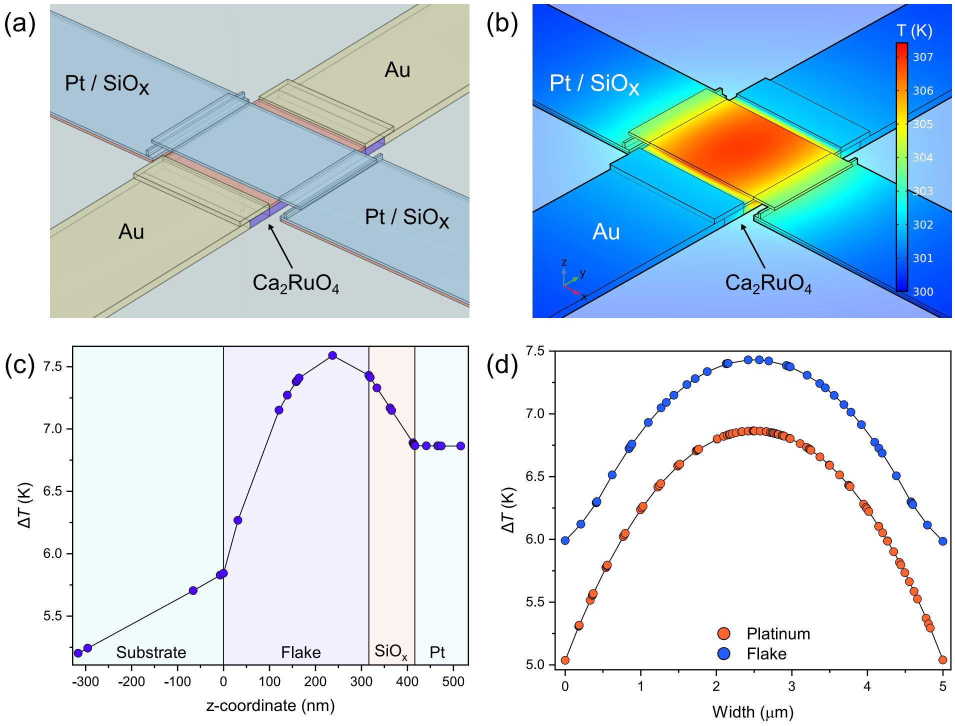

Figure 6.6: (a) Shows a schematic overview of the different elements simulated. Each color corresponds to the labeled material. In (b) the simulated surface temperature heatmap of the sample in (a) is depicted. (c) depicts the temperature increase $\Delta T = T_{\text{flake}} - 300$ K along a vertical line cut through the center of the substrate, flake and thermometer. The different parts of the sample are labeled by the same colors as in (a). The simulated temperature along a horizontal line parallel to the Pt-thermometer leads is displayed in (d). The temperature in **a,b** and (c) is evaluated at the FOM current density.

6.4.2. COMSOL SIMULATIONS

In order to verify that the temperature difference between the Pt-thermometer and the sample is negligible and to investigate the likelihood of any potential temperature gradients in the sample, we have performed thermal simulations supporting the thermometry results. We consider the geometry displayed in Figure 6.6a, which is a true-to-size model of the sample shown in Figure 6.5a. We solve for a steady-state temperature under the assumption that heat is generated uniformly in the part of the crystal between the gold contacts (i.e., not in the parts covered by gold), while the substrate temperature remains constant, 50 µm away from the sample. As input power, we use the measured power density displayed in Figure 6.5b. The temperature equilibrium is governed by the thermal conductivity of the materials, which Terasaki et al. have evaluated for Ca_2RuO_4 to be 5.1 W/mK and 1.8 W/mK for in- and out-of-ab-plane, respectively[26]. The resulting surface temperature distribution is shown in Figure 6.6b.

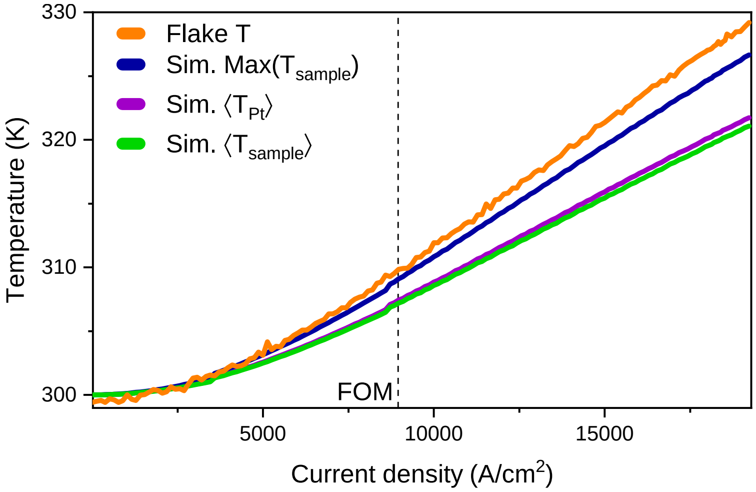

Figure 6.7: The local measured Pt temperature compared to multiple simulated temperatures as a function of the applied J. The data is acquired on the sample depicted in Figure 6.5a. The substrate temperature is 300 K, and The vertical reference line indicates the FOM. The simulated average sample (green curve) and Pt temperature (purple curve) correspond to a high degree, which leads to the conclusion that the Pt-thermometry technique is suited for establishing the sample temperature. The difference between the measured and simulated temperature can be caused by the absence of heat transfer barriers in the simulations.

Figure 6.6c and 6.6d show the temperature variations within the sample at the FOM current density. Here, the temperature increase is plotted as a function of a vertical and horizontal line cut, respectively. The temperature increases roughly quadratically from the sides of the crystal towards the hottest point of the flake. The temperature variations in the flake were found to be lower than 3 K at the FOM current density.

In Figure 6.7 we compare the platinum thermometry data to the simulation results. The measured temperature (orange) exceeds the expected averaged Pt temperature (purple). This can be caused by the absence of heat transfer barriers between the simulated elements. On the other hand, these can be expected in experiments. The purple curve can therefore be considered a lower bound of the expected Pt temperature. Nevertheless, the simulated average sample (green) and Pt temperature (purple) show correspondence to a high degree. We also evaluate the maximum temperature within the simulated flake geometry (blue curve) and compare it to the simulated average Pt temperature, which we find to differ less than 2 K at the FOM current density. Therefore, we consider our Pt thermometry technique suited for acquiring the average sample temperature at the FOM.

6.4.3. CONSEQUENCES OF HEATING

The measurement of the local temperature enables us to calculate what the JE-characteristic would look like based on heating effects only. For the resistivity versus temperature measurement on this sample, we compute the $\mathrm{d}E/\mathrm{d}J$ from our JE-characteristics for low currents (i.e., where the resistivity ρ is current independent):

$$\rho(T) = \frac{\mathrm{d}E}{\mathrm{d}J}(T, J \approx 0) \tag{6.1}$$

Since the temperature is homogeneous up to a variation of 3 K over the entire sample, we can use the locally measured temperature as a function of current density to find the $\mathrm{d}E/\mathrm{d}J$ as a function of heating effects:

$$\frac{\mathrm{d}E_{\text{thermal}}}{\mathrm{d}J}(J) = \frac{\mathrm{d}E}{\mathrm{d}J}(T(J), J \approx 0) = \rho(T(J)) \tag{6.2}$$

Integrating the equation (6.2), we can reconstruct the JE-characteristic that would result, if Joule heating would be the only mechanism causing nonlinear conduction. We set the integration constant by requiring zero electric field for zero current density ($E(0) = 0$; see Appendix D for more details):

$$E_{\text{thermal}}(J) = \int \frac{\mathrm{d}E_{\text{thermal}}}{\mathrm{d}J}(J)\mathrm{d}J \tag{6.3}$$

We denote this reconstructed function as $E_{\text{thermal}}(J)$ and plot it alongside the measured data in Figure 6.8a. Even at low current densities, the actual measured data shows stronger nonlinear conduction than $E_{\mathrm{thermal}}(J)$, indicating that current-driven effects are significant in the microscopic samples for all applied current densities probed in this study.

Alternatively, the differential resistivity as a function of local sample temperature is plotted in Figure 6.8b. The purple curve describes the resistivity as a function of temperature with a constant current density (62 A/cm^2). Alongside, we plot the differential resistivity as a function of increasing bias current while maintaining a constant substrate temperature. The slope decrease of JE-characteristic, caused by the application of current, is not exclusively driven by Joule heating.

Based on our simulations and thermometry experiments, we conclude that the size dependence presented in Figure 6.3 cannot be explained by Joule heating. Furthermore, we find that a current-driven mechanism is present parallel to heating effects in the non-equilibrium phase.

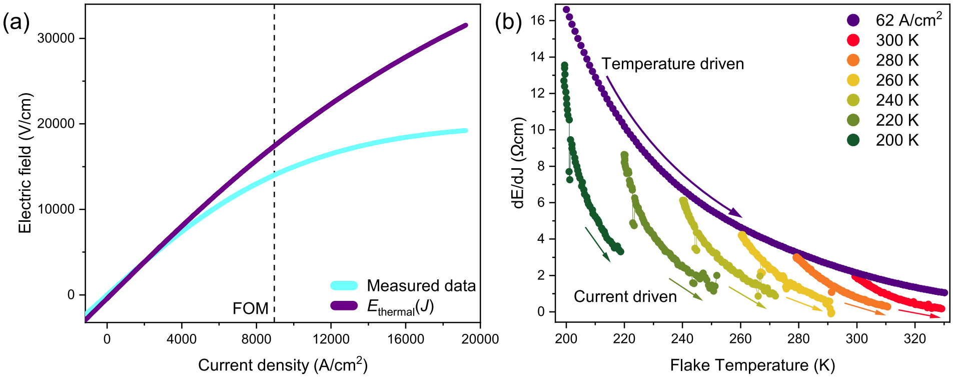

Figure 6.8: (a) shows the electric field acquired simultaneously with the temperature measurement of Figure 6.5. The measured data is compared to E_{thermal}, which is the calculated electric field on basis of Joule heating only. The vertical reference line indicates the FOM. Alternatively, (b) displays the differential resistivity as a function of the flake temperature. Either the substrate temperature (purple) or the current density is changed. At all current densities, the nonlinear conduction is stronger than heating effects can provide.

6.5. DISCUSSION

Before discussing the possible origin of the observed size dependence, we consider the following notes. Firstly, there seems to be no intrinsic length scale found in our measurements. This can be seen from the absence of a specific cross section where the FOM changes discontinuously. Secondly, we can exclude the effects of microcracks since the size dependence continues even in the microscopic regime where micro cracks are not present. By inspecting the samples with a scanning electron microscope, we could confirm that no micro cracks were induced by measuring the JE-characteristic. Thirdly, Jenni et al. observed a similar current-driven mechanism parallel to Joule heating, as is reported here[24]. Lastly, we note that our findings are consistent with the reports on epitaxially grown thin films of Ca_2RuO_4, where the current density required to induce the IMT was also found to be many orders of magnitude higher than in bulk literature values[32].

The emergence of the metallic phase was recently attributed by Terasaki et al[26]. to energy flow, as opposed to charge transport. In this study, the energy flow corresponds to the dissipated power (product of current and voltage IV). In contrast, it is more insightful to describe the product of electric field and current density EJ (power dissipation density), enabling the comparison of samples of different length scales. Since microscopic samples show a four order of magnitude increase in current density at which we observe nonlinear transport, we find that the power dissipation density is eight orders of magnitude larger in microscopic samples than in mm-sized bulk samples (see Figure 6.5a). Therefore, it is unlikely that the energy flux through the crystal is responsible for the observed size dependence.

Alternatively, strain, induced through coupling to the substrate, might explain the size dependence. In the zero-current limit, however, the substrate does not exercise any strain on the crystal, as we will discuss below. The room temperature resistivity of Ca_2RuO_4 strongly depends on strain, and the IMT can be induced by applying 0.5 GPa of pressure[3, 13, 14]. By using ultra-low currents (∽nA), we have confirmed that the insulating-state resistivity of the microscopic samples matches that of their mm-sized counterparts, signaling the absence of strain. Moreover, as discussed in Chapter 7, we have prepared microscopic samples using equal methods and substrates on isostructural Sr_2RuO_4. These samples retained bulk properties to sizes below 200 nm, whereas, like Ca_2RuO_4, its transport properties depend heavily on strain[36–38]. Therefore, we conclude that our microscopic samples do not experience strain at zero current bias. In simultaneous transport and X-ray diffraction measurements, it has been shown that there is no detectable change of the lattice parameters at the FOM current density[4]. Combined with the absence of strain at zero current bias, this leads to the conclusion that our samples do not experience any strain at the FOM, regardless of their size. Thus, we do not regard strain as a plausible explanation for the observed size dependence.

Near the IMT, independent of whether it is induced by current or temperature, the arguments supporting the absence of strain no longer hold, as the lattice constants significantly alter[4, 5]. Although we are far below the IMT in our current-driven experiments, we pass the IMT in the temperature sweep, presented in Figure 6.1d. Strain-related effects could be responsible for the observed broadening of the transition. Moreover, a broadened transition is commonly observed in thin films, where strain induced by the substrate is expected to be an influential parameter[32–34].

Finally, an inhomogeneous current distribution throughout the cross-sectional area could potentially explain the size dependence. Since the current density is calculated by dividing the applied current by the entire cross section, the *apparent current den-*

sity in mm-sized bulk samples might be lower than the *actual current density,* which is physically relevant. When sample dimensions are reduced, however, the apparent and actual current densities can be more similar, and therefore we might measure an increase in apparent current density.

Metallic filament formation, known to occur in Mott insulators, can be the origin of such highly inhomogeneous current distributions[39]. Contrarily, for Ca_2RuO_4, Zhang et al. inspected phase separation using scanning near field optical microscopy (SNOM) and found a ripple pattern at the phase boundary between the insulating and metallic states[7]. Although the resolution of the SNOM technique might be insufficient to rule out sub 100 nm channel formation, it is difficult to reconcile the striped pattern found in SNOM with filament formation at present.

On the other hand, Zhang et al. find that the metallic phase nucleates at the top of the sample, and its depth increases when traversing a phase boundary in the phase-separated state. This could suggest an inhomogeneous current distribution throughout the cross-sectional area (high at the edges of the crystal and decreasing towards the center of the bulk). Since the microscopic crystals have a larger surface-to-volume ratio, the edges are relatively more dominant. If the current density gradually increases below the current-carrying surface, this proposed mechanism will not feature any length scale at which a discontinuous change is expected in the FOM, which is compatible with our findings. In Appendix E, a minimal toy model describing the inhomogeneous current density is presented. This model can reproduce the power law dependence observed in Figure 6.3.

6.6. CONCLUSION

In conclusion, we have performed a detailed study on the size-dependent electrical properties of the Mott insulator Ca_2RuO_4. We find a surprising relation between crystal size and the current density at which nonlinear conduction occurs, which increases four orders of magnitude when the sample size is reduced from 0.5 mm^2 to 0.5 μm^2. We have strong indications that the observed size dependence is not caused by Joule heating, using a local Pt-thermometer fabricated on top of selected microscopic samples. Our findings indicate an intrinsically inhomogeneous current density distribution in single crystals of Ca_2RuO_4. This calls for a reexamination of the relevant role of charge current in the metastable phase and its possible relation to the IMT. As an outlook, the combination of microscopic samples with a well-controlled current path, and local platinum temperature probes, provides a state-of-the-art approach to study the interplay between thermal and electronic effects, which can be used to study the IMT in Mott insulators.

APPENDICES

A. CRYSTAL GROWTH AND SAMPLE FABRICATION

Bulk single crystals of Ca_2RuO_4 were grown using a flux-feeding floating zone technique with Ru self-flux using a commercial image furnace equipped with double elliptical mirrors. Several techniques, including X-ray diffraction, energy dispersive spectroscopy, and polarized light optical microscopy analysis, have been used to fully characterize the structure, quality, and purity of the crystals. See references [40] and [41] for further details.

The microscopic samples were fabricated using mechanical exfoliation on highly resistive $SrTiO_3$ or sapphire substrates[31]. The flake samples are significantly thicker than monolayers. Therefore, random strain patterns, wrinkles, and folds associated with the thin film limit are absent. Due to the natural shape of the crystal flakes, the produced samples are suited best for passing current in the ab-plane. Therefore all experiments are carried out in this configuration.

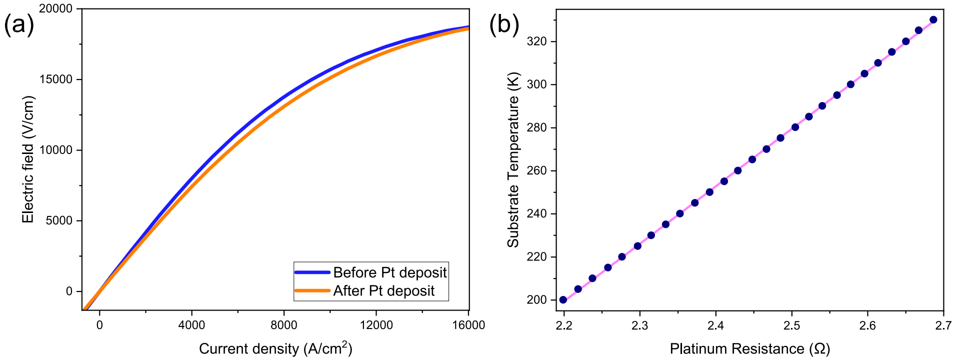

Figure A.1: (a) Displays the JE-characteristic before and after the deposition of the Pt-thermometer on the sample depicted in Figure 6.5a. In (b) the calibration curve of the Pt-thermometer, which is fitted by a linear curve, is shown. The slope of the fit corresponds to 0.27 K per mΩ. This enables sub-Kelvin precision thermometry.

Considerable effort is put into the fabrication of the electrical connections on the samples to reduce the contact resistance that possibly becomes an extrinsic origin for nonlinear conduction due to local Joule heating. In order to perform electrical transport measurements, the samples obtained by the exfoliation process were contacted using electron beam lithography designed and sputter-deposited Ti/Au contacts. When necessary, we used electron beam induced deposition to provide an electrical reinforcement of the contacts by locally depositing an additional layer of tungsten-carbide on them. In addition to the microscopic samples, we have fabricated conventionally mm-sized bulk samples that are contacted by hand using silver paint (Agar Scientific G3691). On the mm-sized samples, we found a resistive background in the JE-characteristics, from which we extracted the contact resistance to be less than 10

Ω, which is significantly smaller than the sample resistance, supporting the use of a two-probe measurement. In addition, some microscopic samples were contacted in a 4-probe geometry. Using these samples, we could confirm that the contact resistance is negligible compared to the sample resistance.

We used the FIB technique to modify the sample width and thickness, enabling full control of sample dimensions and geometry over an extensive crystal size range. An often-heard criticism of FIB processing is the implantation of Ga-ions and damage induced to the crystal due to the high impulse of the ions. The key to resolving these issues is the combination of ultra-low beam currents and an SiO_x capping layer. The first ensures that the damages are only very local (approximately 30 nm from the edge of the milled structure), and the second protects the top side of the crystal during the inevitable radiation of Ga-ions.

The Pt-thermometer is added to selected samples in a second step of electron beam lithography. The Pt-circuit is electrically isolated by a thin layer of sputter-deposited SiO_x (~ 100 nm). This ensures that the Pt-thermometer and sample form two decoupled electrical systems. The resistance between the Pt-circuit and the Ca_2RuO_4 crystal is over 1 GΩ. Besides, the application of the thermometer does not affect the JE-characteristic (see Figure A.1a). The thickness of the SiO_x layer is optimized, providing a disconnected electrical system from the crystal while remaining in thermal contact to provide sub-Kelvin measurement precision. The material of choice for the thermometer circuit is platinum since its resistivity is highly linear over the temperature range at which we carry out our experiments, as seen in the thermometer calibration curve of Figure A.1b. The resistance of the Pt-thermometer changes by 0.27 K/mΩ.

B. ABRUPT TRANSITION IN A RELATIVELY THICK MICROSCOPIC SAMPLE

In most of the microscopic samples, the temperature-driven IMT is broadened. Figure 6.1d shows the general resistivity versus temperature behavior of microscopic samples. However, on one of our microscopic samples with a relatively large thickness (1.5 µm) with respect to the width (3 µm), we have acquired a resistivity versus temperature curve that resembles data acquired on mm-sized bulk crystals (see Figure B.1a): we observe a hysteretic curve that displays an abrupt transition upon cooling through the MIT. N.B., the other transport properties of this sample are fully resembling a typical microscopic sample, including a high Figure of Merit current density. A false colored scanning electron micrograph of this sample is found in Figure B.1b.

A possible origin of the observed broadening of the transition might be strain patterns in the sample caused by the coupling to the substrate. While driving low currents (current densities well below the IMT; including the FOM), our microscopic samples do not experience any strain. However, near the IMT - independent of whether it is induced by current or temperature - this no longer holds, as the lattice constants significantly alter and strain effect can dominate[4, 5]. Furthermore, a broadening of the transition is commonly observed in thin films, where strain caused by the substrate is a crucial parameter[32–34].

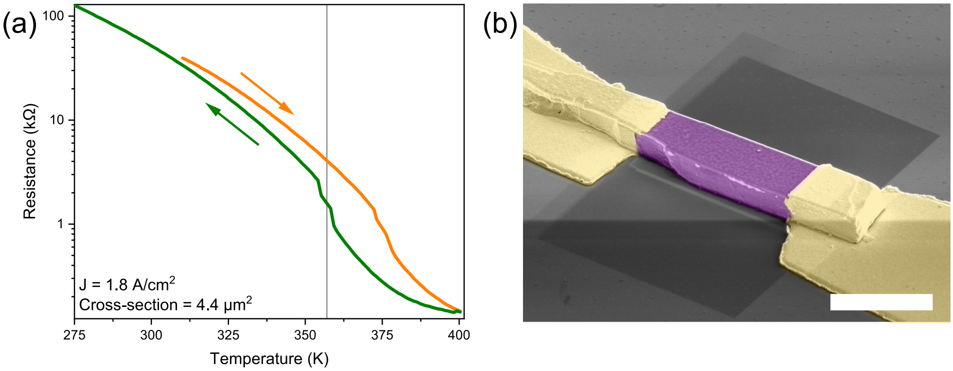

Figure B.1: (a) Shows the resistance versus temperature of a microscopic sample that is 1.5 μm thick and 3 μm wide, which is relatively thick for a sample in the microscopic size range. We observe hysteresis on cycling the temperature and see an abrupt change in resistance when passing the thermal transition temperature of 357K, as indicated by the vertical reference line. In (b), a false colored scanning electron micrograph is shown of the sample used to gather data in Figure (a). Purple indicates the crystal and yellow colored are the titanium/gold contacts. The scale bar corresponds to 5 μm.

C. THE FIGURE OF MERIT AS A FUNCTION OF OTHER LENGTH SCALES

In Figure 6.3, we have chosen to plot the Figure of Merit as a function of the cross-sectional area. Here we present the same data as a function of thickness, width, and length (between the voltage contacts) of the crystal, as plotted in Figure C.1. Most interesting are the samples on which we have performed a thinning study, highlighted by the use of a non-circular symbol in Figure C.1. For the samples of constant thickness, we observe that the FOM can change an order of magnitude in a single sample while decreasing the width, which rules out a dependence solely on thickness. A similar argument can be made for the width and length dependence. Indeed, we have carried out a single step of decreasing the thickness of a sample, which is indicated by the use of arrows in Figure C.1. While the width is constant, the Figure of Merit changes again if we decrease the thickness of this sample.

If we, however, plot the Figure of Merit as a function of the cross-sectional area of the sample, as is done in Figure 6.3, we find that the thinning study samples follow a more coherent trend. Therefore, we use the cross-section as a typical length scale measure. We can conclude from this observation that neither thickness, width, nor length of the crystal solely governs the Figure of Merit, meaning that none of these dimensions are more critical in determining the transport properties of the crystal.

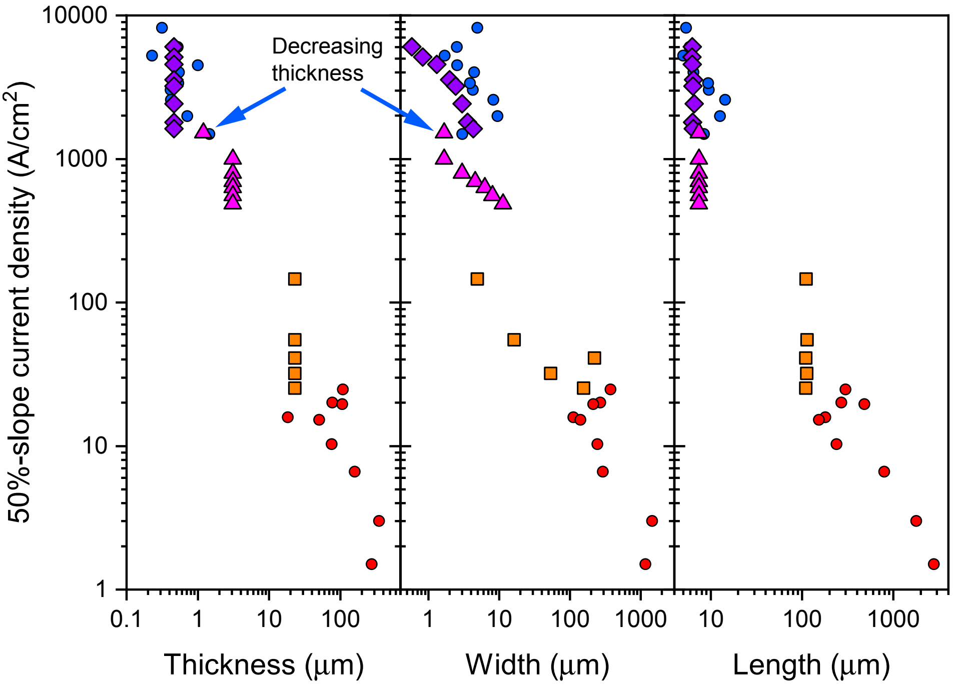

Figure C.1: the 50%-slope current density (FOM) shown as a function of different length scale parameters of the measured samples. In this Figure, each data point represents a single sample. The non-circular symbols represent the thinning study samples (see Figure 6.4 for images of these). The arrows indicate the decrease of thickness during the thinning study on the sample depicted in Figure 6.4c and 6.4d.

D. RECONSTRUCTING THE JE-CHARACTERISTIC ON BASIS OF JOULE HEATING ONLY

Using analytical differentiation it is possible to calculate $\mathrm{d}E/\mathrm{d}J$ from $E(J)$. Reversely, one can calculate $E(J)$ by integration of $\mathrm{d}E/\mathrm{d}J$. The latter introduces an integration constant that needs to be set by a boundary condition. The boundary condition in our case is the requirement of zero electric field for zero current density: $E(0) = 0$. To summarize:

$$E(J) \xrightarrow{\text{diff.}} \frac{\mathrm{d}E}{\mathrm{d}J}(J) \xrightarrow{\text{int.}} E_{\text{recon.}}(J) + C_{\text{int.}} \xrightarrow{\text{Boundary condition}} E_{\text{recon.}}(J) = E(J) \tag{6.4}$$

Here $C_{\text{int.}}$ is the integration constant and $E_{\text{recon.}}$ is the reconstructed electric field from the derivative $\mathrm{d}E/\mathrm{d}J$. As a sanity check, we perform differentiation and integration sequentially on acquired electric field and recover the originally measured data (see Figure D.1a).

The resistivity as a function of temperature is measured by calculating the slope of the

JE-characteristic for low currents (i.e., here, the slope of $E(J)$ is current independent, and no local temperature increase is measured). We can therefore interchange the resistivity as a function of temperature for the $\mathrm{d}E/\mathrm{d}J$ as a function of temperature at approximately zero applied current:

$$\rho(T) = \frac{\mathrm{d}E}{\mathrm{d}J}(T, J \approx 0) \tag{6.5}$$

The application of the Pt-thermometer allows us to measure the local absolute temperature as a function of the current density in the sample. When the crystal temperature increases, the resistivity lowers, causing a decrease of $\mathrm{d}E/\mathrm{d}J$ and, therefore, a decline of the slope of the JE-characteristic. Since we have both the $\mathrm{d}E/\mathrm{d}J$ as a function of temperature and the temperature as a function of current density available, we can combine these to find the $\mathrm{d}E/\mathrm{d}J$ as a function of the locally measured temperature

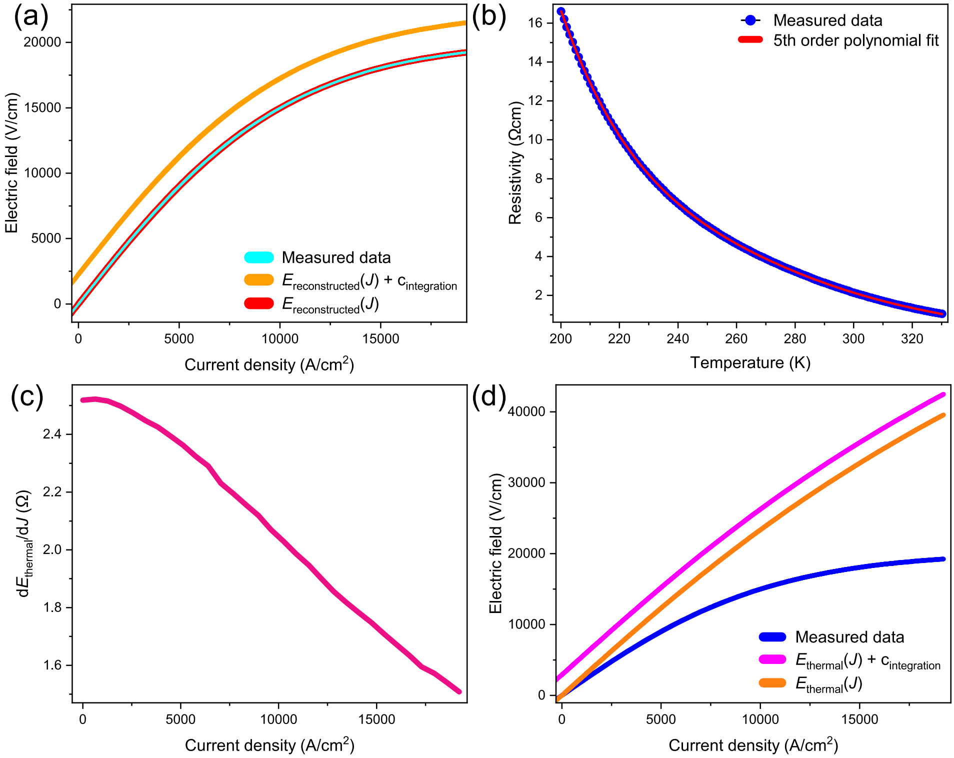

Figure D.1: Summary of calculating E_{thermal}. As a sanity check, we perform subsequent differentiation and integration of a dataset and retrieve the original measured data, which is depicted in (a). (b) shows the resistivity versus temperature curve measured on a sample with embedded Pt-thermometer. The data is fitted by a 5th order polynomial to capture its phenomenological behavior. This fit is used to find the $\mathrm{d}E_{\text{thermal}}/\mathrm{d}J(J)$ (shown in (c)), which is integrated to retrieve E_{thermal} (shown in (d) and Figure 6.8b).

caused by the application of current density, which we denote as $\mathrm{d}E_{\text{thermal}}/\mathrm{d}J$:

$$\frac{\mathrm{d}E}{\mathrm{d}J}(T, J \approx 0) \ \& \ T(J) \xrightarrow{substitution} \mathrm{d}E_{\text{thermal}}/\mathrm{d}J(J) \tag{6.6}$$

To make this substitution, we fit the measured resistivity as a function of temperature with a 5th order polynomial to capture its phenomenological behavior (see Figure D.1b). Next, we use the fitted function to calculate $\mathrm{d}E_{\text{thermal}}/\mathrm{d}J$, which is depicted in Figure D.1c. Finally, we apply the above described procedure to reconstruct E_{thermal} using integration, yielding the data that is shown in Figure 6.8b and Figure D.1d.

E. MINIMAL MODEL FOR CURRENT DENSITY INHOMOGENEITY OVER THE CROSS-SECTIONAL AREA

The cross section dependence might be explained by an inhomogeneous current density distribution throughout the cross-sectional area. Here we present a minimal toy model and phenomenologically compare it to the measured data.

Crucial in this analysis is the difference between the *apparent* current density, namely the total current (I) divided by the total cross-sectional area (A):

$$J_{\text{app}} = I/A \tag{6.7}$$

and the *actual* current density that might be dependent on coordinates spanning the cross-sectional area:

$$J_{\text{act}} = \frac{\mathrm{d}I}{\mathrm{d}A}(x, y) \tag{6.8}$$

Where x (y) is a length parameter that runs between $-D/2$ ($-W/2$) and $D/2$ ($W/2$), with D (W) the thickness (width) of the crystal. The actual and apparent current density can be related to each other by integrating the actual current density to find the total current:

$$J_{\text{app}} = I/A = 1/A \iint \frac{\mathrm{d}I}{\mathrm{d}A}(x, y)\mathrm{d}A \tag{6.9}$$

Therefore a homogeneous current distribution (i.e., a constant actual current density) yields an equal apparent current density:

$$J_{\mathrm{act}} = J_0 \to J_{\mathrm{app}} = 1/A \iint J_0 \mathrm{d}A = \frac{AJ_0}{A} = J_0 = J_{\mathrm{act}} \tag{6.10}$$

We can examine what type of actual current density features the power law dependence on the cross-sectional area observed in the measured current density (displayed in Figure 6.3). To do so, we assume that the actual current density decreases as $J_{\mathrm{act}} = J_0 \lambda^a l^{-a}$. Here a is a dimensionless constant, λ is a characteristic length scale, and l is the distance from the edges of the sample. This means, for a rectangular cross-section, that the total current is given by:

$$I = 4J_0\lambda^a \int_0^{D/2} \int_0^{W/2} \frac{\mathrm{d}I}{\mathrm{d}A}(x,y)\mathrm{d}t\mathrm{d}w \tag{6.11}$$

Here, we used the fact that the system is symmetric in four sectors. Each of those can be divided into two parts:

$$I = 4J_0\lambda^a \left[\int_0^{D/2} \int_0^{\frac{W}{D}x} y^{-a}\mathrm{d}y\mathrm{d}x + \int_0^{W/2} \int_0^{\frac{D}{W}y} x^{-a}\mathrm{d}x\mathrm{d}y \right] \tag{6.12}$$

Leading to:

$$I = \frac{J_0\lambda^a}{(1-a)(2-a)} \left[\left(\frac{D}{W}\right)^{1-a} \left(\frac{W}{2}\right)^{2-a} + \left(\frac{W}{D}\right)^{1-a} \left(\frac{D}{2}\right)^{2-a} \right] \tag{6.13}$$

Where we assumed $a \neq 1$. This can be simplified to:

$$I = \frac{8J_0\lambda^a}{(1-a)(2-a)}(DW)^{1-a} = \frac{8}{(1-a)(2-a)}A^{1-a} \tag{6.14}$$

That entails for the apparent current density:

$$J_{\mathrm{app}} = I/A = \frac{8J_0\lambda^a}{(1-a)(2-a)}\frac{A^{1-a}}{A} = \frac{8J_0\lambda^a}{(1-a)(2-a)}A^{-a} \sim A^{-a} \tag{6.15}$$

Which is the observed power law dependence of the measured current density.

REFERENCES

[1] Nakatsuji, S., Ikeda, S.-i. & Maeno, Y. Ca_2RuO_4: new Mott insulators of layered ruthenate. *J. Phys. Soc. Jpn.* **66**, 1868–1871 (1997).

[2] Alireza, P. L. *et al.* Evidence of superconductivity on the border of quasi-2D ferromagnetism in Ca_2RuO_4 at high pressure. *J. Condens. Matter Phys.* **22**, 052202 (2010).

[3] Nakamura, F. *et al.* From Mott insulator to ferromagnetic metal: A pressure study of Ca_2RuO_4. *Phys. Rev. B* **65**, 220402 (2002).

[4] Cirillo, C. *et al.* Emergence of a metallic metastable phase induced by electrical current in Ca_2RuO_4. *Phys. Rev. B* **100**, 235142 (2019).

[5] Bertinshaw, J. *et al.* Unique crystal structure of Ca_2RuO_4 in the current stabilized semimetallic State. *Phys. Rev. Lett.* **123**, 137204 (2019).

[6] Fürsich, K. *et al.* Raman scattering from current-stabilized nonequilibrium phases in Ca_2RuO_4. *Phys. Rev. B* **100**, 081101 (2019).

[7] Zhang, J. *et al.* Nano-resolved current-induced insulator-metal transition in the Mott insulator Ca_2RuO_4. *Phys. Rev. X* **9**, 011032 (2019).

[8] Alexander, C. S. *et al.* Destruction of the Mott insulating ground state of Ca_2RuO_4 by a structural transition. *Phys. Rev. B* **60**, R8422(R) (1999).

[9] Nakatsuji, S., Ando, T., Mao, Z. & Maeno, Y. Metal–insulator transition in $Ca_{x-2}Sr_xRuO_4$. *Phys. B: Condens. Matter* **259-261**, 949–950 (1999).

[10] Nakatsuji, S. & Maeno, Y. Quasi-two-dimensional Mott transition system $Ca_{x-2}Sr_xRuO_4$. *Phys. Rev. Lett.* **84**, 2666–2669 (2000).

[11] Nakatsuji, S. & Maeno, Y. Synthesis and single-crystal growth of $Ca_{x-2}Sr_xRuO_4$. *J. Solid State Chem.* **156**, 26 – 31 (2001).

[12] Sutter, D. *et al.* Orbitally selective breakdown of Fermi liquid quasiparticles in $Ca_{1.8}Sr_{0.2}RuO_4$. *Phys. Rev. B* **99**, 121115 (2019).

[13] Steffens, P. *et al.* High-pressure diffraction studies on Ca_2RuO_4. *Phys. Rev. B* **72**, 094104 (2005).

[14] Nakamura, F. Pressure-induced Mott transition and related novel quantum phenomena in Ca_2RuO_4. *J. Phys. Soc. Jpn.* **76**, 96–99 (2007).

[15] Braden, M., André, G., Nakatsuji, S. & Maeno, Y. Crystal and magnetic structure of Ca_2RuO_4 magnetoelastic coupling and the metal-insulator transition. *Phys. Rev. B* **58**, 847–861 (1998).

[16] Zegkinoglou, I. *et al.* Orbital ordering transition in Ca_2RuO_4 observed with resonant X-ray diffraction. *Phys. Rev. Lett.* **95**, 136401 (2005).

[17] Nakamura, F. *et al.* Electric-field-induced metal maintained by current of the Mott insulator Ca_2RuO_4. *Sci. Rep.* **3**, 2536 (2013).

[18] Okazaki, R. *et al.* Current-induced gap suppression in the mott insulator Ca_2RuO_4. *J. Phys. Soc. Jpn.* **82**, 103702 (2013).

[19] Taguchi, Y., Matsumoto, T. & Tokura, Y. Dielectric breakdown of one-dimensional Mott insulators Sr_2CuO_3 and $SrCuO_2$. *Phys. Rev. B* **62**, 7015–7018 (2000).

[20] Kanki, T., Kawatani, K., Takami, H. & Tanaka, H. Direct observation of giant metallic domain evolution driven by electric bias in VO_2 thin films on TiO_2(001) substrate. *Appl. Phys. Lett.* **101**, 243118 (2012).

[21] Yang, Z., Ko, C. & Ramanathan, S. Oxide electronics utilizing ultrafast metal-insulator transitions. *Annu. Rev. Mater. Res.* **41**, 337–367 (2011).

[22] Stoliar, P. *et al.* A leaky-integrate-and-fire neuron analog realized with a Mott insulator. *Adv. Funct. Mater.* **27**, 1604740 (2017).

[23] Mattoni, G., Yonezawa, S., Nakamura, F. & Maeno, Y. Role of local temperature in the current-driven metal-insulator transition of Ca_2RuO_4. *Phys. Rev. Mater.* **4**, 114414 (2020).

[24] Jenni, K. *et al.* Evidence for current-induced phase coexistence in Ca_2RuO_4 and its influence on magnetic order. *Phys. Rev. Mater* **4**, 085001 (2020).

[25] Okazaki, R. *et al.* Current-induced giant lattice deformation in the Mott insulator Ca_2RuO_4. *J. Phys. Soc. Jpn.* **89**, 044710 (2020).

[26] Terasaki, I. *et al.* Non-equilibrium steady state in the Mott insulator Ca_2RuO_4. *J. Phys. Soc. Jpn.* **89**, 093707 (2020).

[27] Chiriacò, G. & Millis, A. J. Polarity dependent heating at the phase interface in metal-insulator transitions. *Phys. Rev. B* **102**, 085116 (2020).

[28] Friedt, O. *et al.* Structural and magnetic aspects of the metal-insulator transition in Ca_2RuO_4. *Phys. Rev. B* **63**, 174432 (2001).

[29] Gorelov, E. *et al.* Nature of the Mott transition in Ca_2RuO_4. *Phys. Rev. Lett.* **104**, 226401 (2010).

[30] Huang, Y. *et al.* Reliable exfoliation of large-area high-quality flakes of graphene and other two-dimensional materials. *ACS Nano* **9**, 10612–10620 (2015).

[31] Fermin, R. Fabrication of mesoscopic structures with superconducting Sr_2RuO_4 Master thesis, Universiteit Leiden (2017).

[32] Tsurumaki-Fukuchi, A. *et al.* Stable and tunable current-induced phase transition in epitaxial thin films of Ca_2RuO_4. *ACS Appl. Mater. Interfaces* **12**, 28368–28374 (2020).

[33] Miao, L. *et al.* Itinerant ferromagnetism and geometrically suppressed metal-insulator transition in epitaxial thin films of Ca_2RuO_4. *Appl. Phys. Lett.* **100**, 052401 (2012).

[34] Wang, X., Xin, Y., Stampe, P. A., Kennedy, R. J. & Zheng, J. P. Epitaxial thin film growth of $Ca_2RuO_{4+\delta}$ by pulsed laser deposition. *Appl. Phys. Lett.* **85**, 6146–6148 (2004).

[35] Dietl, C. *et al.* Tailoring the electronic properties of Ca_2RuO_4 via epitaxial strain. *Appl. Phys. Lett.* **112**, 031902 (2018).

[36] Grinenko, V. *et al.* Split superconducting and time-reversal symmetry-breaking transitions in Sr_2RuO_4 under stress. *Nat. Phys.* **17**, 748–754 (2021).

[37] Barber, M. E., Gibbs, A. S., Maeno, Y., Mackenzie, A. P. & Hicks, C. W. Resistivity in the vicinity of a van Hove singularity: Sr_2RuO_4 under uniaxial pressure. *Phys. Rev. Lett.* **120**, 076602 (2018).

[38] Steppke, A. *et al.* Strong peak in Tc of Sr_2RuO_4 under uniaxial pressure. *Science* **355**, eaaf9398 (2017).

[39] Lange, M. *et al.* Imaging of electrothermal filament formation in a Mott insulator. *Phys. Rev. Applied* **16**, 054027 (2021).

[40] Fukazawa, H., Nakatsuji, S. & Maeno, Y. Intrinsic properties of the Mott insulator $Ca_2RuO_{4+\delta}(\delta = 0)$ studied with single crystals. *Phys. B: Condens. Matter* **281-282**, 613–614 (2000).

[41] Granata, V. *et al.* Crystal growth of the Ca_2RuO_4–Ru metal system by the floating-zone technique. *J. Alloys Compd.* **832**, 154890 (2020).

7

CONTROLLING CHIRAL DOMAIN WALLS IN MESOSCOPIC Sr_2RuO_4 USING GEOMETRY AND IN-PLANE MAGNETIC FIELDS

I would like to acknowledge contributions from: G. Stam, J. Ridderbos, A. Brinkman, J. Aarts, K. Lahabi & Y. Maeno

Despite more than a quarter-century of tremendous experimental and theoretical effort, the pairing symmetry of the correlated electron superconductor Sr_2RuO_4 remains elusive. Regardless of the pairing symmetry, however, some of these works found evidence of superconducting chiral domains in bulk crystals. In previous research, we were able to trap a single chiral domain wall, separating such domains, in mesoscopic rings of Sr_2RuO_4. In this chapter, we further examine the properties of these domain walls and find that they are stable over a large range of sample geometries that are either singly or doubly connected. By obtaining the Shapiro response of our samples, we provide definite proof of the Josephson coupling of the domain-wall-associated junctions and gain insight into the periodicity of their current-phase relation. We show that we can alter the domain structure by applying small in-plane magnetic fields (in the ab-plane; $H < H_{c1}$), which manifests itself as the appearance of half-integer Shapiro steps in the IV-characteristic. Furthermore, we find that the in-plane fields can unpin the chiral domain walls, which results in a bistability of the critical current. By applying either a positive or negative current bias, we switch between a low and high I_c state, which resembles a superconducting memory element. Combined, the experiments in this chapter form compelling evidence for the presence of chiral domains, which, in light of recent literature, indicates that a chiral d-wave order parameter describes superconductivity of Sr_2RuO_4.

To be submitted.

7.1. INTRODUCTION

The pairing symmetry of a superconductor determines many of its characteristics and is often established soon after its discovery. The famous example is d-wave superconductivity in the high T_c cuprates[1–3], which was experimentally established within eight years after its Nobel-prize-winning discovery in 1986[4]. Despite plentiful experimental and theoretical efforts, the pairing symmetry of the unconventional superconductor Sr_2RuO_4 has remained one of the larger open questions of condensed matter physics for over the last quarter-century. At the time of writing, there are two main classes of proposals: an order parameter characterized by a two-component nature, with $d_{xz} \pm i d_{yz}$ as the most prominent candidate, or an accidental degeneracy between two single-component order parameters, where $s \pm i d_{xy}$ and $d_{x^2-y^2} \pm i g_{xy(x^2-y^2)}$ are most promising.

A possible way of discriminating between the two classes is the proposed chirality of the order parameter. In a chiral superconductor, the superconducting ground state is two-fold degenerate, which leads to the spontaneous emergence of superconducting domains, each corresponding to a single chirality. Therefore, detecting these domains provides direct evidence for a chiral pairing symmetry. $p_x \pm i p_y$ and $d_{xz} \pm i d_{yz}$ are such chiral pairing symmetries, for example, while p_x and $d_{x^2+y^2}$ are not. Instead of detecting the domains, we can also focus on the chiral domain walls separating them. At the domain wall, the order parameter of both chiralities is locally suppressed, which manifests itself as a Josephson junction[5]. Since the domain size is typically in the micrometer range, trapping a single domain wall in experiments is impossible in macroscopic crystals. This provides a strong motivation for reducing the size of the crystals in well-controlled geometries.

In previous work, we found the emergence of spontaneous Josephson junctions in mesoscopic rings of Sr_2RuO_4, which we interpreted as chiral domain walls associated with a chiral p-wave pairing symmetry[6]. In this chapter, we provide further examination of these domain walls. By obtaining measurements of Shapiro steps on these junctions, we not only provide definitive proof of the Josephson coupling but also a further study of the periodicity of the current-phase relation of the domain wall junctions. We find that, under the application of small in-plane fields, the periodicity of the current-phase relation can be altered, which leads to the observation of fractional Shapiro steps. Furthermore, in-plane fields reveal a two-level state in the critical current of the junctions, where the application of electrical current can be used to switch between each state, resembling a superconducting memory. Finally, we will try to provide a reinterpretation of these results based on the most recent experimental and theoretical works considering the pairing symmetry of Sr_2RuO_4. To achieve this goal, this chapter will commence with a history of the experimental progress on the pairing symmetry in Sr_2RuO_4.

7.2. BRIEF EXPERIMENTAL HISTORY OF THE PAIRING SYMMETRY IN Sr_2RuO_4

Soon after its discovery of in 1994[7], it was noted that superconductivity in Sr_2RuO_4 is highly sensitive to non-magnetic disorder and that it bears many similarities to the A-phase of liquid ^{3}He[8–10]. This started the search for experiments and theoretical models that further examine the pairing symmetry[11, 12]. This section will give a brief overview of these experiments.

7.2.1. AN UNCONVENTIONAL SUPERCONDUCTOR

The breakthrough experiments that have shaped the understanding of the pairing symmetry focus on the breaking of time reversal symmetry (TRS) in the superconducting state. Specifically, it was found using muon spin resonance experiments and polar Kerr microscopy that internal magnetic fields spontaneously appear below T_c (see Figure 7.1a)[13, 14]. Moreover, using doped samples, with reduced T_c, it was shown that TRS breaking is directly tied to the onset of superconductivity[15]. The breaking of TRS at T_c has an important consequence: the superconducting order parameter is of a two-component nature.[1][16] For the tetragonal lattice of Sr_2RuO_4, i.e., a D_{4h} symmetry point group, this entails either a spin triplet p-wave pairing: $p_x \pm ip_y$ ($S = 1$, $L = 1$), or singlet d-wave pairing: $d_{xz} \pm id_{yz}$ ($S = 0$, $L = 2$).[2] Next, Sr_2RuO_4 was examined by nuclear magnetic resonance (NMR) Knight shift measurements and inelastic neutron scattering experiments, which both measure the spin susceptibility of the electronic system. It was found that spin susceptibility below the critical current is not suppressed, indicating a triplet order parameter (see Figure 7.1b)[17, 18]. Furthermore, using cantilever magnetometry measurements, it was found that mesoscopic rings of Sr_2RuO_4 can host half-quantum vortices under the application of an in-plane magnetic field[19]. This further strengthens the hypothesis of a triplet order parameter, where the Cooper pair spins lie in the ab-plane. Therefore, for a long time, the prime candidate for the pairing symmetry was $p_x \pm ip_y$.

However, some inconsistencies with the chiral p-wave picture remained. First, the upper critical field $H_{\mathrm{c}2}$ in the ab-plane is Pauli limited[20]. Pauli limiting behavior results from the balance between superconducting condensation energy (set by the magnitude of the gap) and magnetic polarization energy (set by the spin susceptibility)[21]. If $H_{\mathrm{c}2}$ in the ab-plane is Pauli limited, this signifies a suppression of the spin susceptibility below T_c, which is in direct contradiction to the spin susceptibility measurements. Besides, detecting the magnetic fields produced by the proposed edge currents associated with the chiral p-wave pairing using scanning SQUID remained elusive[22].

---

[1] More components are allowed, but less likely as they require more fine-tuning between the components.

[2] These are the lowest orders. In principle, chiral f-wave, chiral h-wave, or even higher orders are allowed, although Occam's razor speaks against them.

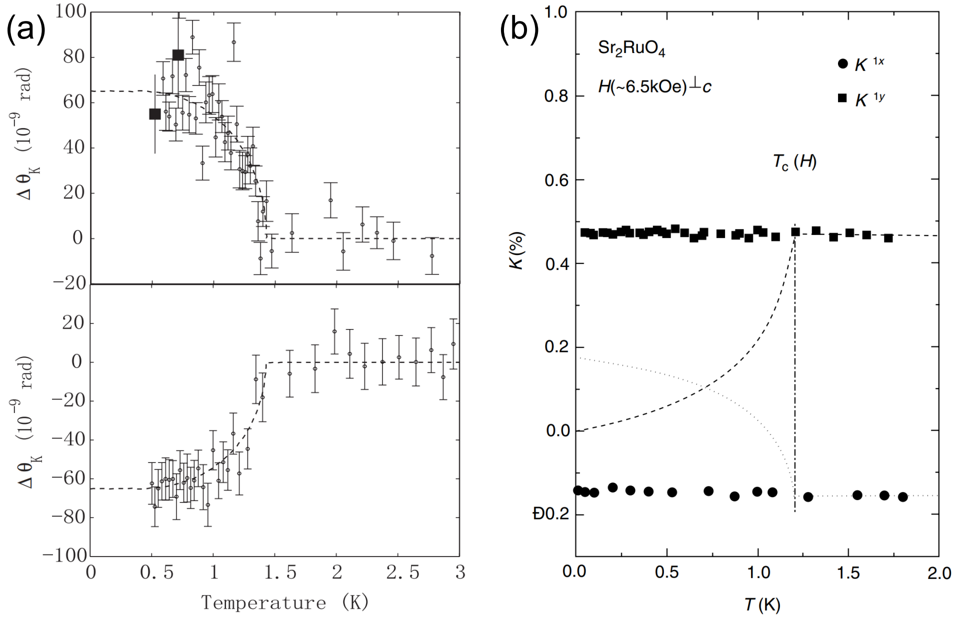

Figure 7.1: Reproduction of two classic results obtained on Sr_2RuO_4. (a) shows a measurement of the magneto-optic Kerr effect, which is the rotation of polarized light reflected on the surface of a Sr_2RuO_4 crystal as a function of temperature. The polarization indicates local magnetism, which only appears below $T_c = 1.5$ K. This result is one of the two main bodies of evidence for a broken TRS superconducting state in Sr_2RuO_4 (the other being muon spin resonance[13]). The sign of the polarization rotation can be controlled by field cooling the sample, as evidenced by the difference between the lower and upper panel, which indicates a chiral pairing. Figure reproduced from ref. [14]. In (b), a measurement of the ^{17}O Knight shift as a function of temperature is shown. This technique measures the spin susceptibility of the electronic system, which was found to be unsuppressed below T_c. Together with work on polarized-neutron scattering[18], this formed strong evidence for a triplet order parameter for over twenty years. Reproduced from ref. [17].

7.2.2. POST-2019 RESULTS: A SHIFT FROM THE p-WAVE PARADIGM

It is not an understatement that our lives changed dramatically at the end of 2019 and the beginning of 2020: the NMR Knight shift experiments on Sr_2RuO_4 were revisited, and it was found that the unsuppressed spin susceptibility was caused by a subtle heating effect of the substrate holder[23, 24]. Likewise, the inelastic neutron scattering measurements were repeated using lower magnetic field pulses and improved statistics, confirming the spin susceptibility suppression below T_c[25]. On the other hand, TRS breaking experiments were also repeated and found still valid. specifically, by applying uniaxial strain to the crystals during muon spin resonance experiments, it was revealed that the critical temperature can be raised even to double its unstrained value, while the temperature at which TRS is broken (T_{TRS}) remained at 1.5 K (see Figure 7.2a)[26]. This was interpreted as a strain-induced increase of T_c of one component of the wave function, whereas the T_c of the second component remained the same at T_{TRS}. Therefore only below T_{TRS} this results in a two-component pairing. Besides, this experiment also shows a clear difference between the intrinsic unstrained supercon-

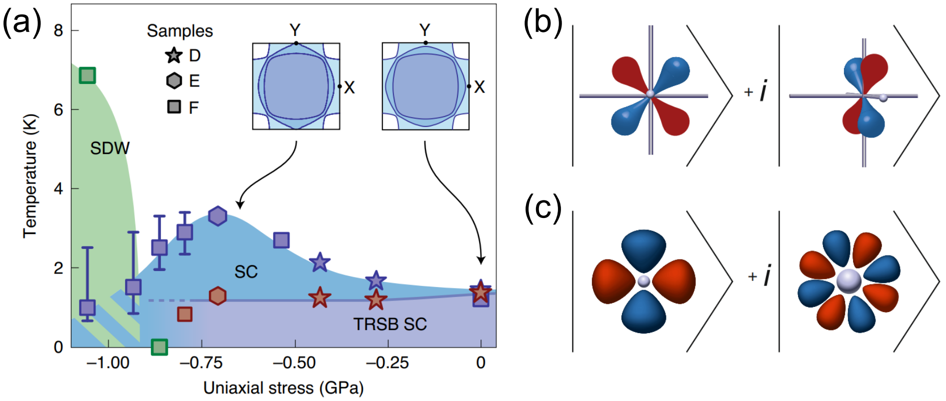

Figure 7.2: (a) phase diagram detailing the time reversal symmetry breaking (TRSB) under the uniaxial stress, as determined by muon spin resonance. Even though the T_c of the superconducting (SC) phase can be more than doubled, T_{TRS} remains 1.5 K. This was interpreted as a rise in critical temperature corresponding to one of the two components of the wave function. At high strain, a spin density wave (SDW) is revealed. The inset shows a schematic of the Fermi surface of Sr_2RuO_4; the origin of the peak in T_c lies in the γ-band passing through a Lifshitz transition near the maximum T_c. Image taken from ref. [26]. (b) and (c) show a schematic representation of the two most likely candidates for the pairing symmetry of Sr_2RuO_4: $d_{xz} \pm i d_{yz}$ and $d_{x^2-y^2} + i g_{xy(x^2-y^2)}$ pairing respectively. The color coding is similar as in Figure 2.2. Images taken from ref. [30].

ducting state and the extrinsic increased-T_c state, coined the '3K-phase'. The latter was identified as resulting from strain[27]. In conclusion, this collection of experiments caused a shift away from the p-wave paradigm toward even parity order parameters, with most prominently $d_{xz} \pm i d_{yz}$ pairing, i.e., the chiral d-wave pairing (see schematic in Figure 7.2b).

There is, however, evidence against $d_{xz} \pm i d_{yz}$ pairing, as well. First, from thermal conductivity measurements, it was shown that vertical line nodes exist in the gap structure, which is incompatible with chiral d-wave pairing[28]. Besides, a chiral d-wave state should exhibit a second transition in the heat capacity, tied to T_{TRS}, which can be revealed under uniaxial strain. However, in recent measurements, this second discontinuity was lacking[29].

An alternative route to resolve these issues is by assuming an accidental degeneracy between two single component order parameters. Most notable are the proposals for $s \pm i d_{xy}$ and $d_{x^2-y^2} \pm i g_{xy(x^2-y^2)}$ [31–33]. These, especially the latter, might seem exotic, but they resolve the breaking of TRS with the vertical line node and the missing second discontinuity in the heat capacity. The $s \pm i d_{xy}$ pairing is supported by the strong spin-orbit and Hund's coupling present in the normal state, resulting in a possibly interorbital triplet pairing that behaves as intraband singlets; therefore, this pairing is coined 'shadowed triplet'[34, 35]. Furthermore, $d_{x^2-y^2} \pm i g_{xy(x^2-y^2)}$ (see schematic in Figure 7.2c) is compatible with the temperature dependence of the elastic constants in recent ultrasound measurements[36, 37], and the quadratic dependence of $T_{TRS} - T_c$

on uniaxial strain[38], among many other experimental observations[33]. On the other hand, such an accidental degeneracy requires fine-tuning of the material parameters. In other words: in a universe dominated by s-wave and some d-wave superconductors, an accidental degeneracy between d- and g-wave is a *very* major coincidence. More importantly, although uniaxial stress splits T_{TRS} and T_{c}, it was found that hydrostatic pressure induces a downward trend in both, which is highly unlikely for an accidental degeneracy[39]. Finally, neither $d \pm ig$ pairing nor chiral d-wave pairing can account for the observation of half quantum vortices in magnetometry measurements, and the proximity effect in Sr_2RuO_4-SF hybrid structures[3] [19, 41].

Clearly, a plethora of proposed pairing symmetries are found in literature based on seemingly contradicting experimental results. What does that leave us for the *actual* pairing symmetry of Sr_2RuO_4? Maybe the best answer can be found in ref. [39]: "the difficulty in reconciling apparently contradictory experimental results in Sr_2RuO_4 may mean that one or more major, apparently solid results will in time be found to be incorrect, either for a technical reason or in interpretation. Further experiments are therefore necessary." Regardless of the validity of previous experiments, almost all of the work discussed in this section concerns macroscopic crystals. As argued in the introduction, a chiral superconductor can break up into domains, which for Sr_2RuO_4 is supported by numerous studies, for example, by the observation of telegraph noise in Sr_2RuO_4 corner junctions and the sign change in the Kerr signal, during field-cooled experiments[14, 42, 43]. As these are typically micrometer-sized, studying sub-micron devices can lead to experiments on a single domain, or better yet, on a single domain wall separating the two domains. Our first efforts in trapping a single chiral domain wall, published in a previous work, are discussed below.

7.3. TRAPPING A SINGLE SUPERCONDUCTING DOMAIN WALL IN MESOSCOPIC Sr_2RuO_4

In Chapter 6, we described a procedure of fabricating microscopic flakes from a bulk crystal using mechanical exfoliation. Sr_2RuO_4 is well suited to create microstructures using the same method. Therefore, the same procedure is applied for the sample production in this chapter. For a more detailed discussion of the sample production method, see Appendix A of Chapter 6.[4] Specifically, we used this method in a previous work to structure microrings in the exfoliated crystals[6]. Striking about these micro devices, and the ones presented in the rest of this chapter, are their high residual resistivity ratio (RRR) and their bulk T_{c}, indicating that neither the exfoliation method nor the focused ion beam structuring method affects the crystal quality. Besides, since the T_{c} never exceeds 1.5 K, it gives indisputable proof of the absence of the 3K-phase and,

---

[3] Although, within the $d \pm ig$ pairing framework half-quantum vortices can exist, they require a specific varying strain pattern[40].

[4] The crystals were grown using the floating zone method in the group of Y. Maeno[44].

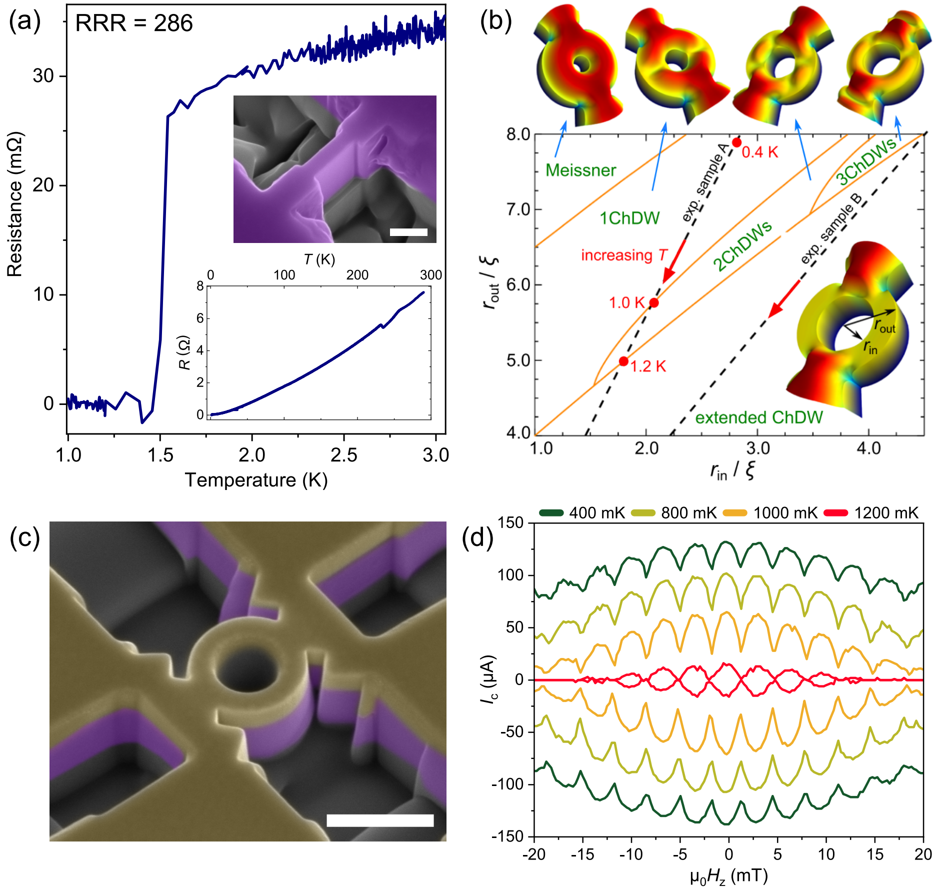

Figure 7.3: (a) Resistance versus temperature of a 200 nm wide constriction in a Sr_2RuO_4 flake. Despite the mechanical exfoliation and the microstructuring using focused ion beams, the device retained a bulk T_c of 1.5 K and a high residual resistivity ratio. The insets show a false colored scanning electron micrograph of the measured device (the scale bar corresponds to 500 nm) and the same dataset plotted for the full temperature range. (b) shows a phase diagram of chiral domain configurations in a microstructured ring based on time-dependent Ginzburg-Landau simulations of a chiral p-wave order parameter. The outer and inner diameter of the ring, normalized to the coherence length, determine the specific configuration: two chiral domain walls in either arm of the ring are stable over a wide temperature range. In the schematic rings, the color code signifies the Cooper pair density, which illustrates that such domain configuration can act as a SQUID-like system. Figure modified from ref. [6]. Here *exp. sample B* is describing Ring 2, and since sample dimensions of Ring 1 are very similar to those of Ring 2, it can be represented by a very similar line (not plotted here). (c) False colored scanning electron micrograph of Ring 1. The crystal is colored purple, protected by a yellow colored layer of gold. The scale bar corresponds to 1 μm. In (d), the critical current versus perpendicular applied magnetic field ($I_c(B)$) is shown, obtained on Ring 1. Over a large range of temperatures, we observe SQUID-like oscillations, despite the homogeneous crystal.

therefore, any significant strain in these devices[27]. A good example is the resistance versus temperature of the 200 nm wide bar presented in Figure 7.3a. In Appendix A we present an overview of the ring samples used to obtain the data presented in this chapter. Some of the experiments presented in this chapter were carried out at Twente University, Appendix A discusses which ones.

For such clean systems, a uniform superconducting phase is expected. The experimental reality is, therefore, quite surprising: the $I_c(B)$-pattern shows clear oscillations with a period determined by fluxoid quantization corresponding to the area of the ring. Typically this pattern is observed on superconducting quantum interference devices (SQUIDs), which are two Josephson junctions in parallel, creating a doubly connected superconductor in a loop geometry. This means that, once the crystal is cooled below T_c, two Josephson junctions spontaneously appear in each arm of the ring. These oscillations, and therefore the junctions, are present at all temperatures below the transition, even down to 50 mK. A false colored scanning electron micrograph of such ring device is shown in Figure 7.3c[5]; $I_c(B)$ obtained on this sample is shown in Figure 7.3d.

Several trivial mechanisms can produce oscillatory behavior of $I_c(B)$ in clean superconducting systems. The arguments against those are reported in reference [6]; here, we will provide a brief overview. First, if the dimensions of a superconducting device are reduced to below the coherence length ξ, naturally, the order parameter is suppressed, and a constriction (or S–s–S) junction is formed. The feature size (e.g., the width of the arms of the ring) of the samples discussed in this chapter is well above the $\xi_{ab-\text{plane}}$ of Sr_2RuO_4, which equals 66 nm at low temperatures. More importantly, such junctions would exhibit a temperature-dependent current-phase relation that leads to a temperature dependence of the shape of the oscillations, which is not measured in our rings[45]. Furthermore, a constriction junction features a multi-valued current-phase relation, which results in a hysteretic IV-characteristic for $T << T_c$[46]. In our samples, however, the retrapping current equals the critical current for all temperatures. The same argument holds against superconducting persistent currents as the origin of the I_c-pattern: aside from the absence of a temperature-dependent amplitude of the oscillations, also the shape does not match the expected sawtooth-like $I_c(B)$ for persistent currents[47]. In addition, current excited vortices can produce oscillations in I_c, however, only in a temperature range to 5% below T_c, not as low as 50 mK[48]. The device in Figure 7.3c is capped by a layer of gold for protection against FIB-induced damages. However, this layer is shorted by the Sr_2RuO_4 crystal in the superconducting phase and therefore cannot be responsible for I_c oscillations. More importantly, the oscillatory behavior is also present in samples that do not have a metallic but insulating capping layer. Finally, accidental weak links, like inclusions and nano cracks, can be ruled out by the large residual resistivity ratios, absence of 3K-phase, and sharp superconducting transitions, indicating pristine crystals.

Alternatively, these spontaneous weak links can be attributed to the presence of superconducting chiral domain walls pinned in the arms of the ring. In order to strengthen this hypothesis, time-dependent Ginzburg-Landau simulations are presented in ref. [6], assuming a chiral p-wave pairing. These show that mono- and multidomain states are stable in ring structures of these dimensions. Besides, a uniform superconducting state can appear. Tuning the inner and outer radius with respect to the coherence length gives rise to these different states, resulting in a phase diagram, reproduced in Figure 7.3b. Combined with the experimental results, this makes compelling evidence for the presence of chiral domain walls. However, since it is unlikely that the pairing symmetry of Sr_2RuO_4 is chiral p-wave, these results need to be reevaluated in light of the most recent literature. The rest of this chapter will be dedicated to this reevaluation and to more recent experiments on the unusual properties of these domain walls revealed under the application of microwave radiation or in-plane magnetic fields.

---

[5] This specific device has a layer of gold on top, which was left after a failed lift-off procedure during fabrication of electrical contacts. We made a virtue of necessity by using this gold as a capping layer. Since gold is not superconducting, the charge transport is completely dominated by the Sr_2RuO_4 in the superconducting phase.

7.4. DETECTION OF SHAPIRO STEPS

Although the SQUID oscillations in $I_c(B)$ form strong evidence for domain walls in the arms of the ring, the magnetic fields used in these experiments can alter the domain structure of a chiral superconductor[6]. Obtaining the Shapiro response of the rings can therefore confirm their presence without relying on static magnetic fields. In Figure 7.4a, we show the appearance of Shapiro steps obtained on one of the ring samples, confirming the Josephson coupling. We show their accompanying power dependence in Figure 7.4b. Since Shapiro steps can only originate from the Josephson effect, their detection directly rules out persistent currents or current-excited vortices as the origin of the observed $I_c(B)$ pattern. Note that relatively large microwave powers are needed to produce the results in Figure 7.4. Besides, Shapiro steps are only measured under the application of a few selected frequencies. The latter is presumably tied to the re-

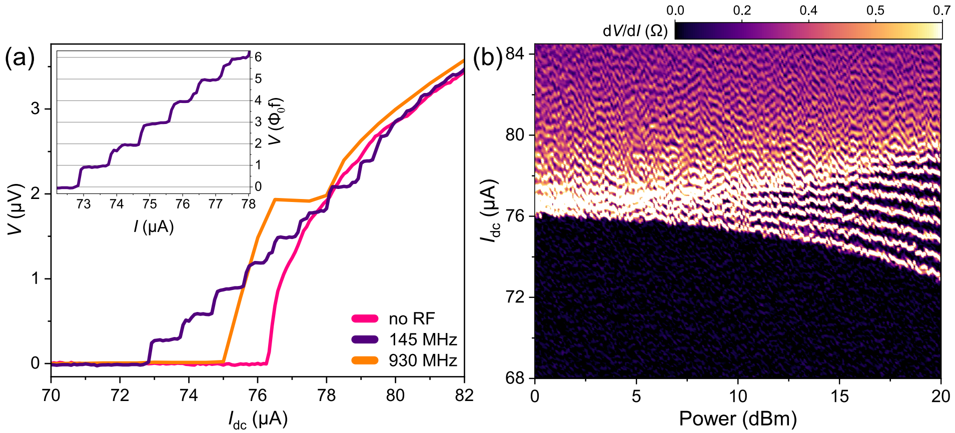

Figure 7.4: Shapiro response obtained on Ring 4. (a) IV-characteristic around I_c for different applied microwave frequencies, obtained at 50 mK and maximum applied power (20 dBm). Clear quantized steps appear near I_c, the height of which linearly scales with the frequency of the applied microwave. The inset shows the data obtained at 145 MHz, rescaled in order to show that the step height matches the expected values for Shapiro steps. In (b), we depict the power dependence of the Shapiro steps obtained at an applied frequency of 145 MHz.

quirement for large microwave powers: for some frequencies, a natural resonance in the cryostat occurs, which results in an amplified local RF field.[6] A possible explanation for the need for high powers is that the bulk superconducting contacts might partially shield the domain walls.

7.5. CONSIDERATIONS ON GEOMETRY

We have investigated the influence of geometry on the domain structure of our devices by obtaining $I_c(B)$ on both doubly and singly connected samples. First of all, we have produced a sample that is a doubly connected straight bar, with large superconducting reservoirs as contacts. Figure 7.5a shows a false colored scanning electron micrograph of this device; the corresponding $I_c(B)$ pattern is shown in Figure 7.5b. We find similar SQUID-like oscillations on this sample as on the ring samples. This directly rules out any influence of the contact geometry on the stability of the chiral domain walls. Furthermore, it shows that the chiral domain walls are stable irrespective of the curvature of the arms of the ring. We have also examined singly connected samples of 500 nm wide and multiple micrometer-sized bar devices. These showed neither an oscillatory $I_c(B)$ nor the appearance of Shapiro steps. Furthermore, the I_c are sharp and well defined, as commonly observed in bulk superconducting samples. Samples that trap a chiral domain wall, on the other hand, exhibit a relatively broad I_c transition. Therefore, we conclude that no junctions are pinned in micrometer-sized bar devices or 500 nm wide constrictions.

In order to isolate and examine only a single junction, we have carried out a second step of FIB processing on the device depicted in Figure 7.3c (Ring 1), during which we cut one of the arms of the ring, changing it into a singly connected sample (see Figure 7.5c). Using the Shapiro response, we verified the Josephson coupling in this singly connected sample and thereby the presence of a chiral domain wall (see Figure 7.6a). We show the corresponding $I_c(B)$ in Figure 7.5d. We observe a monotonic decay of the critical current for all temperatures, which contradicts the Fraunhofer interference pattern expected for a single junction. However, the period of the oscillations is given by the effective area, which is much smaller than the total area of the ring for a single arm. Naively, we can estimate the effective area by multiplying the width of the arm by the coherence length (typical width of a chiral domain wall). We find the period matching this area to exceed the measured values of the upper critical field of this device. Therefore, it is impossible to acquire more than the middle lobe of the interference pattern.

A closer inspection of the interference pattern is presented in Figure 7.6b. Instead of a Fraunhofer pattern that is cut-off by H_{c2}, the data is fitted by a Gaussian decay. Such $I_c(B)$-patterns are generally observed on long diffusive junctions[49–51]. In this limit, the scatter centers lead to the Andreev bound states tracing many different paths through the junction. By the central limit theorem, the phase difference associated with these trajectories will approach a Gaussian distribution, which manifests itself as a Gaussian interference pattern. Diffusive is, however, not an adjective that is appropriate to describe Sr_2RuO_4 (N.B., the mean free path in the normal state is larger than the ring diameter). Nevertheless, we conclude from the phase diagram in Figure 7.3b that the domain walls are in the extended regime, implying no direct *line of sight* between the superconducting contacts. This indicates that a similar mechanism based on scattering on the edges of the ring is responsible for the Gaussian interference pattern.

---

[6] This is supported by the fact that different frequencies for different samples give a Shapiro response, although the sample geometry is very similar.

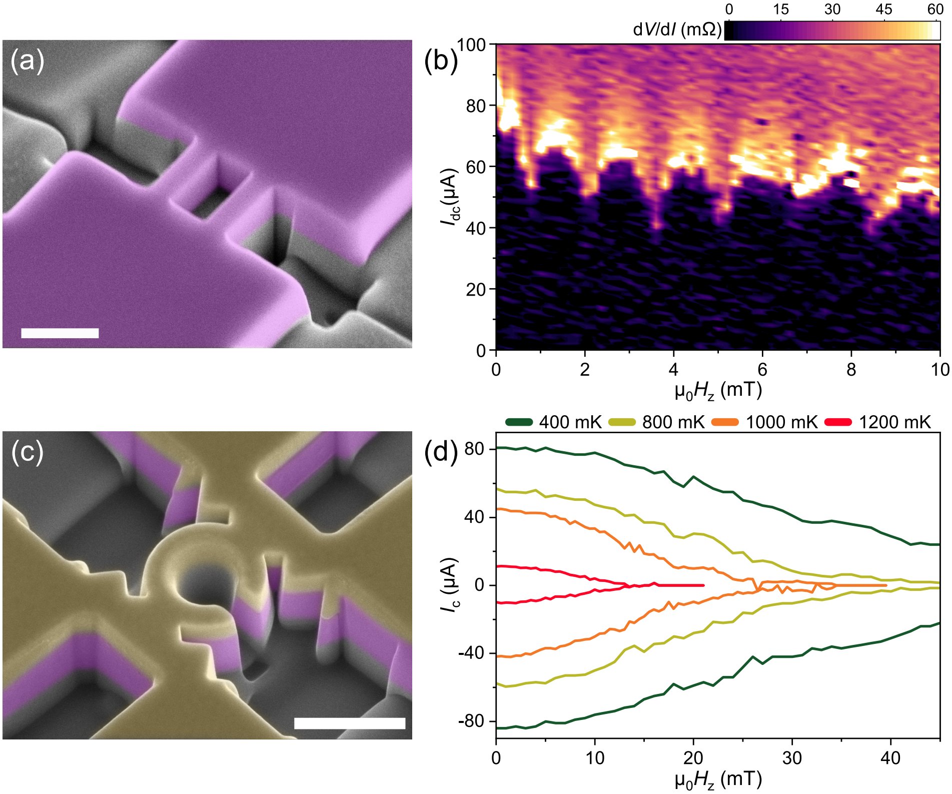

Figure 7.5: (a) a false colored scanning electron micrograph of a doubly connected straight bar sample, called Ring 3. Note that two large superconducting reservoirs form the contacts. Purple indicates the Sr_2RuO_4 crystal, the SiOx capping layer causes the dark contrast on top of the crystal, and the scale bar corresponds to 1 μm. (b) the $I_c(B)$-pattern, obtained on Ring 3 at 1 K. (c) depicts a false colored scanning electron micrograph of Ring 1 (also shown in Figure 7.3c), where we have cut one arm of the ring, transforming the sample to singly connected. The yellow top layer is the gold protective layer, and purple indicates the Sr_2RuO_4 crystal. The scale bar corresponds to 1 μm. In (d), we show the $I_c(B)$ patterns obtained on the sample shown in (c) for different temperatures. The critical current decreases monotonically as function of applied field.

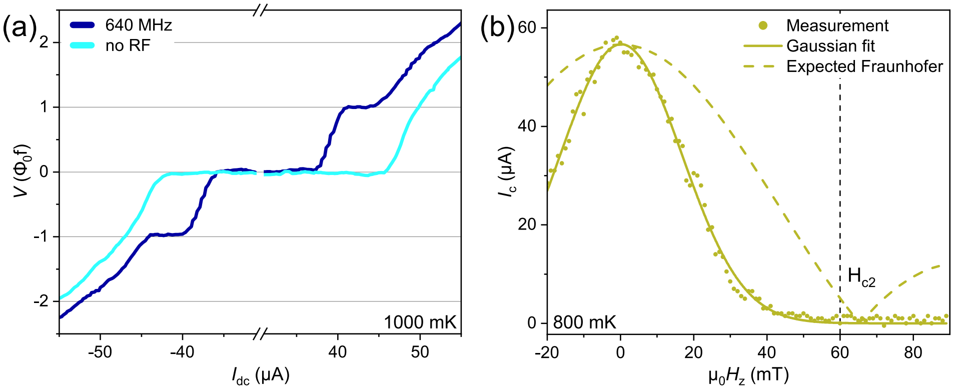

Figure 7.6: (a) Shapiro response of the single arm of Ring 1 (as shown in Figure 7.5c) obtained at 1 K. The voltage is normalized to the expected height of the Shapiro steps at 640 MHz. The Shapiro steps confirm the presence of a chiral domain wall. (b) $I_c(B)$ obtained on Ring 1 at 800 mK. The full circles correspond to the measured data, and the line is a Gaussian fit to the data. The dashed line is the expected Fraunhofer pattern, based on a single Josephson junction with an effective area given by the product of the coherence length and the width of the arm of the ring. The vertical reference line shows the upper critical field defined as $R(H_{c2}) = R_N$. As the chiral domain wall is in the extended regime, the Gaussian $I_c(B)$ can be caused by ballistic scattering processes on the bounds of the arm of the ring.

7.6. $I_c(T)$ OF A CHIRAL DOMAIN WALL JUNCTION

Besides the Shapiro response and the magnetic interference patterns, the temperature dependence of the critical current provides an additional tool to identify the presence of domain walls. In Figure 7.7a, we plot the I_cR_N product of three samples (containing chiral domain walls) with different geometry as a function of normalized temperature. We find that the critical current follows an exponential increase close to T_c, but at lower temperatures, it saturates and plateaus. More importantly, not only the temperature dependence but also the magnitude of I_cR_N is identical for all devices, despite the vastly different sample geometry. Note that we have independently established the presence of domain walls for all the three devices depicted in Figure 7.7a using other techniques (either by the detection of Shapiro steps or the detection of SQUID-like oscillations). From this analysis we conclude that $I_cR_N(T/T_c)$ is universal for chiral domain walls.

In contrast to samples that exhibit the presence of domain walls, devices that lack a chiral domain wall do not show a universal $I_cR_N(T/T_c)$. For example, the two I_cR_N-curves shown in Figure 7.7b. Instead of a exponential increase close to T_c, we observe a more bulk-like $(1-T/T_c)^{1/2}$ dependence.[7] Furthermore, the magnitude of the I_cR_N product is not sample-independent. Typically, the field dependence of the critical current of these samples is a monotonic linear decay, and Shapiro response lacked. In conclusion, the behavior of $I_cR_N(T/T_c)$ allows us to distinguish between samples that effectively pin a chiral domain wall and those that do not.

---

[7] In fact, this same behavior is found in the $I_cR_N(T)$ of the micrometer-sized contacts of samples that exhibit domain walls.

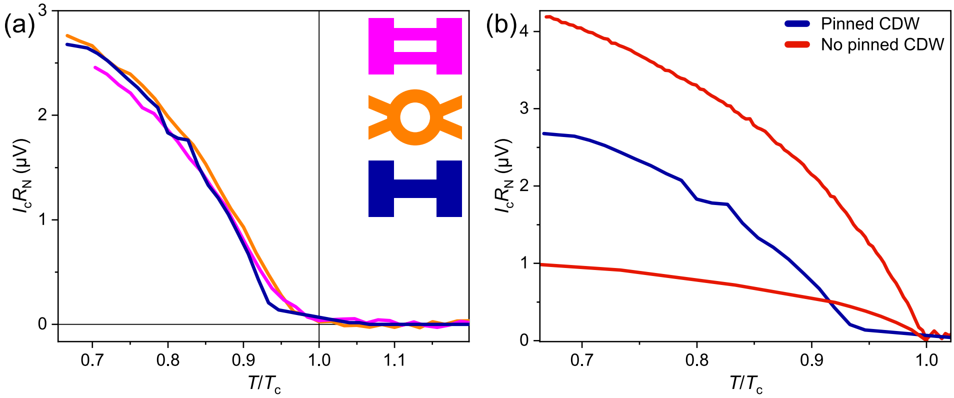

Figure 7.7: $I_cR_N(T/T_c)$ for two classes of samples. (a) samples that do pin chiral domain walls show a universal temperature dependence of I_cR_N, despite there vastly different sample geometry. Here the orange curve corresponds to Ring 2 (T_c = 1.2 K) and the magenta one corresponds to Ring 3 (T_c = 1.28 K). The bar (blue colored curve) has a critical temperature of 1.5 K. Note that not only the temperature dependence, but also the magnitude of I_cR_N is identical between the samples. As a sharp contrast to this behavior, we plot the $I_cR_N(T/T_c)$ of samples that do not exhibit chiral domain walls in (b) with red curves. Here the temperature dependence close to T_c is well captured by the more bulk-like $(1-T/T_c)^{1/2}$ dependence. Furthermore, the magnitude of I_cR_N differs between samples. As reference we plot the curve obtained on the bar sample from (a).

7.7. FIELD-INDUCED BISTABLE DOMAIN CONFIGURATIONS

By applying small in-plane magnetic fields, we found that we can decrease the pinning of the chiral domain walls, which manifests itself as a bistable I_c state controlled by the bias current polarity. This process is shown in Figure 7.8. We find that a high I_c (blue curve) and a low I_c (orange curve) state appears under the application of 20 mT along a line connecting the measurement leads (x-direction). We can switch between these states by applying either a large enough positive or negative current bias, which we denote by I_+ and I_- respectively (indicated by red circles in Figure 7.8). If the sample is in the low I_c configuration, it remains in the low I_c branch until we apply a current larger than I_+. upon passing $I > I_+$, the sample transitions to the high I_c branch, which can be identified by a hysteresis loop on the positive current polarity. The high I_c state is subsequently stable until a negative bias current of $I < I_-$ is applied. Consequently, the sample switches to the low critical current state, resulting in a hysteresis loop on the negative current polarity. Note that both I_c states are exceedingly stable: the hysteresis loops only appear accompanied by switching between the states. Therefore, it is impossible to observe a hysteresis loop multiple times on the same current polarity, making this behavior quite distinct from conventional hysteresis loops in underdamped junctions.

Having made the distinction from conventional hysteresis loops, we recognize that the bistability of I_c results in two hysteresis loops upon cycling the bias current between positive and negative directions (using currents $|I| > \max(I_-, I_+)$). In Figure 7.8, we ob-

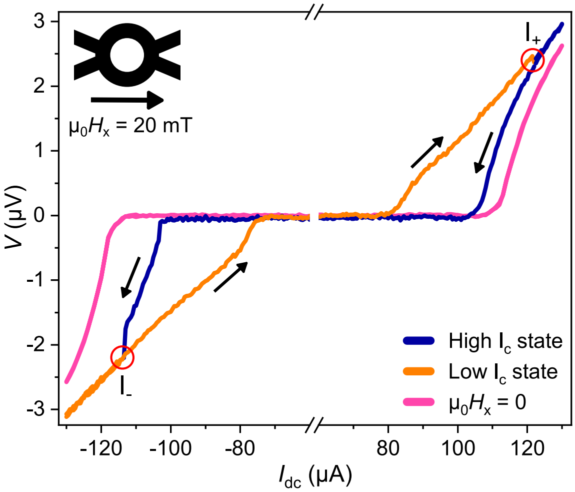

Figure 7.8: IV-characteristics obtained on Ring 2 at 600 mK, under the application of an in-plane field of 20 mT along the x-direction (line connecting the measurement leads attached to the ring). A two-level critical current state is revealed: the blue curve is the high I_c state, and in orange, we plot the low I_c state. As a reference, we show the IV-characteristic for zero field in pink. We can switch between these bistable states by applying high positive or negative bias currents. Specifically, by applying $I > I_+$ ($I_+ = 122$ µA, for Ring 2), the sample switches to the high I_c state. The reverse is true for a bias current of $I < I_-$ ($I_- = -114$ µA, for Ring 2). Both I_+ and I_- are indicated by red circles. Switching between the I_c states results in a hysteresis loop, the order of which is shown by the black arrows. The switching behavior is characterized by a hysteresis loop of normal order (critical current larger than the retrapping current) on the negative bias polarity and a hysteresis loop of the reversed order on the positive current polarity.

serve a critical current that exceeds the retrapping current when switching from the high I_c state to the low I_c state (on the negative current polarity). However, the reverse is true when switching from the low I_c state to the high I_c state (on the positive current polarity): the retrapping current is higher than the critical current. As this behavior is uncommon, we coin this the anomalous hysteresis polarity. Interestingly, when reversing the field direction, the polarity of the anomalous hysteresis changes sign, as shown in Figure 7.9. In other words, the role of I_+ and I_- in switching between the critical current states interchanges upon reversing the field direction. This is graphically summarized in Figure 7.10.

Before interpreting the bistability I_c property of these samples, first, some general remarks. Although Figures 7.8 and 7.9 are results obtained on ring-shaped devices, we observed this behavior in all samples that pin chiral domain walls, irrespective of curvature or whether they contain singly or doubly connected geometries. Besides, field cooling or applying the field after cooling the sample is cooled below T_c gave identical results. On the other hand, we find that the direction and magnitude of the in-plane magnetic field, required to obtain this behavior, is sample dependent. For example, Ring 1 (Figure 7.3c) showed the bistability of I_c at an in-plane field of 15 mT applied 55 degrees with respect to the x-direction.[8] For a more detailed discussion, the reader is

---

[8] Here the x-direction is defined as *along the ring*; see the inset of Figure 7.8

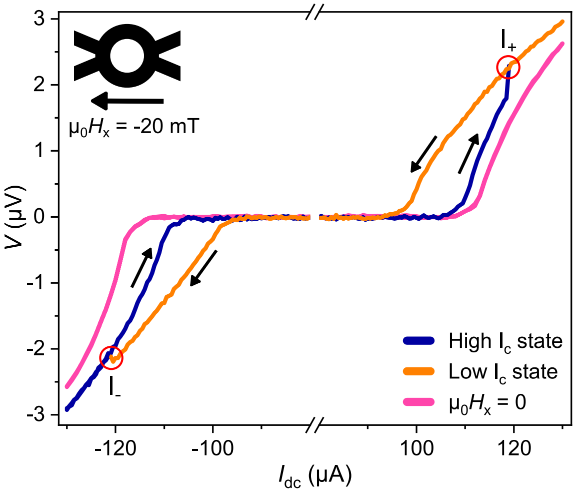

Figure 7.9: Measurements analogous to those presented in Figure 7.8, where the in-plane field direction is reversed. All indicators and symbols are as defined in Figure 7.8 and the data is acquired on Ring 2 at 600 mK. Note that reversing the field direction along the ring, results in an exchange of the role of I_+ and I_- in switching between the critical current states. In other words, the anomalous hysteresis is observed on the negative bias polarity. The values of I_+ and I_- are 119 μA and -121.5 μA respectively.

referred to Appendix B. Note that the magnitude of the field that triggers the bistability is below H_{c1} and can therefore not be caused by in-plane Abrikosov vortices that are mobile in the sample. Finally, this rather unusual switching property cannot be caused by any conventional constriction-type junctions reviewed in section 7.3. Its detection, therefore, reinforces the hypothesis that the spontaneous Josephson coupling in these mesoscopic devices is caused by the presence of superconducting chiral domain walls.

In order to interpret the bistable I_c of our samples, we turn to two key literature results that showed the presence of mobile chiral domain walls. Kidwingira et al. first found evidence of telegraph noise near the critical current of corner junctions on macroscopic crystals of Sr_2RuO_4, which they interpreted as the movement of chiral domain walls[42]. Similarly, Anwar et al. studied Sr_2RuO_4 hybrid junctions between niobium and Sr_2RuO_4 (coupled by a Ru-inclusion to the Sr_2RuO_4 crystal) and found similar hysteresis loops as presented here, along with the aforementioned telegraph noise near I_c (see Figure 7.11a)[43]. Moreover, Anwar et al. found that the application of small fields in the ab-plane increases the telegraph noise near I_c, which indicates that the domain walls become less strongly pinned due to the in-plane fields (see Figure 7.11b). Most likely, the two-level I_c property shares its origins with the telegraph noise observed on macroscopic samples. Both Kidwingira et al. and Anwar et al. discuss macroscopic devices that do not pin domain walls due to the sample size. However, here we study confined structures exhibiting stronger pinning, and therefore the domain configuration is more stable. However, the application of in-plane fields decreases the domain wall pinning, which consequently leads to the appearance of a bistable domain configura-

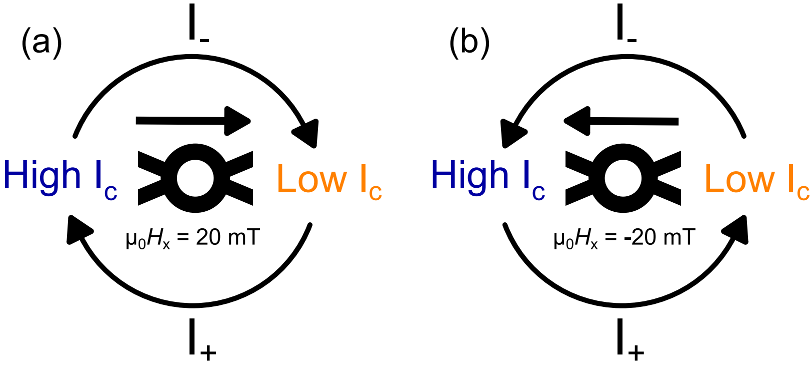

Figure 7.10: Schematic of the interplay between field direction, I_+ and I_- in determining the low or high I_c state in ring structures of Sr_2RuO_4 as revealed under the application of in-plane fields. (a) and (b) correspond to the results presented in Figure 7.8 and 7.9 respectively. The color coding of the high and low critical current states corresponds to the curve color in the IV-characteristics of Figure 7.8 and 7.9. As evidenced by the difference between (a) and (b), reversing the field direction, interchanges the role of I_+ and I_- in changing between the two different I_x states.

tion. In turn, a different domain configuration can lead to a different I_c; the application of an in-plane magnetic field can lead to a bistable I_c in our mesoscopic devices[52]. Not only fields can move the domain walls: as evidenced by the telegraph noise near I_c the bias current also couples to the domain configuration. This explains the influence of I_+ and I_- in switching between the two I_c states. Moreover, if both an electrical current and an in-plane magnetic field can exert a torque on the domain wall, it explains why reversing the field direction interchanges how I_+ and I_- determine the low or high I_c state.

There are, however, also some open questions that remain. First and foremost, how the domain structure is influenced under in-plane fields is not known. More specifically, what is not known is the direction of the lattice vectors with respect to the applied magnetic field, and therefore the possible importance of field-to-lattice alignment. In Appendix C we present, as an outlook, an experiment that determines the a- and b-axis in a mesoscopic device in situ. Secondly, the results presented here raise the question of how a charge current couples to the chiral domain walls and why chiral domain walls can become unpinned by the application of in-plane fields. Thirdly, it must be noted that magnetic fields of the same magnitude were used in the magnetometry experiments that revealed the presence of half-quantum vortices in mesoscopic rings of Sr_2RuO_4[19]. This calls for a reexamination of these results and a possible reinterpretation based on chiral domain walls present in these rings.

Finally, these domain wall junctions can function as superconducting memory elements. Analogous to the devices presented in Chapter 5, we can specify a read-out current between the critical current of the low I_c branch and I_+. This leads to a finite voltage in the low I_c state, whereas a zero voltage in the high I_c state. It is advantageous that the bias current polarity controls the writing procedure of such memory instead of applying a magnetic field. On the other hand, the memory of our rings is limited by the need for finite static magnetic fields and sub-1.5K temperatures. Besides, chiral domain walls can never form non-volatile memories, as they are tied to the superconducting phase.

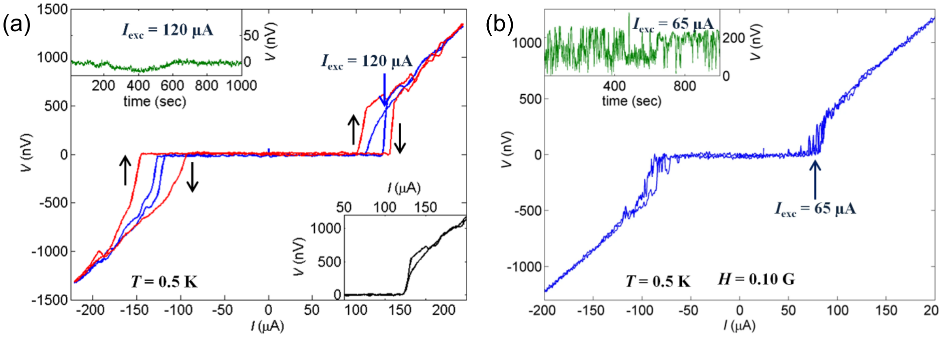

Figure 7.11: Two examples of multistable I_c states, taken from Anwar et al[43]. In (a), there is a clear bistable behavior, with an anomalous hysteresis on the positive current bias and a regular hysteresis loop on the negative bias, comparable to the data in Figure 7.8. As this concerns a macroscopic crystal, the chiral domain walls are pinned less. Therefore, switching between chiral domain configurations does not require the application of in-plane fields. Moreover, the IV-characteristic can be altered between different cooling cycles, indicating a non-deterministic domain configuration when entering the superconducting state. When small magnetic fields are applied in the ab-plane (0.01 mT), the pinning of chiral domain walls decreases, and the domains reconfigure without applying currents larger than I_+ or I_-, resulting in large amounts of telegraph noise near I_c.

7.8. ALTERING THE PERIODICITY OF CURRENT-PHASE RELATION WITH IN-PLANE MAGNETIC FIELDS

Besides a current switchable bistable I_c state, in-plane fields can alter the periodicity of the current-phase relation associated with the domain wall junctions. We found that some combinations of field magnitude and alignment can give rise to clear half-integer Shapiro steps, which indicates a current-phase relation that is π-periodic instead of 2π-periodic. For example, in Figure 7.12a, we plot both I_c states of Ring 4, corresponding to the application of a 10 mT field along the x-direction. We find the bistable I_c states where the high I_c branch shows only an integer Shapiro response, whereas the low I_c branch shows both integer and half-integer steps. This suggests that the two I_c states have different current-phase relations. Upon resetting the field (i.e., diminishing the field to zero and subsequently reapplying the original field), we find that the domain composition is reconfigured (see Figure 7.12). This results in a missing first Shapiro step on the positive current polarity, and on the reverse sweep, after switching to the low I_c state, the appearance of half-integer steps, where the first half step is missing. Furthermore, the half-integer Shapiro response seems limited to one current polarity. Although we did not find a direct correlation between the occurrence of the anomalous hysteresis loop and the non-integer steps, reversing the field direction changes the po-

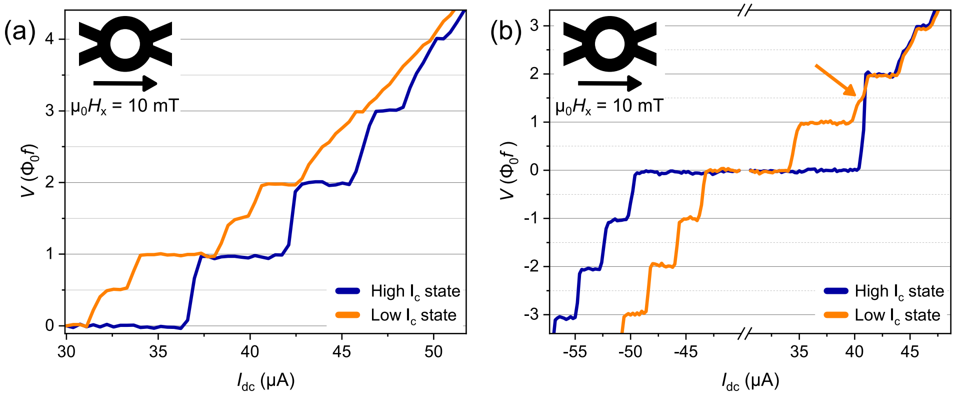

Figure 7.12: IV-characteristics acquired under simultaneous radiation of microwaves (145 MHz) and the application of an in-plane field of 10 mT along the x-direction on Ring 4 at 50 mK. In (a), we observe the unmistakable appearance of half-integer Shapiro steps in the low I_c state. However, the high I_c state only shows an integer Shapiro response, indicating an altered current-phase relation between the I_c states. After resetting the field (i.e., setting the field to zero and subsequently reapplying the same field), we only find integer Shapiro steps on the negative current polarity. The first step is lacking on the positive bias polarity; only in the low I_c state do we observe a half-integer Shapiro step, indicated by the yellow arrow..

larity at which we observe the fractional steps. Therefore, most likely, there is a relation between the multistable I_c states and the appearance of the fractional Shapiro steps: both properties require similar in-plane fields, and the exact magnitude or orientation seems to vary between samples. Moreover, there seems to be no correspondence between the geometry of the sample and the field direction required to trigger either the two-level I_c property or the non-integer Shapiro steps.

To examine the origin of the fractional Shapiro steps, we perform a magnetic field sweep under microwave radiation (see Figure 7.13). Before this experiment, we verified a reproducible half-integer Shapiro response at finite in-plane fields. We observe a Fraunhofer-like interference pattern with Shapiro steps close to I_c. In Figure 7.13b,c we plot IV-characteristics at specific fields, extracted from Figure 7.13a. Interestingly, $\frac{1}{3}$-fractional Shapiro steps appear near the minima of the interference pattern (i.e., 4.5 mT and 9.9 mT). Naturally, at these minima, the first harmonic of the current-phase relation is suppressed, and therefore it can be dominated by the higher harmonics. This effect is commonly observed in, for example, $0-\pi$ transitions in SF-hybrid junctions[53, 54]. Beyond 15 mT, however, there seem to be no oscillations in the $I_c(B)$-pattern. In this regime, we see the appearance of the half-integer steps, which might be distinguished from the trivial fractional steps observed in the minima of $I_c(B)$. At even higher magnetic fields, the half-integer steps disappear, and only integer steps are observed. Besides, integer steps are observed between the minima in the oscillatory part of the $I_c(B)$-pattern.

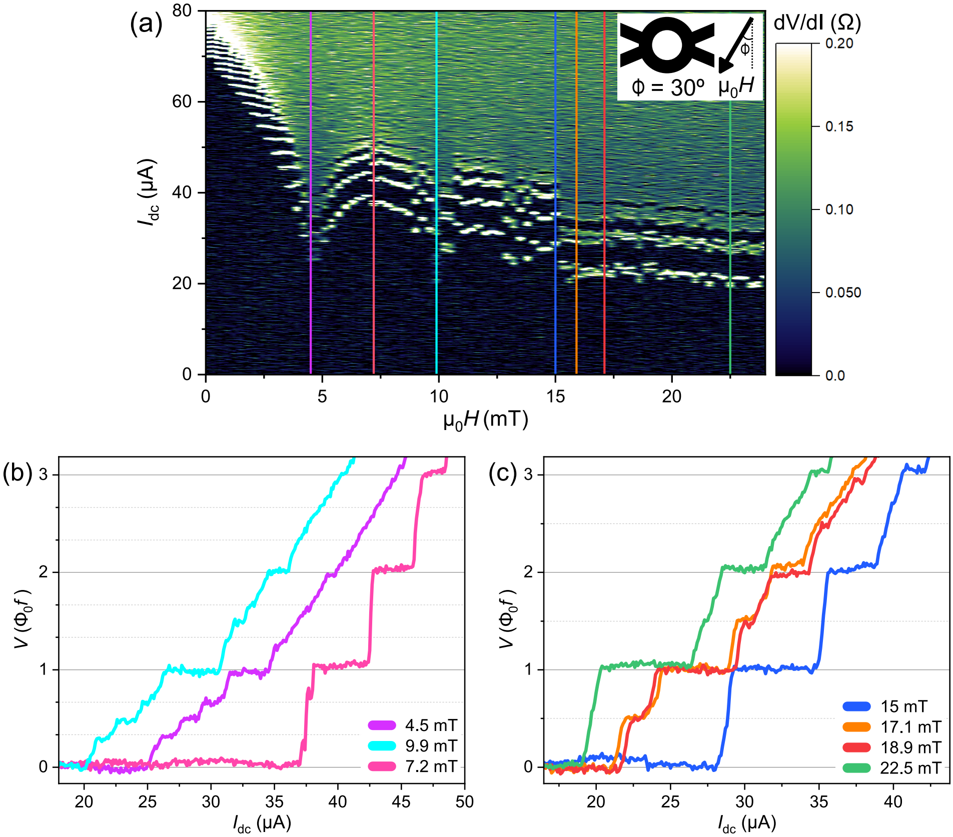

Figure 7.13: (a) In-plane magnetic field sweep obtained on Ring 4, under the application of microwaves (145 MHz) at 50 mK. There is a 30 degree angle between the y-axis and the magnetic field direction (see inset). To erase any field history, we reduce the field to zero between each field step and we cycle both current polarities twice at each field. In (a) we plot the up-sweep of the second cycle (i.e., increasing current direction). (b) and (c) show IV-characteristics extracted from (a). The color coding of the vertical reference lines corresponds to the color of the curves in (b) and (c).

The period of the oscillations in $I_c(B)$, combined with the thickness of the crystal, implies a junction length of 1.5 μm, which exceeds the outer diameter of the ring of 1 μm. This is not expected since the interference pattern is obtained at 50 mK. No extended domain wall regime is expected at these temperatures and sample dimensions, according to the time-dependent Ginzburg-Landau simulations. Furthermore, in-plane magnetic field sweeps obtained on other ring samples never exhibited a Fraunhofer-like pattern but rather a monotonic decay. The interference pattern presented in Figure 7.13a, therefore, raises the question of what the junction geometry is and how it is related to the domain wall structure. The interference pattern also seems to suggest that the $\frac{1}{3}$-fractional Shapiro steps result from a trivial process. On the other hand, since they are stable over a larger field range, the half-integer Shapiro response might be the consequence of a more profound effect of the presence of in-plane fields.

7.9. IMPLICATIONS FOR THE PAIRING SYMMETRY

As mentioned in the introduction, the chiral p-wave pairing paradigm became problematic in recent years due to multiple revisited experiments, and today the proposals range far and wide. This section will try to reconcile our experiments with one of those proposals.

Since the discovery of SQUID-like oscillations in homogeneous rings of Sr_2RuO_4 reported in [6], and their attribution to chiral domain walls, we have studied numerous properties of these remarkable junctions. To explicitly name them: the temperature dependence associated with the trapping of a domain wall, which is sample independent; the influence of geometry on the domain structure; the bistability of chiral domain walls by the application of in-plane magnetic fields, and the alteration of the periodicity of the current-phase relation due to said in-plane fields. Before continuing the discussion of the consequences of these observations, we conclude that these unusual properties can never occur in regular constriction type junctions nor as a result of persistent currents. Therefore, the experiments presented in this chapter form a compelling collection of evidence for the existence of superconducting domains in Sr_2RuO_4.

Chiral p-wave superconductivity is one of the least complex symmetries featuring the spontaneous appearance of superconducting domains. However, since chiral p-wave pairing has become an unlikely candidate for describing the pairing in Sr_2RuO_4, we require an alternative featuring such domains. Naturally, any chiral order parameter satisfies this need. Alternatively, as mentioned in section 7.2.2, there is a proposed class of superconducting pairings composed of two single-component order parameters. Although these order parameters can also break up into superconducting domains, this does not happen spontaneously. Instead, a varying strain texture caused by dislocations and impurities is required for the stabilization of the domain walls[40, 55]. Not only is this scenario opposed by our evidence of clean and strain-free crystals, it also suggests that the domains are set by the lattice and therefore are not mobile, which is directly contradicted by our in-plane field experiments. On the other hand, a symmetry-protected chiral pairing allows for mobile domains. Therefore, chiral d-wave is a more likely candidate based on our experiments.

In section 7.2.2 we noted two arguments countering the chiral d-wave picture. First is the observation of vertical line nodes, which seems to conflict with chiral d-wave pairing, for which horizontal line nodes are expected[28]. However, taking into account spin-orbit coupling and inter-layer interactions (as opposed to a more simple two-dimensional model), it was shown that a chiral d-wave superconductor can exhibit quasi-particle Fermi surfaces, which can appear as vertical line-nodes in experiments[56, 57]. The missing second transition in heat capacity measurements poses a bigger problem, which, up to now, remains unresolved[29].

7.10. CONCLUSION AND OUTLOOK

We have studied the properties of mesoscopic structures of Sr_2RuO_4 in various singly and doubly connected microstructures and found the spontaneous emergence of Josephson junctions, independent of the sample geometry in the superconducting phase. This is supported by the measurement of the $I_c(B)$-pattern, as well as a clear Shapiro response. Furthermore, we find that the I_cR_N product displays a universal temperature dependence, regardless of device geometry. Under the application of in-plane fields, a bistable critical current emerges, characterized by a low I_c and a high I_c state that can be switched by the application of electrical current. Besides, in-plane fields alter the periodicity of the current-phase relation of the spontaneous junctions, which is reflected by the appearance of half-integer steps in the Shapiro response. Combining these unusual observations provides compelling evidence for the presence of superconducting domains in Sr_2RuO_4. Naturally, a chiral order parameter can feature such domains, and in light of the recent experimental work detailing the pairing symmetry of Sr_2RuO_4, a chiral d-wave order parameter of the form $d_{xz} \pm i d_{yz}$, is, therefore, the most promising candidate.

The experiments presented in this chapter raise plenty of questions as well. For example, why are the domain walls more mobile under the application of in-plane fields, and what determines their interaction with charge current? Besides, what determines the direction and magnitude of the in-plane magnetic fields required to produce the bistable I_c and likewise the half-integer Shapiro response? Finally, how are these effects related to the alignment of the crystalline axes? These questions remain unanswered. Besides, there remain multiple apparent contradictory results in literature. Therefore, further experiments are necessary.

APPENDICES

A. SAMPLE DIMENSIONS OF RING SAMPLES

In this Appendix, we provide an overview of the length parameters of the different samples used to obtain the data in this chapter. They are summarized in Table 7.1. Note that the behavior reported on each sample is not exclusive to that specific device. Besides, some of the data is not acquired in the Vectormagnet (see Appendix A of Chapter 2) but at Twente university in a dilution refrigerator capable of reaching 10 mK base temperatures. The data shown in Figures 7.4, 7.12, 7.13, B.1, and B.2 are obtained using a Stanford Research Instruments SR830 lock-in in Twente using a similar method as described in Appendix A of Chapter 2.

B. STABILITY OF CHIRAL DOMAIN WALLS UNDER IN-PLANE FIELDS

Although the mobile domain walls and their associated bistability of the critical current are observed universally in all samples, the direction and magnitude of the in-plane field required to trigger this behavior vary between samples. This Appendix presents an extensive search for the I_c bistability in the in-plane field parameter space obtained on two different ring samples.

In order to quantify the amount of hysteresis in an IV-characteristic, which accompanies switching between different I_c states, we define a parameter that measures the absolute voltage difference between the low I_c state and the high I_c state. We calculate this parameter by summing the absolute voltage difference between the two states at each current:

Sample name	D_{in}	D_{out}	t	Comments
Ring 1	0.608 µm	1.20 µm	0.450 µm	This sample is shown in the false colored scanning electron micrographs of Figure 7.3c and Figure 7.5c. It has a thick conducting gold capping layer. It is used to obtain the interference patterns depicted in Figure 7.3d, Figure 7.5d and 7.6.
Ring 2	0.531 µm	1.26 µm	0.7 µm	Sample presented in reference [6] as 'Exp. sample B' (see Figure 1d in ref. [6] for an scanning electron micrograph). The geometry of this sample is very close to Ring 1. We obtained the data presented in section 7.7 on this sample as well as $I_c(T)$ data.
Ring 3	0.475 µm	1.38 µm	0.589 µm	This is the doubly connected bar sample shown in the false colored scanning electron micrograph of Figure 7.5a. The sample is composed of two 1 µm long bars; here, the inner diameter references the distance between the bars, and the outer diameter is the total width of the sample (i.e., the inner diameter plus the width of both bars). This sample provided the data for the $I_c(T)$ and the interference pattern in Figure 7.5b.
Ring 4	0.486 µm	1.01 µm	0.253 µm	This sample is shown in the false colored scanning electron micrograph of Figure C.1b. The ring part of the sample is used to obtain the Shapiro step results presented in Figure 7.4, 7.12 and 7.13. Besides, we studied the stability of the critical current state switching on this sample (i.e., Figure B.2).

Table 7.1: Table containing the dimensions (inner diameter D_{in}, outer diameter D_{out} and the thickness t) and other details of the ring samples used acquire the data presented in this chapter.

$$\text{Hyst.} = \sum_{I_i} |V(I_i \rightarrow) - V(I_i \leftarrow)| \tag{7.1}$$

Here we sum over each current probed in the IV-characteristic, $V(I_i \rightarrow)$ is the voltage measured during the forward sweep, and $V(I_i \leftarrow)$ the voltage measured on the reverse sweep. Naturally, this parameter gives a measure for the surface enclosed by the hysteresis loops: it is zero if there is no hysteresis and finite if any hysteresis exists between the current and retrapping current. In Figure B.1 we plot the hysteresis parameter for a large combination of field magnitudes and directions. Here ϕ is the polar angle in the xy-plane, and $\phi = 0$ corresponds to the direction along the ring, as defined in the inset of Figure 7.8. We find $\phi = 20$ degrees the optimal angle to produce the switching behavior reported in section 7.7.

In Figure B.2a, we present a measurement of the same hysteresis parameter for Ring 4, which does not have any preferential angle along which it produces the bistable I_c states. Moreover, we have obtained the IV-characteristic at each field twice, which allows us to examine the reproducibility of the hysteresis parameter at a constant magnetic field (see Figure B.2b). From the difference between Figure B.2a and B.2b, we can conclude that this sample pins chiral domain walls less effectively than other samples. Note that this does not mean the sample can be regarded as irregular, as it showed a

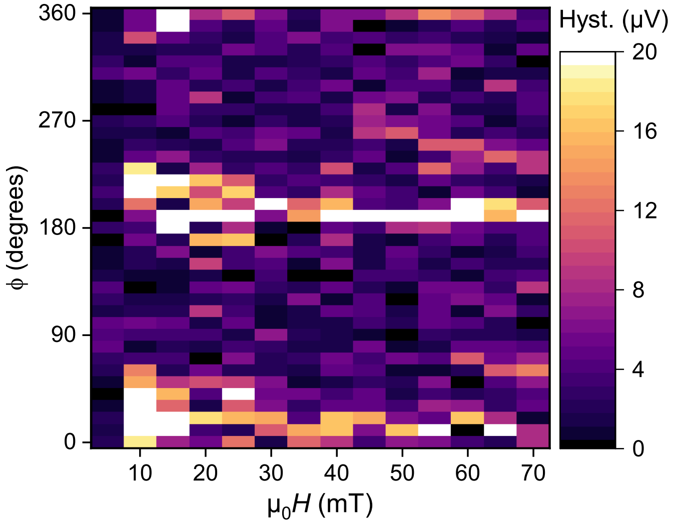

Figure B.1: Hysteresis parameter (summed difference between the high I_c state and the low I_c state) extracted for different combinations of field magnitude and direction. Note that each pixel represents a single IV-characteristic. Here ϕ is the polar angle in the xy-plane (with the x direction along the ring, as defined in Figure 7.8). At $\phi = 20$ degrees we find clear hysteresis behavior, indicating switching between different I_c states (i.e., mobile domain walls). Before setting each field and starting the IV-measurement, the field was reduced to zero.

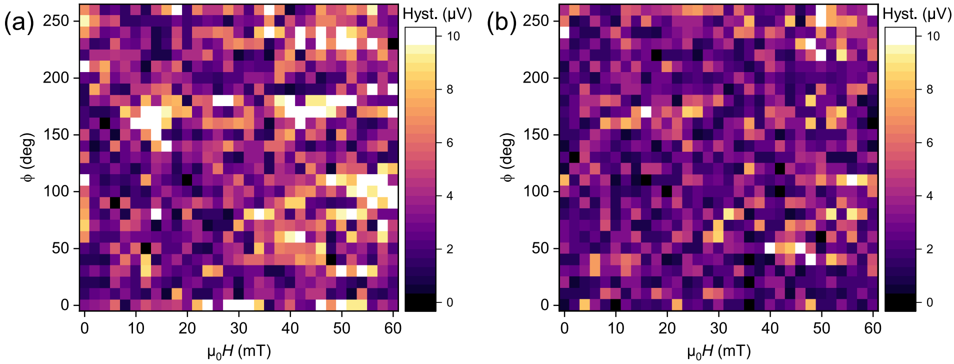

Figure B.2: (a) The same quantity measured as presented in Figure B.1 for Ring 4. The same measurement protocol was used to acquire the data. However, the IV-characteristic was measured twice at each field. In (b), we plot the hysteresis parameter obtained from the second IV-characteristic. This sample does not have a preferred field direction that triggers the mobile domain regime. Besides, this sample pins the chiral domain walls less effectively, which can be seen from the difference between (a) and (b): the hysteresis loops are less reproducible.

clear SQUID-like interference pattern and Shapiro response.

C. PROPOSED EXPERIMENT TO ESTABLISH A- AND B-AXIS IN SITU

Since we found no correlation between the geometry of the samples and the field alignments that trigger the critical current bistability, comparing the relative field directions to the orientation of the atomic lattice would provide valuable insight into the underlying mechanism. There might be a relation to the nematicity of the electronic system found in the normal state of Sr_2RuO_4 [58], if there is no correlation with the atomic lattice. As an outlook, we provide an experiment, that can establish the direction of the a- and b-axis of the crystal flake in situ.

Crucial to this proposal is the observation of an anisotropy in the upper critical field in the ab-plane of Sr_2RuO_4 (see Figure C.1a) [59]. During this experiment, the orientation of the lattice was established first, and the anisotropy was measured. We propose to utilize the reverse: measure the anisotropy in H_{c2} and infer the direction of the principle axes from this measurement using the results presented in reference [59]. Figure C.1b depicts a sample shaped into a multiple micrometer-sized bar attached to a ring with a diameter of 1 μm. Using contacts V_1 and V_2, we can measure the voltage over the bar, which does not pin chiral domain walls due to its relatively large size. Therefore we can assess the anisotropy in H_{c2} and establish the crystalline axes of the flake. Since there is a fixed orientation between the bar and the ring, this information transfers to the ring. Next, we can switch our voltage measurement to contacts V_2 and V_3, which measure the voltage over the ring, allowing us to repeat the experiments using in-plane fields and relate them to the crystalline lattice.

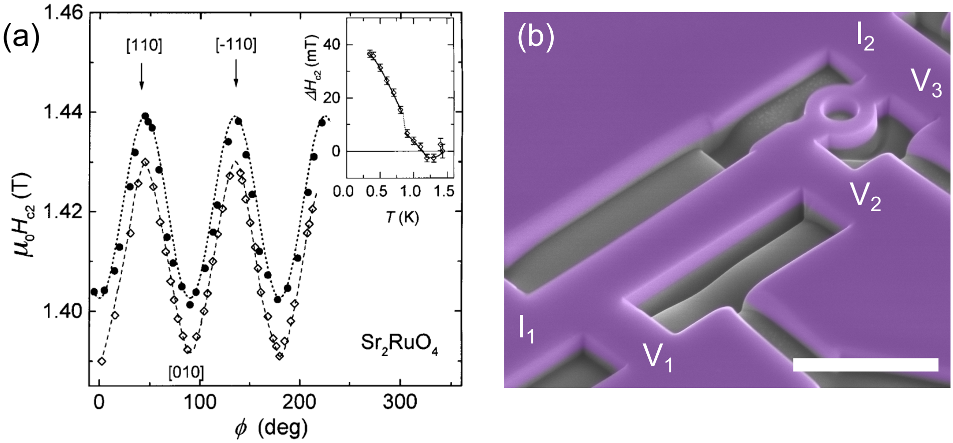

Figure C.1: (a) the upper critical field of Sr$_2$RuO$_4$ in the ab-plane as a function of the polar angle between the field direction and the a-axis, taken from reference [59]. Using this result, we can infer the crystalline axes by measuring the anisotropy in H_{c2}. (b) false colored scanning electron micrograph of a sample that can be employed to carry out the proposed experiment. Current is applied between the contacts labeled with I$_1$ and I$_2$. The bar part of this sample (between voltage contacts V$_1$ and V$_2$) is relatively large and therefore does not pin chiral domain walls. We can use the bar to measure the anisotropy in H_{c2}, which then provides information about the crystalline axes of both the bar and the ring (experimentally accessible using contacts V$_2$ and V$_3$). The scale bar corresponds to 2 μm; this sample was used to obtain the Shapiro data presented in the main text.

References

[1] Hardy, W. N., Bonn, D. A., Morgan, D. C., Liang, R. & Zhang, K. Precision measurements of the temperature dependence of λ in YBa$_2$Cu$_3$O$_{6.95}$: Strong evidence for nodes in the gap function. *Phys. Rev. Lett.* **70**, 3999–4002 (1993).

[2] Wollman, D. A., Van Harlingen, D. J., Lee, W. C., Ginsberg, D. M. & Leggett, A. J. Experimental determination of the superconducting pairing state in YBCO from the phase coherence of YBCO-Pb dc SQUIDs. *Phys. Rev. Lett.* **71**, 2134–2137 (1993).

[3] Tsuei, C. C. *et al.* Pairing symmetry and flux quantization in a tricrystal superconducting ring of YBa$_2$Cu$_3$O$_{7-\delta}$. *Phys. Rev. Lett.* **73**, 593–596 (1994).

[4] Bednorz, J. G. & Müller, K. A. Possible high T_c superconductivity in the Ba−La−Cu−O system. *Z. Phys. B Con. Mat.* **64**, 189–193 (1986).

[5] Sigrist, M. & Agterberg, D. F. The role of domain walls on the vortex creep dynamics in unconventional superconductors. *Progr. Theor. Phys.* **102**, 965–981 (1999).

[6] Yasui, Y. *et al.* Spontaneous emergence of Josephson junctions in homogeneous rings of single-crystal Sr$_2$RuO$_4$. *npj Quantum Mater.* **5**, 21 (2020).

[7] Maeno, Y. *et al.* Superconductivity in a layered perovskite without copper. *Nature* **372**, 532–534 (1994).

[8] Mackenzie, A. P. *et al.* Extremely Strong Dependence of Superconductivity on Disorder in Sr_2RuO_4. *Phys. Rev. Lett.* **80**, 161–164 (1998).

[9] Rice, T. M. & Sigrist, M. Sr_2RuO_4: an electronic analogue of ^{3}He? *J. Phys.: Condens. Matter* **7**, L648 (1995).

[10] Rice, M. An analogue of superfluid ^{3}He. *Nature* **396**, 627–628 (1998).

[11] Maeno, Y., Kittaka, S., Nomura, T., Yonezawa, S. & Ishida, K. Evaluation of spin-triplet superconductivity in Sr_2RuO_4. *J. Phys. Soc. Japan* **81**, 1–29 (2012).

[12] Mackenzie, A. P., Scaffidi, T., Hicks, C. W. & Maeno, Y. Even odder after twenty-three years: The superconducting order parameter puzzle of Sr_2RuO_4. *npj Quantum Mater.* **2**, 40 (2017).

[13] Time-reversal symmetry-breaking superconductivity in Sr_2RuO_4. *Nature* **394**, 558–561 (1998).

[14] Xia, J., Maeno, Y., Beyersdorf, P. T., Fejer, M. M. & Kapitulnik, A. High resolution polar kerr effect measurements of Sr_2RuO_4: evidence for broken time-reversal symmetry in the superconducting state. *Phys. Rev. Lett.* **97**, 167002 (2006).

[15] Luke, G. *et al.* Unconventional superconductivity in Sr_2RuO_4. *Phys. B: Condens. Matter* **289-290**, 373–376 (2000).

[16] Sigrist, M. & Ueda, K. Phenomenological theory of unconventional superconductivity. *Rev. Mod. Phys.* **63**, 239–311 (1991).

[17] Ishida, K. *et al.* Spin-triplet superconductivity in Sr_2RuO_4 identified by ^{17}O Knight shift. *Nature* **396**, 658–660 (1998).

[18] Duffy, J. A. *et al.* Polarized-Neutron Scattering Study of the Cooper-Pair Moment in Sr_2RuO_4. *Phys. Rev. Lett.* **85**, 5412–5415 (2000).

[19] Jang, J. *et al.* Observation of half-height magnetization steps in Sr_2RuO_4. *Science* **331**, 186–188 (2011).

[20] Deguchi, K., A. Tanatar, M., Mao, Z., Ishiguro, T. & Maeno, Y. Superconducting double transition and the upper critical field limit of Sr_2RuO_4 in parallel magnetic fields. *J. Phys. Soc. Japan* **71**, 2839–2842 (2002).

[21] Clogston, A. M. Upper limit for the critical field in hard superconductors. *Phys. Rev. Lett.* **9**, 266–267 (1962).

[22] Hicks, C. W. *et al.* Limits on superconductivity-related magnetization in Sr_2RuO_4 and $PrOs_4Sb_{12}$ from scanning SQUID microscopy. *Phys. Rev. B* **81**, 214501 (2010).

[23] Pustogow, A. *et al.* Constraints on the superconducting order parameter in Sr_2RuO_4 from oxygen-17 nuclear magnetic resonance. *Nature* **574**, 72–75 (2019).

7

[24] Ishida, K., Manago, M., Kinjo, K. & Maeno, Y. Reduction of the ^{17}O Knight shift in the superconducting state and the heat-up effect by NMR pulses on Sr_2RuO_4. *J. Phys. Soc. Japan* **89**, 034712 (2020).

[25] Petsch, A. N. *et al.* Reduction of the spin susceptibility in the superconducting state of Sr_2RuO_4 observed by polarized neutron scattering. *Phys. Rev. Lett.* **125**, 217004 (2020).

[26] Grinenko, V. *et al.* Split superconducting and time-reversal symmetry-breaking transitions in Sr_2RuO_4 under stress. *Nat. Phys.* **17**, 748–754 (2021).

[27] Steppke, A. *et al.* Strong peak in Tc of Sr_2RuO_4 under uniaxial pressure. *Science* **355** (2017).

[28] Hassinger, E. *et al.* Vertical line nodes in the superconducting gap structure of Sr_2RuO_4. *Phys. Rev. X* **7**, 011032 (2017).

[29] Li, Y.-S. *et al.* High-sensitivity heat-capacity measurements on Sr_2RuO_4 under uniaxial pressure. *Proc. Natl. Acad. Sci. U.S.A.* **118**, e2020492118 (2021).

[30] Agterberg, D. F. The symmetry of superconducting Sr_2RuO_4. *Nat. Phys.* **17**, 169–170 (2020).

[31] Rømer, A. T., Hirschfeld, P. J. & Andersen, B. M. Superconducting state of Sr_2RuO_4 in the presence of longer-range Coulomb interactions. *Phys. Rev. B* **104**, 064507 (2021).

[32] Scaffidi, T. Degeneracy between even- and odd-parity superconductivity in the quasi-1D Hubbard model and implications for Sr_2RuO_4 (2020). Preprint at https://arxiv.org/abs/2007.13769.

[33] Kivelson, S. A., Yuan, A. C., Ramshaw, B. J. & Thomale, R. A proposal for reconciling diverse experiments on the superconducting state in Sr_2RuO_4. *npj Quantum Mater.* **5**, 43 (2020).

[34] Clepkens, J., Lindquist, A. W. & Kee, H.-Y. Shadowed triplet pairings in hund's metals with spin-orbit coupling. *Phys. Rev. Research* **3**, 013001 (2021).

[35] Clepkens, J., Lindquist, A. W., Liu, X. & Kee, H.-Y. Higher angular momentum pairings in interorbital shadowed-triplet superconductors: Application to Sr_2RuO_4. *Phys. Rev. B* **104**, 104512 (2021).

[36] Ghosh, S. *et al.* Thermodynamic evidence for a two-component superconducting order parameter in Sr_2RuO_4. *Nat. Phys.* **17**, 199–204 (2021).

[37] Benhabib, S. *et al.* Ultrasound evidence for a two-component superconducting order parameter in Sr_2RuO_4. *Nat. Phys.* **17**, 194–198 (2021).

[38] Watson, C. A., Gibbs, A. S., Mackenzie, A. P., Hicks, C. W. & Moler, K. A. Micron-scale measurements of low anisotropic strain response of local T_c in $\mathrm{Sr_2RuO_4}$. *Phys. Rev. B* **98**, 094521 (2018).

[39] Grinenko, V. *et al.* Unsplit superconducting and time reversal symmetry breaking transitions in $\mathrm{Sr_2RuO_4}$ under hydrostatic pressure and disorder. *Nat. Commun.* **12** (2021).

[40] Yuan, A. C., Berg, E. & Kivelson, S. A. Strain-induced time reversal breaking and half quantum vortices near a putative superconducting tetracritical point in $\mathrm{Sr_2RuO_4}$. *Phys. Rev. B* **104**, 054518 (2021).

[41] Anwar, M. S. *et al.* Observation of superconducting gap spectra of long-range proximity effect in $\mathrm{Au/SrTiO_3/Sr_1RuO_3/Sr_2RuO_4}$ tunnel junctions. *Phys. Rev. B* **100**, 024516 (2019).

[42] Kidwingira, F., Strand, J. D., Harlingen, D. J. V. & Maeno, Y. Parameter domains in $\mathrm{Sr_2RuO_4}$. *Science* **314**, 1267–1271 (2006).

[43] Anwar, M. S. *et al.* Anomalous switching in $\mathrm{Nb/Ru/Sr_2RuO_4}$ topological junctions by chiral domain wall motion. *Sci. Rep.* **3**, 2480 (2013).

[44] Mao, Z., Maeno, Y. & Fukazawa, H. Crystal growth of $\mathrm{Sr_2RuO_4}$. *Mater. Res. Bull.* **35**, 1813–1824 (2000).

[45] Troeman, A. G. P. *et al.* Temperature dependence measurements of the supercurrent-phase relationship in niobium nanobridges. *Phys. Rev. B* **77**, 024509 (2008).

[46] Kumar, N., Fournier, T., Courtois, H., Winkelmann, C. B. & Gupta, A. K. Reversibility of superconducting nb weak links driven by the proximity effect in a quantum interference device. *Phys. Rev. Lett.* **114**, 157003 (2015).

[47] Michotte, S., Lucot, D. & Mailly, D. Fluxoid quantization in the critical current of a niobium superconducting loop far below the critical temperature. *Phys. Rev. B* **81**, 100503 (2010).

[48] Berdiyorov, G. R. *et al.* Large magnetoresistance oscillations in mesoscopic superconductors due to current-excited moving vortices. *Phys. Rev. Lett.* **109**, 057004 (2012).

[49] Cuevas, J. C. & Bergeret, F. S. Magnetic Interference Patterns and Vortices in Diffusive SNS Junctions. *Phys. Rev. Lett.* **99**, 217002 (2007).

[50] Chiodi, F. *et al.* Geometry-related magnetic interference patterns in long SNS Josephson junctions. *Phys. Rev. B* **86**, 064510 (2012).

[51] Blom, T. J. *et al.* Direct-write printing of Josephson junctions in a scanning electron microscope. *ACS Nano* **15**, 322–329 (2021).

[52] Bouhon, A. & Sigrist, M. Influence of the domain walls on the Josephson effect in Sr_2RuO_4. *New J. Phys.* **12**, 043031 (2010).

[53] Stoutimore, M. J. A. *et al.* Second-harmonic current-phase relation in Josephson junctions with ferromagnetic barriers. *Phys. Rev. Lett.* **121**, 177702 (2018).

[54] Yao, Y. *et al.* Half-integer shapiro steps in strong ferromagnetic Josephson junctions. *Phys. Rev. B* **104**, 104414 (2021).

[55] Willa, R., Hecker, M., Fernandes, R. M. & Schmalian, J. Inhomogeneous time-reversal symmetry breaking in Sr_2RuO_4. *Phys. Rev. B* **104**, 024511 (2021).

[56] Ramires, A. & Sigrist, M. Superconducting order parameter of Sr_2RuO_4: A microscopic perspective. *Phys. Rev. B* **100**, 104501 (2019).

[57] Suh, H. G. *et al.* Stabilizing even-parity chiral superconductivity in Sr_2RuO_4. *Phys. Rev. Research* **2**, 032023 (2020).

[58] Wu, J. *et al.* Electronic nematicity in Sr_2RuO_4. *Proc. Natl. Acad. Sci. U.S.A.* **117**, 10654–10659 (2020).

[59] Mao, Z. Q., Maeno, Y., NishiZaki, S., Akima, T. & Ishiguro, T. In-plane anisotropy of upper critical field in Sr_2RuO_4. *Phys. Rev. Lett.* **84**, 991–994 (2000).

SUMMARY

This thesis examines how size reduction and geometry influence Josephson junctions with normal and ferromagnetic weak links, as well as the properties of highly correlated electron matter through transport experiments. Central to achieving this goal is a top-down sample fabrication technique: by combining mechanical exfoliation of bulk single crystals with focused ion beam (FIB) processing, we can produce microstructured correlated oxide materials. Besides, FIB milling allows us to structure Josephson junctions with arbitrarily-shaped electrodes from macroscopic thin films, having feature sizes well below 1 µm. The thesis is divided into three parts, which I will detail below.

PART ONE: JOSEPHSON PHYSICS IN THIN FILM PLANAR JUNCTIONS

The first part introduces basic concepts of superconductivity and the most fundamental building block of superconducting electronics: the Josephson junction. Chapter two explains that superconductivity is a state of matter characterized by a change of charge carrier statistics from Fermionic to Bosonic nature. This allows them to occupy a single quantum mechanical state, which results in zero electrical resistance and the expulsion of magnetic fields from the center of the bulk, among other properties. The currents that expel the magnetic fields are called shielding currents and are driven by the quantum mechanical phase. Therefore, superconductivity is a manifestation of quantum mechanics at the macroscale. This becomes clear in Josephson junctions, which are two superconducting electrodes separated by a non-superconducting link. The maximum supercurrent such an object can sustain, called critical current (I_c), oscillates as a function of magnetic field (B), resulting from the interference between the shielding currents running in the electrodes.

The shielding currents in the electrodes are determined by the local vector potential for a macroscopic junction. However, when a Josephson junction is situated between two superconducting films that are thinner than the penetration depth of the magnetic field (i.e., London penetration depth), this radically changes. Instead, non-local electrodynamics start to play a role, and the $I_\mathrm{c}(B)$-pattern is determined by the geometry of the electrodes. The third chapter extends the model proposed by John Clem in 2010, which calculated $I_\mathrm{c}(B)$ for a rectangular superconducting strip of length L and width W, separated in the middle by a Josephson junction, to include ellipsoid and rhomboid geometries. We find the periodicity of the $I_\mathrm{c}(B)$-pattern to have universal limits

for $L \gg W$ and $L \ll W$, independent of the geometry of the electrodes. Furthermore, we experimentally verify the L/W dependence of this periodicity by fabricating elliptically shaped planar S−N−S junctions with various aspect ratios. This part concludes by establishing a relation between the $I_c(B)$-pattern and the spatial distribution of critical current in a planar junction between thin films that can be used to analyze possible current channels.

PART TWO: MESOSCOPIC SF-HYBRID JOSEPHSON JUNCTIONS

Ferromagnetism and superconductivity are typically antagonistic properties. In the last twenty years, however, it has been shown that magnetic inhomogeneity at the interface between a superconductor and a ferromagnet can induce long-range triplet (LRT) correlations, penetrating the ferromagnet over long distances. Alternatively, ferromagnetic vortices and Skyrmions were proposed to generate LRT correlations based on their ferromagnetic spin textures, although these lacked experimental realization. In the second part of this thesis, we replace the metallic layer of the S−N−S junctions described in the first part with a ferromagnet, resulting in S−F−S Josephson junctions that feature a deterministic ferromagnetic spin texture due to the shape of the electrodes. We use these junctions to study the interplay of supercurrents and spin texture, which had remained experimentally elusive before.

Specifically, in the fourth chapter, we show that the presence of a ferromagnetic vortex leads to the LRT proximity effect in disk-shaped S−F−S devices. By employing the relation between the $I_c(B)$-pattern and the spatial distribution of critical current developed in the first Part, we find the LRT currents to flow in highly localized channels located at the rim of the device. We explain the emergence of these ‘rim currents’ through the equivalence between the spin texture and an effective spin-orbit coupling, which results in an accumulation of spin at the sample−vacuum boundary that gets transformed into LRT correlations. By modifying the spin texture, we show that we can alter the relative phase between the channels, manifesting itself as the appearance of 0 and π channels.

In Chapter five, we transition to elliptical S−F−S devices to create a stable and non-volatile superconducting memory element that combines the ultra-fast manipulation of spins with dissipationless readout. It functions based on the bistability of magnetic textures of the ferromagnet: the sample can either be uniformly magnetized along its long axis or contains two magnetic vortices at zero applied field. The two states yield considerably different critical currents, which facilitates electrical readout of the bit. We call the low critical current the "1" state and the high I_c state resembles the "0". By quantifying the fields emerging from the ferromagnet using micromagnetic simulations, we show that the change in critical current is caused by the local stray field penetrating the Josephson junction.

PART THREE: STRONGLY CORRELATED RUTHENIUM OXIDE MICROSTRUCTURES

In Part three of this thesis, we use size-reduction in specific geometries to study two strongly correlated ruthenium oxide materials, namely, the isostructural counterparts Ca_2RuO_4 and Sr_2RuO_4. The first is a Mott insulator at room temperature exhibiting an insulator-to-metal transition (IMT) at surprisingly low current densities, making it a candidate material for developing Mott-based electronics. In Chapter six, we study the current densities required for driving Ca_2RuO_4 crystals out of the insulating phase, using size as the principal tuning parameter. We find a four orders of magnitude increase in the current density that induces the current-maintained metastable phase (preceding the fully metallic state) when the crystal size is reduced to the micrometer scale. This effectively shatters the promise of applications using this material. Furthermore, we tackle the hotly debated issue of possible heating effects driving the transition by including a microscopic thermometer on our micrometer-sized samples. We conclude from our thermometry experiments and simulations that heating effects cannot explain the found size dependence. Instead, our findings suggest that an inhomogeneous current distribution over the cross-sectional area is responsible for the size dependence.

One of the large open questions of condensed matter physics is the nature of the electron pairing in the superconductor Sr_2RuO_4. At the moment, the proposals range widely. An attractive approach to differentiate between these proposals is the chirality of the order parameter. A chiral superconductor is characterized by a finite angular momentum of the Cooper pairs, which causes the superconducting order parameter to spontaneously break up into spatially separated domains, each corresponding to a single chirality. In a previous work, we found an experimental signature of the chiral domain walls separating two chiral domains: the order parameter is locally suppressed at the domain wall, which acts as a Josephson junction. In Chapter seven, we further examine the properties of these chiral domain wall junctions. We find that the chiral domain walls are stable in mesoscopic samples of quite different geometries. Furthermore, the I_cR_N product associated with domain wall junctions exhibits a universal temperature dependence. By obtaining the Shapiro response of our samples, we provide definite proof of the Josephson coupling of the domain-wall-associated junctions. Besides, we gain insight into their current-phase relation and find that we can alter the domain structure by applying small in-plane magnetic fields (in the ab-plane of the crystal; $H < H_{c1}$), which is indicated by the appearance of half-integer Shapiro steps in the IV-characteristic. In-plane fields also reveal a bistable critical current, which can be switched by reversing the bias current polarity: by applying either a positive or negative current bias, we switch between a low and high I_c state. We interpret the bistability of I_c as unpinned, and therefore mobile, domain walls in our samples. Finally, we conclude that a chiral d-wave order parameter is best suited for describing superconductivity of Sr_2RuO_4.

SAMENVATTING

Dit proefschrift beschrijft hoe het verkleinen van de elektrodes en hun geometrie invloed heeft op Josephson-juncties met een normaal metaal of ferromagnetische verbinding en hoe het verkleinen van kristallen van sterk gecorreleerde elektronenmaterialen in sepcifieke vormen invloed kan hebben op hun eigenschappen. Dit wordt onderzocht door middel van transportexperimenten. Als rode draad door dit proefschrift loopt de top-down samplefabricagetechniek. Micrometer grote kristallen, verkregen door mechanische exfoliatie, worden met de gefocusseerde ionenstraal (FIB) gefreesd tot microstructuren. Daarnaast, stelt het FIB-frezen ons in staat om Josephson-juncties met arbitrair gevormde elektroden te structureren uit lateraal macroscopische dunne lagen van supergeleiders, met een precisie van ruim onder 1 µm. Dit proefschrift is onderverdeeld in drie delen, die ik hieronder toegelicht.

DEEL ÉÉN: JOSEPHSON FYSICA VAN JUNCTIES TUSSEN DUNNE LAAG SUPERGELEIDERS

In het eerste deel worden de concepten van supergeleiding en de meest fundamentele bouwsteen van de supergeleidende electronica, de Josephson-junctie, besproken. Hoofdstuk 2 zet uiteen dat supergeleiding een toestand is die wordt gekenmerkt door een verandering van de ladingsdragers van fermionische naar bosonische aard, waardoor ze zich in één enkele kwantumtoestand kunnen bevinden. Dit resulteert onder meer in de afwezigheid van elektrische weerstand en de verdrijving van magnetische velden uit de bulk van de supergeleider. De kringstromen die de magnetische velden verdrijven worden afschermingsstromen genoemd en worden aangedreven door de kwantummechanische faseverschillen. Vandaar dat supergeleiding een manifestatie van de kwantummechanica op macroschaal wordt genoemd. Dit wordt duidelijk in Josephson-juncties: twee supergeleidende elektroden gescheiden door een niet-supergeleidende verbinding. De maximale superstroom die een Josephson-junctie kan dragen, de zogenaamde kritische stroom (I_c), oscilleert als een functie van het magnetische veld (B), als gevolg van de interferentie tussen de afschermingsstromen in de elektroden.

Voor een macroscopische junctie bepaalt de lokale vectorpotentiaal de afschermstromen in de elektroden. Dit verandert echter wanneer een Josephson-junctie zich tussen twee supergeleidende films bevindt die dunner zijn dan de penetratiediepte van het magnetische veld. In dit geval bepaalt de niet-lokale elektrodynamica de afschermstromen, en wordt het $I_\mathrm{c}(B)$-patroon volledig bepaald door de geometrie van de elektroden. Het derde hoofdstuk is een uitbreiding op het door John Clem in 2010 voorgestelde model, dat $I_c(B)$ geeft voor een rechthoekige supergeleidende strook met lengte L en breedte W, gedeeld in twee door een Josephson-junctie in het midden van de strook, naar ellipsoïde en ruitvormige geometrieën. We vinden dat de periodiciteit van het $I_c(B)$-patroon twee universele limieten heeft voor $L \gg W$ en $L \ll W$, onafhankelijk van de geometrie van de elektroden. Verder leveren we een experimentele verificatie van de L/W-afhankelijkheid van deze periodiciteit door elliptisch gevormde vlakke S–N–S-juncties te fabriceren met verschillende L/W-verhoudingen. We sluiten dit deel af met een relatie tussen het $I_c(B)$-patroon en de ruimtelijke verdeling van kritische stroom in een vlakke junctie tussen twee dunne films die kan worden gebruikt om mogelijke stroomkanalen te analyseren.

DEEL TWEE: MESOSCOPISCHE SF-HYBRIDE JOSEPHSON JUNCTIES

Ferromagnetisme en supergeleiding zijn doorgaans twee elkaar tegenwerkende fenomenen. In de afgelopen twintig jaar is echter aangetoond dat magnetische inhomogeniteit in het grensvlak tussen een supergeleider en een ferromagneet een superstroom kan genereren die de ferromagneet over lange afstanden kan binnendringen. Naast magnetische inhomogeniteit is er een groep alternatieve theoretische voorstellen om deze zogeheten *long-range triplet* (LRT-)correlaties te induceren op basis van ferromagnetische spintexturen zoals vortices. Deze zijn echter nog niet experimenteel gerealiseerd. In het tweede deel van dit proefschrift vervangen we de metallische laag van de S–N–S juncties beschreven in het eerste deel door een ferromagneet, wat resulteert in S–F–S Josephson-juncties met een deterministische ferromagnetische spintextuur geïnduceerd door de geometrie van de elektroden. We gebruiken deze juncties om de, voorheen experimenteel niet toegankelijke, interactie van superstromen en spintexturen te bestuderen.

In het bijzonder demonstreert het vierde hoofdstuk dat de aanwezigheid van een ferromagnetische vortex leidt tot LRT-correlaties in schijfvormige S–F–S-juncties. Door gebruik te maken van de relatie tussen het $I_c(B)$-patroon en de ruimtelijke verdeling van kritische stroom beschreven in het eerste deel, vinden we dat de LRT-stromen in sterk gelokaliseerde kanalen aan de rand van het sample stromen. We verklaren het ontstaan van deze '*rim currents*' door de equivalentie tussen de vortex spintextuur en een effectieve spin-baankoppeling die resulteert in een accumulatie van spin aan het sample–vacuüm grensvlak, welke vervolgens wordt omgezet in LRT-correlaties. Door de spintextuur aan te passen, laten we zien dat we de relatieve faseverschuiving tussen de kanalen kunnen veranderen, wat zich manifesteert als 0 en π kanalen in de junctie.

In hoofdstuk vijf beschrijven we elliptische S–F–S-juncties die een stabiel en niet-vluchtig supergeleidend geheugenelement vormen dat de ultrasnelle manipulatie van spintexturen combineert met uitlezing zonder warmtedissipatie. Het werkingsprincipe achter het geheugenelement is de bistabiliteit van magnetische texturen van de ferromagneet: het sample kan ofwel uniform gemagnetiseerd zijn langs zijn lange as of bevat twee ferromagnetische vortices, in de afwezigheid van een extern aangelegd magnetisch veld. De twee toestanden leveren aanzienlijk verschillende kritische stromen (I_c) op, wat de elektrische uitlezing van de bit vergemakkelijkt. We noemen de lage I_c toestant de "1"toestand en de hoge I_c toestand de "0"toestand. Door de velden die uit de ferromagneet komen te kwantificeren met behulp van micromagnetische simulaties, laten we zien dat de verandering in kritische stroom wordt veroorzaakt door het lokale strooiveld dat de Josephson-junctie binnendringt.

DEEL DRIE: MICROSTRUCTUREN VAN STERK GECORRELEERDE RUTHEEN OXIDEN

In deel drie van dit proefschrift gebruiken we de reductie van sample dimensies in specifieke geometrieën om twee sterk gecorreleerde rutheenoxides te bestuderen, namelijk de isostructurele tegenhangers Ca_2RuO_4 en Sr_2RuO_4. De eerste is een Mott-isolator bij kamertemperatuur die een isolator-naar-metaaltransitie (IMT) vertoont bij verrassend lage stroomdichtheden, waardoor het een kandidaat-materiaal is voor de ontwikkeling van nieuwe Mott-IMT elektronica. In hoofdstuk zes bestuderen we de stroomdichtheid waarmee Ca_2RuO_4 kristallen uit de isolerende fase gedreven kunnen worden, waarbij we de grootte van de kristallen als parameter gebruiken. We vinden een toename van vier ordes van grootte in de stroomdichtheid die de metastabiele fase induceert (welke vooraf gaat aan de volledig metallische toestand) wanneer de kristalgrootte wordt verkleind tot de micrometerschaal. Daarmee laten we zien dat Ca_2RuO_4 niet geschikt is voor toepassingen binnen de elektronica. Verder bespreken we de opwarmeffecten die mogelijk verantwoordelijk zijn voor de IMT, een heet hangijzer in onderzoek aan de IMT in Ca_2RuO_4. We bereiken dat door een thermometer van micrometerformaat in onze samples op te nemen. We concluderen uit onze thermometrie-experimenten en simulaties dat verwarmingseffecten de gevonden grootte-afhankelijkheid niet kunnen verklaren. In plaats daarvan suggereren onze bevindingen dat een inhomogene stroomverdeling over het dwarsdoorsnede-oppervlak verantwoordelijk is voor de grootte-afhankelijkheid.

Een van de grote open vragen van de vaste stof fysica is de aard van de elektronenparen in de onconventionele supergeleider Sr_2RuO_4. Op dit moment lopen de voorstellen dan ook sterk uiteen. Een aantrekkelijke benadering om onderscheid te maken tussen deze voorstellen is de chiraliteit van de ordeparameter. Een chirale supergeleider wordt gekenmerkt door een eindig baanimpulsmoment van de Cooper-paren, waardoor de supergeleidende ordeparameter zich spontaan opbreekt in ruimtelijk gescheiden domeinen, elk overeenkomend met een enkele chiraliteit (rechts- of linkshandig). In een eerdere publicatie, vonden we bewijs voor het bestaan van de chirale domeinwanden die twee chirale domeinen scheiden. De ordeparameter wordt bij de domeinwand onderdrukt en fungeert daarom als een Josephson-junctie. Hoofdstuk zeven gaat dieper in op de eigenschappen van deze chirale domeinwand-juncties. We vinden dat de chirale domeinwanden stabiel zijn in mesoscopische samples van verschillende geometrieën en dat het $I_\mathrm{c}R_\mathrm{N}$ product geassocieerd met domeinwand-juncties een universele temperatuurafhankelijkheid vertoont. Door de Shapiro-respons van onze samples te verkrijgen, leveren we definitief bewijs van het Josephson-effect van de chirale domeinwanden. Bovendien krijgen we inzicht in hun stroom-faserelatie en ontdekken we dat we de domeinstructuur kunnen beïnvloeden door kleine magnetische velden in het vlak (het ab-vlak van het kristal; $H < H_\mathrm{c1}$) aan te leggen, hetgeen we opmaken uit het verschijnen van halve Shapiro-stappen in de IV-karakteristiek. Bovendien onthullen magneet velden in het ab-vlak een dubbelstabiele kritische stroom, die kan worden geschakeld door de polariteit van de aangelegde stroom om te keren: door ofwel een positieve of negatieve stroom aan te leggen, schakelen we tussen een lage en een hoge I_c toestand. De oorzaak van de bistabiliteit in I_c ligt in mobiele domeinwanden in onze samples. Ten slotte concluderen we dat een chirale d-wave orderparameter het meest geschikt is voor het beschrijven van supergeleiding van $\mathrm{Sr_2RuO_4}$.

CURRICULUM VITAE

I was born in February 1993 in Rotterdam. In the same city, I completed my pre-university education at the Rotterdams Montessori Lyceum in 2012. Afterwards, I studied physics at Leiden University, obtaining a BSc and MSc degree cum laude. Throughout my BSc education, I have also successfully finished an honors course in philosophy. During my masters, I performed two research projects, which gained me experience in transport experiments in microstructures. During the first, carried out under the supervision of prof. Jan Aarts, I developed a method of exfoliating and contacting Sr_2RuO_4 flakes, a skill that has enabled Chapter six and seven of this thesis. The second project I carried out at the Max Planck Institute for Chemical Physics of Solids in Dresden, Germany, under the supervision of Dr. Philip Moll. During this project, I studied the resistivity anisotropy in the normal state of an iron pnictide superconductor. Since these crystals can only be grown in micrometer-sized crystallites, we employed focused ion beam milling to fabricate microstructures with different geometries to extract the components of the resistivity tensor. Learning how to apply focused ion beam milling properly has greatly influenced the research presented in this thesis. After my time at the Max Planck institute, I returned to Leiden University to start my PhD research under supervision of prof. Jan Aarts in 2018.

LIST OF PUBLICATIONS

- A. Bellunato, S. D. Voltan, C. Sabater, E. W. de Vos, **R. Fermin**, K.N. Kanneworff, F. Galli, J. M. van Ruitenbeek and G. Schneider. Dynamic tunneling junctions at the atomic intersection of two twisted graphene edges, *Nano Letters* **18**, 2505-2510 (2018).
- Y. Yasui, K. Lahabi, V. F. Becerra, **R. Fermin**, M. S. Anwar, S. Yonezawa, T. Terashima, M. V. Milošević, J. Aarts and Y. Maeno. Spontaneous emergence of Josephson junctions in homogeneous rings of single-crystal Sr_2RuO_4, *npj Quantum Materials* **5**, 21 (2020).
- T. J. Blom, T. W. Mechielsen, **R. Fermin**, M. B. S. Hesselberth, J. Aarts and K. Lahabi. Direct-write printing of Josephson junctions in a scanning electron microscope, *ACS Nano* **15**, 322-329 (2020).
- **R. Fermin***, G. Avallone*, K. Lahabi, V. Granata, R. Fittipaldi, C. Cirillo, C. Attanasio, A. Vecchione and J. Aarts. Universal size-dependent nonlinear charge transport in single crystals of the Mott insulator Ca_2RuO_4, *npj Quantum Materials* **6**, 91 (2021).
- **R. Fermin**, D. van Dinter, M. Hubert, B. Woltjes, M. Silaev, J. Aarts and K. Lahabi. Superconducting triplet rim currents in a spin-textured ferromagnetic disk, *Nano Letters* **22**, 2209-2216 (2022).
- **R. Fermin**, N. Scheinowitz, J. Aarts and K. Lahabi. Mesoscopic superconducting memory based on bistable magnetic textures, *Physical Review Research* **4**, 033136 (2022).
- **R. Fermin**, B. de Wit and J. Aarts. Beyond the effective length: How to analyze magnetic interference patterns of thin film planar Josephson junctions with finite lateral dimensions, under review at *Physical Review B*, arXiv:2210.05388.
- **R. Fermin** et al. Controlling chiral domain walls in mesoscopic Sr_2RuO_4 using geometry and in-plane magnetic fields, *To be submitted.*

---

*These authors contributed equally.

ACKNOWLEDGEMENTS

First and foremost, I want to express my gratitude to Jan Aarts for enabling me to do research at LION and, in some sense, enabling research at LION in general. As scientific director, you have quite a full schedule, yet you always manage to find the time to support me. Your vast overview of physics combined with deep-reaching knowledge of superconductors and material physics is genuinely inspiring.

Usually, PhD students are supervised by a promotor and a co-promotor. Although I did not have a co-promotor, I worked closely with Kaveh Lahabi on most of the projects presented in this thesis. I could always count on his knowledge and support, making him closest akin to a co-promoter.

As evidenced by the long author lists at the beginning of each chapter of this thesis, experimental physics is always a team effort. I want to express my gratitude for the collaborations with scientists from other universities that helped this thesis come about. First, Mikhail Silaev, for his theoretical work on the generation of long-range triplets in the Co-disk junctions. Next, Guerino Avallone, Victoria Granata, Rosalba Fittipaldi, Carla Cirillo, Carmine Attanasio, and Antonio Vecchione for working together on the size-dependent nonlinear charge transport in the Ca_2RuO_4 crystals. Especially, *'Wajio'* Guerino, for doing the experiments on Ca_2RuO_4 with me and the discussions on the sample quality, during his stay here in Leiden. Finally, I thank Alexander Brinkman for allowing me to measure the Sr_2RuO_4 samples at Twente University and Joost Ridderbos for supporting me with those measurements. The measurements were not only helpful for completing this thesis, but I also learned a lot about low-noise measurement set-ups during those two weeks.

Apart from collaborators, I want to thank all students I have worked with during these years. Chronologically I want to thank: Allard Nieuwesteeg for contacting BSCO flakes; Bart Woltjes for his measurements on the Co-disk junctions and Sr_2RuO_4 rings; Dyon van Dinter for his work on the cobalt disks, Frans van Die for his work on BSCO; Guido Stam for measuring a ton of Sr_2RuO_4 samples remotely during the lock-down; Naor Scheinowitz for his simulations and measurements on the ellipse-shaped memories and Bob de Wit for helping to extend the Clem model to elliptical geometries.

I am also grateful for the technical support from the fine mechanical department (FMD) and electronics department (ELD). Specifically, Peter van Veldhuizen from the ELD, who always was available for quick repairs to inserts, and Ruud van Egmond and

Christiaan Pen from the FMD, for their support on the Vectormagnet. I also owe a debt of gratitude to the research technicians of LION: Thomas Mechielsen, Marcel Hesselberth, and Douwe Scholma; you always kept the equipment running, gave countless intros to students, and always were standing by for quick support. Federica Galli, I want to thank you for your continued support on solving the issues that plagued the Vectormagnet over the years. I also would like to thank Daniëlle Duijn for the adequate help on administrative matter and Ellie van Rijsewijk for making the graduation procedure as smooth as possible.

I am thankful for all individuals in LION that make the atmosphere such a great working environment. Specifically, I want to thank the (former) members of the MSM group: Junxiang Yao, Nikita Lebedev, Aymen Ben Hamida, Kumar Prateek, Xing Chen, Iacopo Bertelli, and Chunhai Yin, in addition to those mentioned above, for the great times. A special thanks to Jimi de Haan and Norman Blümel: it is safe to say that your festive spirits are responsible for much of the social cohesion within LION.

Although doing a PhD is a tremendous amount of fun, it is only so with a proper work-life balance. Therefore I would like to thank my friends from outside the university that helped me recharge during these *four more years*: Anne, Bert, Allard, Sebas, Peter, Wico, Tristan, Richard, Sophie, Felix, Jean, Jet, Evelien, Jasper, Marijn, Thomas, Siyun, Olivier, and Sanjana thank you for the great memories these years. I would also like to thank Z. Schaap for his continued support.

I want to express my greatest gratitude to my parents, Hubert and Monique, who always supported me. By explaining what I was researching here in Leiden, I would always rediscover my love for experimental physics and realize how lucky I am to do research for a living. Finally, I cannot forget my dear Isabel. You are always there for me, and support me no matter the stress level. I could not have finished the PhD without your aid, and I look forward to our next adventure, 'post-Leiden'!